Iron-oxide catalyzed silicon photoanode for water splitting

by

Kimin Jun

B.S. Mechanical and Aerospace Engineering
Seoul National University, Korea (2002)

M.S. Mechanical and Aerospace Engineering
Seoul National University, Korea (2006)

Submitted to the Department of Mechanical Engineering
in partial fulfillment of the requirements for the degree of

Doctor of Philosophy in Mechanical Engineering
at the

MASSACHUSETTS INSTITUTE OF TECHNOLOGY

September 2011

© 2011 Massachusetts Institute of Technology. All rights reserved.

Signature of Author……………………………………………………………………………….
Department of Mechanical Engineering
July 26, 2011

Certified by………………………………………………………………………………………….
Joseph M. Jacobson
Associate Professor of Mechanical Engineering and Media Arts and Sciences
Thesis Supervisor

Accepted by………………………………………………………………………………………….
David E. Hardt
Chairman, Department Committee on Graduate Students

Iron-oxide catalyzed silicon photoanode for water splitting

by

Kimin Jun

Submitted to the Department of Mechanical Engineering on August 10, 2011
in partial fulfillment of the requirements for the degree of
Doctor of Philosophy in Mechanical Engineering

Abstract

This thesis presents an integrated study of high efficiency photoanodes for water splitting using silicon and iron-oxide. The fundamental limitations of silicon to water splitting applications were overcome by an ultrathin iron-oxide film stack and a pH-adjusted electrochemical environment. It was experimentally demonstrated that this functional photoanode has very strong photoactivity exceeding the performance of previously reported systems. A complete theoretical explanation is provided with experimental substantiations.

Two major obstacles of the application of silicon to water splitting are its high valence band edge and the lack of catalytic functionality. The solution for band edge mismatch is to facilitate the unique pH response of silicon with respect to electrolyte pH. As opposed to the low pH, a high pH electrolyte allows the silicon valence band edge to be located below the oxygen evolution potential, providing physical platform for the water oxidation reaction. In this platform, the introduction of a thin iron-oxide layer was proved to effectively catalyze the anode reaction which is otherwise impossible. The very thin film enables the separation of the two key functions of the photoelectrode: photocarrier generation and catalysis. Since the iron-oxide film has a very low absorption of incident light, phorocarriers are generated in the silicon layer, while the surface still maintains catalytic functionality. By this functional separation, it was possible to overcome the loss incurred by poor electronic and photovoltaic properties of iron-oxide. The thin semiconducting film also allows a space charge region to span beyond the catalyst layer to silicon, inducing a large built-in potential to lower the required overpotential. Additional improvement was made by adopting silicon microfabrication techniques to maximize light harvesting and minimize potential losses in silicon layer. By vertical wires and ohmic contact formation, the onset potentials were decreased and the current-potential slopes were steepened, resulting in current density as high as 17 mA/cm^2 at zero overpotential.

These results were obtained with two of the most abundant materials, and as such shows the prospect of an efficient solar-driven water splitting pathway. In addition, the comprehensive theoretical explanations will contribute to searching for further system improvements.

Thesis Supervisor: Joseph M. Jacobson
Title: Associate Professor of Mechanical Engineering and Media Arts and Sciences

Table of contents

Figures and Tables

Acknowledgements

This thesis may entitle me to a Ph.D., but I am certain that what awards the degree to me is not the thesis itself, but all the people around me whose minds are dissolved in this thesis. I am deeply grateful to everyone.

Joseph Jacobson, my advisor, is a respectable thinker. His envisions and insights broadened my scope and grew mine. Also, his patient and continuous supports allowed me to explore various topics, and finally find one I like.

I appreciate kind supports of my committee members and participating faculties. Prof. Sang-Gook Kim and prof. Carl Thompson guided and encouraged my researches at every meeting. They pointed what is missing and what must be clarified. Also, the advices and discussions with prof. Neil Gershenfeld, prof, Jeffrey Grossman and Dr. Peter Carr enriched this thesis. Prof. Tonio Buonassisi allowed to conduct these experiments in his facilities and gave me valuable feedbacks on the manuscript.

My research group, Molecular Machines and the Center for Bits and Atoms was a wonderful place to work at. Especially, Brian Chow, David Kong and Manu Prakash gave me a lot of helps in physical setups and chemical protocols from the time I joined. Dr. Sangjun Moon was not only a talented coworker but a great mentor. I appreciate the administrative supports from Joseph Murphy, Patty Tolan, Nicole Degnan, Sherry Lassiter, Kelly Maenpaa, John DiFrancesco, Tom Lutz, Kevin Davis and Leslie Regan in Media Lab and Mechanical Engineering. I also got many technical helps from campus wide, including Dr. Seungwoo Lee, Rupak Chakraborty and Heechul Park.

Special gratitude must go to Jaebum Joo, Yun Seog Lee and Kurt Broderick. Jaebum has always been with me in the lab. From researches to life, the chatting with him was productive and enjoyable. Also, I owe Yun Seog his devoted helps of solar experiments and materials analysis. All of my fabrication processes must have not been possible if Kurt was not here in MIT.

Korean society, particularly KGSAME was a great supporting group. The lively colleagues refreshed and, at the same time, stimulated me. I also shared much time with Media Lab Korean colleagues in personal meetings and workshops, filling myself with ample new ideas and enthusiasm with them.

Samsung Scholarship foundation thankfully supported my graduate life with generous scholarship. The CBA and prof. Gershenfeld financially supported every part of my research.

Finally, the last slot. This is reserved for my family. Whenever I mentally struggled with the hard time, you were always beside me. Father, mother and my sister, Moonkyoung, I know you were busy encouraging me so often for last five years. Now I want to do the role for you. And, my wife, Minkyeong, this thesis is yours. I can't find any better words, just…… thank you and I love you.

Chapter 1   Chemical fuel and solar water splitting

1.1 Renewable chemical fuel

'Energy crisis' became a word we hear on daily basis. The vulnerability of energy resource prices(mostly fossil fuels) has been increased in last decades. Although there are debates about the origin, reserves or speculations, it is obvious that the energies based on physical commodities will be more expensive or even depleted in the future. To overcome this apparent and predictable crisis, there are intense researches on alternative energies. Major philosophies behind these approaches are sustainability and ubiquitousness to supply energy eternally with domestic resources. Therefore, naturally harvested energies are the preferred forms such as solar, wind and geothermal energies. These primary energy resources are hard to be used as they are, but must be converted to useful and convenient secondary forms. Also these natural energy sources exist as low density forms in residential area, as a result, sometimes requiring extreme environments for maximized efficiency. Solar energy facilities in desert or wind farms off the seashore are good examples. Due to these reasons, electricity is typically generated on site and readily distributed through grid system. Then, why should we be bothered to deliver chemical energies?

1.1.1 Necessity of renewable chemical energy

Figure 1.1 shows primary energy use expectation by end-use sector in United States.[1] Most of the industrial, commercial and residential consumption is occupied by fixed installations, therefore online operation, which is based on grid energy distribution, is common energy supply scheme. However, large portion of energy consumption depends on stored energies, or off-grid energies. A good example is transportation which accounts for more than 25% of total energy consumption as shown in figure 1.1. Also, emergency facilities, physically isolated installations and mobile appliances require energy storage media for offline operations. This means proper measures should be devised to compensate the demands for offline operations in addition to online energies which are represented by electricity grid system.
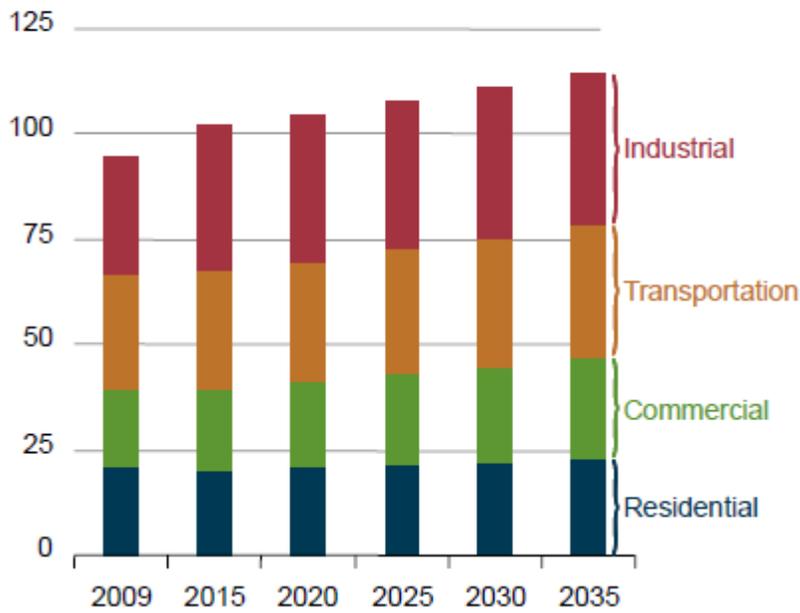
Figure 1.1 Primary energy use by end-use sector, 2009-2035 (quadrillion Btu)

Following figure 1.2 [2] shows a list of storage media and their specific energies.
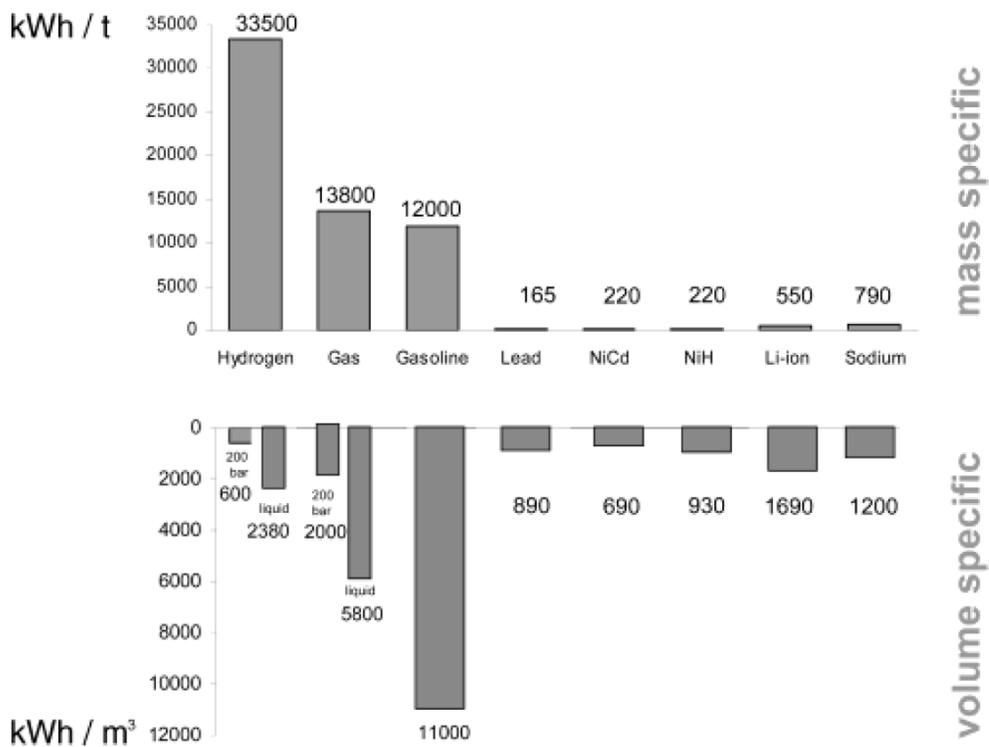
Figure 1.2 Theoretical specific energies of selected media

14

Considering electricity grid system as our core infrastructure, battery deserves to be a firsthand choice. Although it is obvious from the figure 1.2 that batteries have much lower specific energy compared to chemical media, their simple construction provides strong advantages including scaled down builds and easy embedment into devices. Also, since no physical exchanges of materials are necessary, batteries are appropriate for portable appliances like electronics.

There are ongoing trials to extend the usage of batteries into more energy intensive applications such as transportation. In reality, many vehicles using battery or hybrid powertrain are being developed. However, as shown in figure 1.2, although researchers have developed high specific energy batteries, still their energy contents are much lower than conventional chemical fuels, therefore the usage is limited. For example, modern passenger cars typically generates well above 100 horse power output, which is about 75 kW. Considering laptops with well below 100 W specification, this is about three orders larger number. This manifests that current battery technologies cannot completely satisfy energy demands of exemplified ground transportation. This is even more problematic in air transportation. In spite of the huge heat loss, turbo propulsion is the dominant choice for aircraft engine due to its high specific thrust. In this aspect, the idea of replacing chemical fuels with batteries is still premature in energy intensive fields. Refueling is another issue in practical operation. While chemical fuel can be filled up within minutes, battery recharging takes hours of continuous plugging. Long term degradation of battery increases the overall operation costs, too.

Since grid systems and batteries cannot completely compensate the needs for offline energy applications, the development of renewable chemical fuel is an indispensible task.

1.1.2 Types and production methods of renewable chemical fuels

Potentially available chemical fuels include hydrogen and synthetic hydrocarbon. Hydrogen is one of the most primitive chemical fuels. It is versatile, for example, as a burning gas, it can be directly fed into combustion chamber. Or, it is a fuel for fuel cell, generating electricity. At any application, the final exhaustive product is water, so there is no worry about pollution. On the other side, hydrogen always comes with the problem of storage. Since liquefied hydrogen requires extremely low temperature, practical storage is compressed gas or alloyed phase through chemical bonding. Former method accompanies safety issue, and for latter solution, the technologies are still in early stage. Therefore, the use of hydrogen and the discussion of storage should be reckoned simultaneously.

Another candidate is hydrocarbon liquid fuel, which includes synthetic hydrocarbon and alcohols. They are stable in normal conditions, and the volume specific energy is higher than any other chemical energies, minimizing the concern on storage. However, as we have experienced, the carbon contents emit carbon dioxide, a major green house gas. Therefore, renewable application requires carbon dioxide capturing and recycling technologies, too.

In fact, synthetic processes of hydrogen and hydrocarbon have many aspects in common. Notably, water splitting is in the core of the processes to generate hydrogen(or proton). Hydrocarbon is synthesized by follow-up steps which combine this hydrogen with carbon. Therefore, effective water splitting should be the essential first task to achieve renewable fuel synthesis. The water splitting can be conducted by several ways, but representatively, electrolysis, thermolysis and photosynthesis.

Electrolysis uses electricity to decompose water molecule into oxygen and hydrogen. When high enough electric potential is applied, anode oxidize water molecule into oxygen and proton, while cathode reduces the proton into hydrogen.(Details will follow in section 1.2) In thermolysis(or thermochemical) reaction,[3] the liquid water is heated, typically above 2000 ℃, then intrinsic bonding of water is broken resulting in various phases of hydrogen and oxygen atomic compounds including hydrogen molecule. In photosynthesis, water is decomposed by electron transport through photosystem I and II with the help of catalyst. Most of the bio organisms subsequently produces oxygen and proton compound(NADPH), however those organisms containing specially designed hydrogenase,[4] or under certain conditions,[5] can dominantly produce hydrogen.

Above classification is based on the processes. However, the advantage of certain process is rather dependant on the type of primary energy source. When it comes to solar energy which is overwhelmingly abundant and renewable than any other forms of energy source, the comparison between electrolysis by photovoltaic devices and photosynthesis by bio organisms is particularly popular but controversial. The complexity generally originates from how to calculate all the investment and opportunity costs. However, in the context of fundamental energy storage efficiency, photovoltaic system is said to have a clear advantage over photosynthesis.[6] Also, although solar thermochemical production might be competitive with solar-electrolysis under certain reactions,[7] the uncertainties in the intermediate processes as well as materials challenges against the extreme temperature generally gives advantage to electrolysis over thermolysis. In these considerations within solar based technologies, photovoltaic electrolysis is estimated to be economically more promising than other methods.

1.1.3 Hydrogen for hydrocarbon synthesis

In section 1.1.2, the problem of hydrogen storage was briefly mentioned. Although hydrogen has excellent mass specific energy, its low density gives hydrogen the title of the worst volume specific energy media. Also, the explosive nature raises a safety concern for storage. Visions like hydrogen grid[8, 9] cannot solve the fundamental problems, rather hamper the meaning as a portable fuel. In this respect, synthetic liquid hydrocarbon made of hydrogen is an attractive storage option not only because it provides safely condensed phase, but also allows to inherit the vast infrastructures of current hydrocarbon economy. This overall research is dedicated to solar water splitting for hydrogen production, however a brief and limited introduction to synthetic hydrocarbon fuel will be presented in this section, without losing the contextual consistency.

Liquid fuels can be produced by bio organisms.[10] In this case, without dedicated hydrogen production process, the protons are directly used to grow biomass during photosynthesis. This biofuel is largely classified into bioethanol and biodiesel. Bioethanol is mainly produced by fermentation of sugar-rich plants, while biodiesel is produced by transesterification process of oil extracted from oil-rich crops or microalgae. These bio processes, seemingly renewable and environmentally friendly, raise continuous debates about the effectiveness. In energy storage standpoint as mentioned in previous section, bio processes are not more efficient than other competitors like photovoltaic processes. In addition to the opportunity costs of land, fertilizer and transportation which have already been considered quantitatively, there are a lot more issues whose metrics have not been established yet, such as the side effect of plantation. Although microalgae may be a better option on these issues, scaled up application of biofuels needs further investigation at this moment.

Assuming there is ample supply of hydrogen, the chemical process for synthetic fuels can be implemented. Until now, the most successful and scalable method is Fischer-Tropsch(FT) method.[11-13] Figure 1.3[12, 13] describes the schematic diagram of the FT process.

Processes and Technology

$$(2n+1)H_2 + nCO \rightarrow C_nH_{(2n+2)} + nH_2O$$
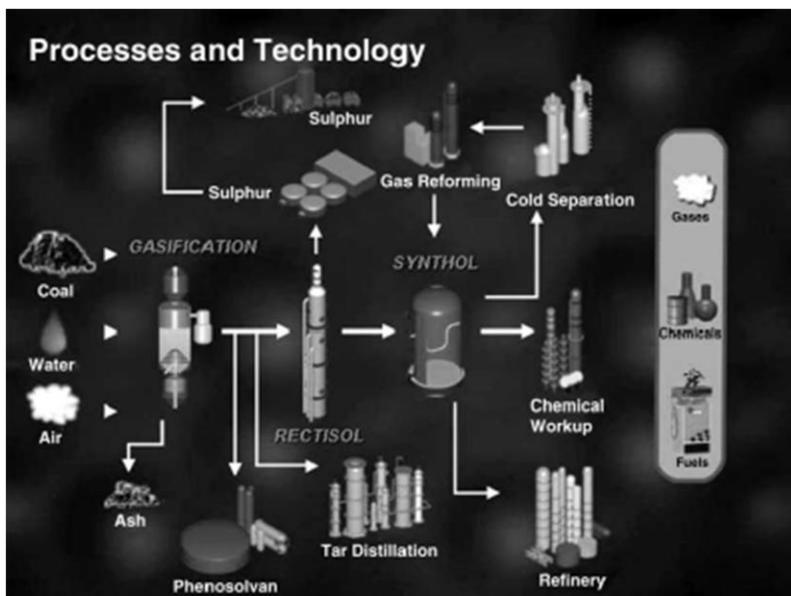
Figure 1.3 Fischer-Tropsch process

The chemical ingredient is syngas, that is, carbon monoxide and hydrogen. By controlling the reaction environment, long hydrocarbon chain(typically $C_1 - C_{15}$) can be synthesized. This process is being commercially operated in countries like South Africa effectively producing about 800,000 barrels of liquid hydrocarbon per day. One of the important advantages of FT process is the freedom of carbon sources since it requires carbon monoxide which can be easily derived from various sources. Although coal and natural gas are currently used as the primary carbon sources, many prospective carbon dioxide recycling processes can be implemented to supply carbon monoxide.[14] In the mean time, there should be viable and recyclable path for hydrogen supply, which does not exist yet. Currently, hydrogen is obtained by reforming carbon containing resources. However, the large amount of carbon dioxide generated as the byproduct of reforming process is simply wasting valuable carbon sources as well as requiring additional CO_2 recycling load. By supplying renewable hydrogen, it is estimated that the current conversion efficiency of about 62 %[11] can be enhanced, which makes FT process more economic. This implies that renewable hydrogen generation can contribute to carbon neutral economy while still allowing the consumption of hydrocarbon fuels.

1.2 Overview of solar water splitting

1.2.1 Electrochemical water splitting mechanism

In this section, a few general electrochemical concepts, especially regarding semiconductor electrochemistry,[15-17] will be presented, which are the basis for semiconductor solar water splitting. Then, the mechanism for this specific reactions, water reduction and oxidation will be explained in detail.

1.2.1.1 Electrochemistry at metallic and semiconducting electrodes
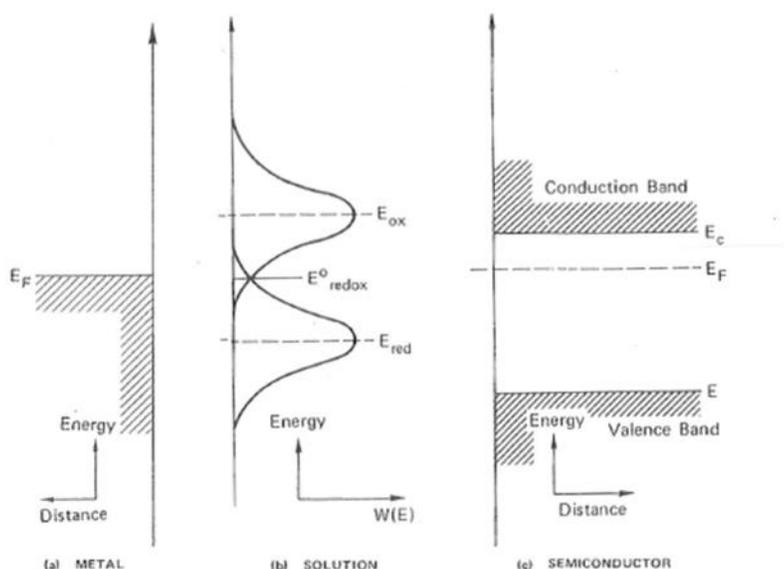
Figure 1.4 Energy models of metal, electrolyte and semiconductor

Figure 1.4[15] describes basic energy models of solid electrodes and liquid electrolyte. In solid electrode, energy band is modeled from atomic energy level.[15, 18] Isolated atoms have discrete levels of energy. However, in solid phase, numerous atoms locate side by side, making overlapped energy levels. Due to the Pauli's exclusion principle, the overlapped energy levels can no longer possess their original energies, but slightly shifted. This eventually forms pseudo-continuous energy bundle, called energy band. The band normally occupied by valence electrons is called valence band, while generally unoccupied but excited states' energy bundle is called conduction band. Depending on materials' atomic orbital, there could be forbidden 'gap' between these valence band and conduction band. If the gap is negative, that is, if the two bands overlap, it is metallic, and always conductive. In contrast, if the gap is largely positive,

typically more than 3 eV, it is insulating. In most of the conditions, insulator doesn't flow current. The set of materials in between metal and insulator is called semiconductor. It becomes conductive conditionally. If valence electrons are excited, they make mobile carriers: holes in valence band and electrons in conduction band. These carriers contribute to the current flow providing the semiconductor conductivity. This carrier distribution can be modified by doping exotic atoms which donate or accept electrons. The energy level in which there are 50 % chance of the electron occupation is called Fermi level.

The fundamental difference between solid electrode and liquid electrolyte lies in the mobile carrier. In case of solid material, atoms are confined in their relative positions with adjacent atoms. Therefore, only electrons can travel through this atomic network. However, in liquid electrolyte, electrons cannot travel. Instead, only ions can move and carry charges. Therefore, when the ionic species are brought into contact with solid interfaces like metal, they experience reduction or oxidation since the types of mobile carriers must be converted. The tendency of reduction and oxidation(redox) varies depending on ionic species. Some ions show very strong oxidizing behavior, while others have strong reducing behavior. This energetic tendency is quantitatively unique on each redox couple, so can be expressed as a corresponding electric potential. This is called standard electrode potential or redox potential(E^0_{redox}). In more precise view, the energy levels of a redox couple are located slightly apart from each other, and are also probabilistic functions. Therefore, the energy level of equilibrated probability is termed as redox potential. This sounds conceptually very similar to Fermi level of solid electronics, and surprisingly, it is.
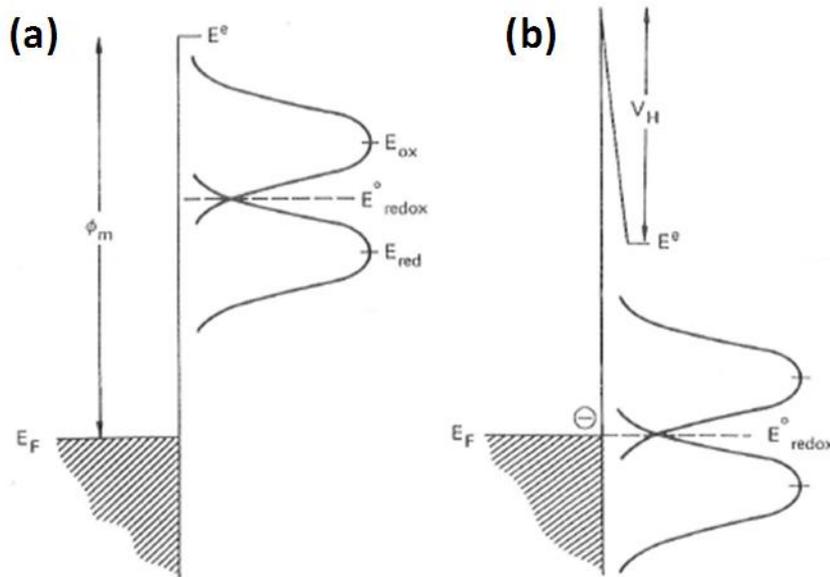
Figure 1.5 Liquid electrolyte redox schematic diagram at metallic electrode, (a) before contact and (b) after equilibrium.

Figure 1.5[15] describes electrochemical reaction in a metal electrode. Assuming Fermi level of metal electrode is lower than redox potential, then the redox couple tends to "lose" electrons to electrode. Since the metallic surface has high carrier concentration, the carrier distribution of metal isn't altered. However, in liquid side, the chemical reaction increases the number concentration of certain polar ions. This inhomogeniety creates electric double layer, called Helmholtz double layer. This Helmholtz layer makes liquid version of "space charge region" in which electric field exists. As a result, the reaction continues until Fermi level of metal and that of liquid(that is, redox potential) are equilibrated.

Semiconductor electrode has limited carrier concentration, typically lower than electrolyte ionic concentration.(From now on, unless specified, 'semiconductor' denotes nondegenerate semiconductor.) Therefore, when semiconductor comes into contact with liquid electrolyte, initially the carriers are exchanged. The relative position of redox potential and energy bands determines the direction. However, the semiconductor carriers are soon depleted. Similar to semiconductor to metal contact, in the semiconductor is formed band bending over wide space charge region, which is much wider than Helmholtz layer thickness. This reaction continues until equilibrium at which carrier concentrations of electrode and liquid are equal, as described in figure 1.6.[19] Note the different mobile carriers of valence band(hole) and conduction band(electron). Anode reaction is driven by semiconductor valence band, while cathode reaction is driven by conduction band. Figure 1.6 shows hole transfer overwhelms electron transfer in n-type semiconductor. If additional potential is given to the semiconductor, the space charge region can vanish. This potential is called flat band potential as is the case in solid junction, and the flat band potential gives the information about semiconductor band edge positions.
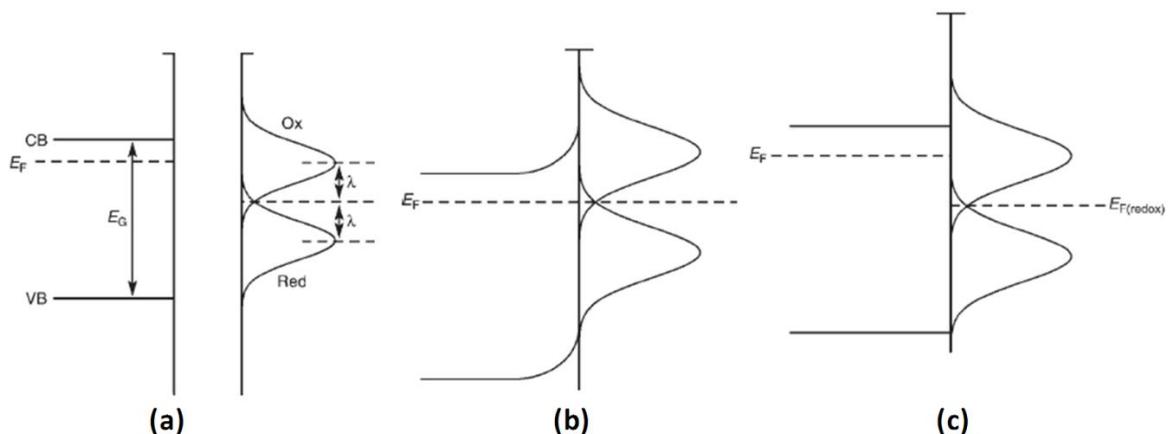
Figure 1.6 Semiconductor electrode and electrolyte junction diagram, (a) before contact, (b) equilibrium and (c) flat band condition.

As vacuum is arbitrarily used as a standard energy level in solid state physics, reference electrodes can be chosen to set a standard scale for convenience. Typically, redox potential of stable redox couple is chosen, such as normal hydrogen electrode(NHE) in which unit activity proton and hydrogen(pH=0) is reduced or oxidized. This NHE can be correlated with vacuum energy level as well as other reference electrodes as in figure 1.7. Table 1.1 describes selected redox potentials of well known redox couples.[20]
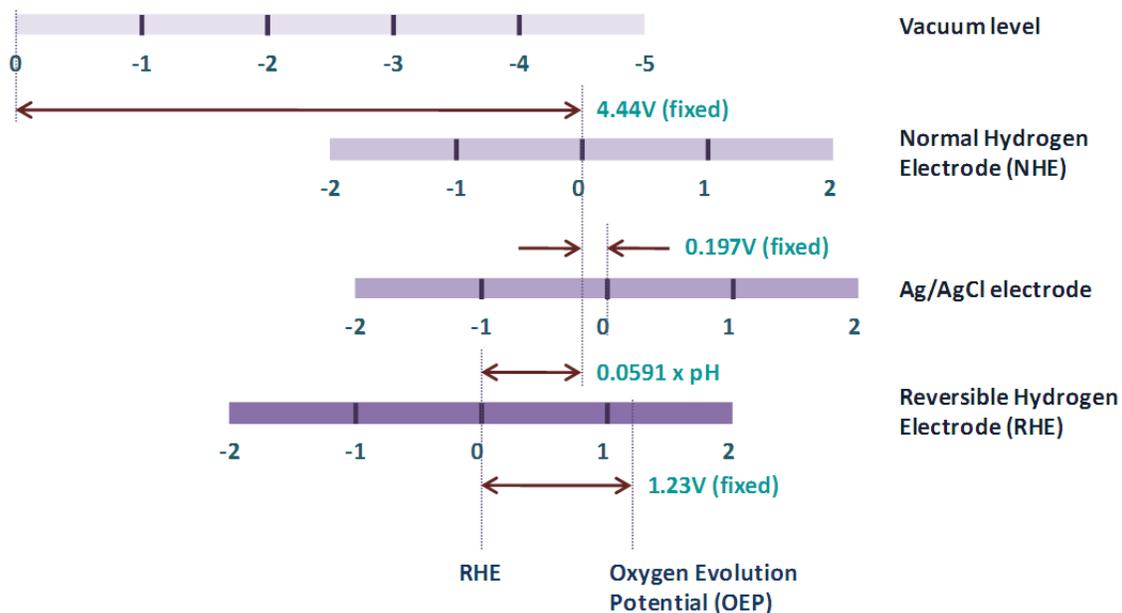
Figure 1.7 NHE and energy scales

Half-reaction	E^0 [V]	Half-reaction	E^0 [V]
$K^+ + e^- = K$	-2.93	$Cd^{2+} + 2e^- = Cd$	-0.4
$Na^+ + e^- = Na$	-2.71	$GeO_2 + 2H^+ + 2e^- = GeO + H_2O$	-0.37
$Mg^{2+} + 2e^- = Mg$	-2.36	$Cu_2O + H_2O + 2e^- = 2Cu + 2OH^-$	-0.37
$Al^{3+} + 3e^- = Al$	-1.68	$In^{3+} + 3e^- = In$	-0.34
$Ti^{2+} + 2e^- = Ti$	-1.63	$Ni^{2+} + 2e^- = Ni$	-0.23
$SiF6^{2-} + 4e^- = Si + 6F^-$	-1.37	$HPO4^{2-} + 2H^+ + 2e^- = HPO3^{2-} + H_2O$	-0.23
$TiO + 2H^+ + 2e^- = Ti + H_2O$	-1.31	$Si + 4H^+ + 4e^- = SiH_4$	-0.14
$Mn^{2+} + 2e^- = Mn$	-1.18	$WO_3 + 6H^+ + 6e^- = W + 3H_2O$	-0.09
$SO4^{2-} + 2e^- + H2O = SO3_{2-} + 2OH^-$	-0.94	$2H^+ + 2e^- = H_2$	0
$SiO_2 + 4H^+ + 4e^- = Si + 2H_2O$	-0.91	$Cu^{2+} + 2e^- = Cu$	0.34
$Cr^{2+} + 2e^- = Cr$	-0.9	$[Fe(CN)_6]^{3-} + e^- = [Fe(CN)_6]^{4-}$	0.36
$TiO^{2+} + 2H^+ + 4e^- = Ti + H_2O$	-0.88	$O_2 + 2H_2O + 4e^- = 4OH^-$	0.4
$2H_2O + 2e^- = H_2 + 2OH^-$	-0.83	$Cu^+ + e^- = Cu$	0.52
$Zn^{2+} + 2e^- = Zn$	-0.76	$I3^- + 2e^- = 3I^-$	0.54
$Ga^{3+} + 3e^- = Ga$	-0.53	$Fe^{3+} + e^- = Fe^{2+}$	0.77
$Fe^{2+} + 2e^- = Fe$	-0.44	$O_2 + 4H^+ + 4e^- = 2H_2O$	1.23

$Cr^{3+} + e^- = Cr^{2+}$	-0.42	$Cl_2 + 2e^- = 2Cl^-$	1.36

Table 1.1 Redox potentials, V vs. NHE.

1.2.1.2 Water splitting reactions at anode and cathode

In table 1.1, two water splitting half reactions are presented with their redox potentials.

When H^+ activity is 1(pH=0):

Cathode: $2H^+ + 2e^- \leftrightarrow H_2(g)$ (0 V vs. NHE)
Anode: $O_2(g) + 4H^+ + 4e^- \leftrightarrow 2H_2O$ (1.23 V vs. NHE)

When OH^- activity is 1(pOH=0):

Cathode: $2H_2O + 2e^- \leftrightarrow H_2(g) + 2OH^-$ (-0.827 V vs. NHE)
Anode: $O_2(g) + 4e^- + 2H_2O \leftrightarrow 4OH^-$ (0.403 V vs. NHE)

Equation 1.1 Water splitting reactions
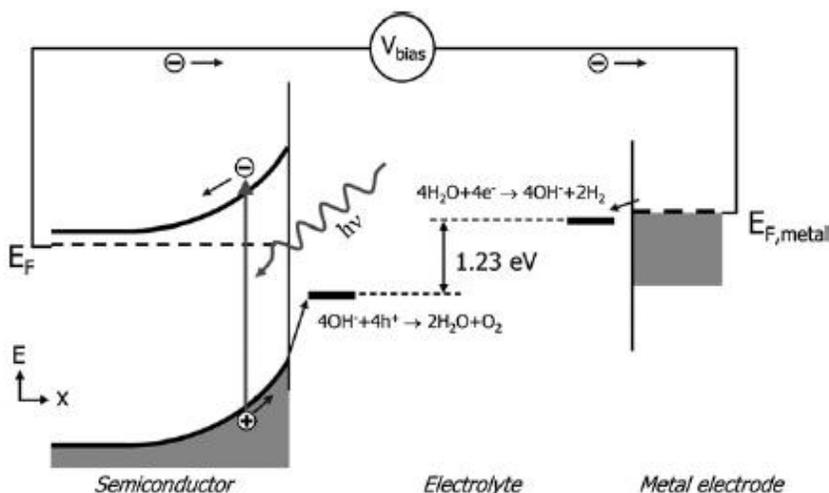
Figure 1.8 Water splitting diagram on energy level consideration

In ideal condition, we need two electrodes with 1.23 V potential difference.(figure 1.8[21]) Anode donates holes to water molecules, therefore produces oxygen gas and protons. These protons are reduced at cathode by higher potential(1.23 V) electrons.

However, there are several non-idealities in real operation. The first is thermodynamic loss. At redox potential, the reactions are in equilibrium so net reaction rate is zero. If small perturbation from the redox

potential is applied to this electrode, either reduction or oxidation starts to be enhanced, but the net generation is still very small. That is, the redox potential only describes the point one reaction starts to be observable, but does not provide any clue of kinetics. Therefore, to achieve meaningful current flow, we need more 'driving force'; more potential than required redox potential should be added. This extra potential is called overpotential. Then, corresponding current(half cell reaction) is formulated as Tafel equation.

$$i = i_0 \exp\left(\alpha \frac{zq\eta}{kT} \right)$$

i_0: exchange current density

α: charge transfer coefficient

z: valence number

q: electron charge

k: Boltzmann's constant

T: temperature

η: overpotential

Equation 1.2 Tafel equation

To enhance the reactions, anode potential must be lowered(shifted toward positive potential) to precipitate hole transfer to electrolyte, while cathode potential must be raised(shifted toward negative potential) for better electron transfer to electrolyte. Figure 1.9 shows net current, which is anodic current minus cathodic current, which is called Butler-Volmer equation, as a function of overpotential for water splitting reaction.[22]
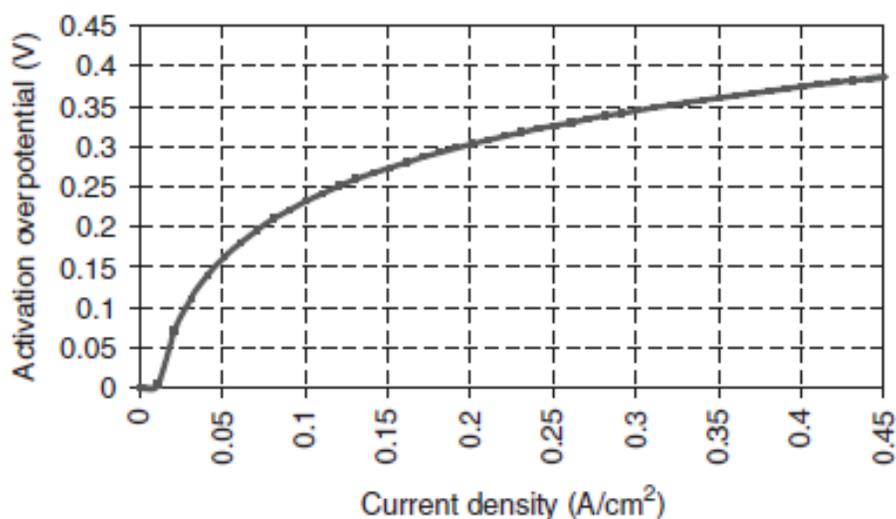
Figure 1.9 Current density vs. overpotential for water splitting

Second consideration is the reaction complexity. In contrast to simple reactions in which only electrons are exchanged, some complex reactions involve reconfiguration of chemical bonds, or intermediate states. Although reactants and products are energetically stable, intermediate products may not be stable due to high energy bonding states. Therefore, these types of reactions have high activation potential which retards overall reaction. Water splitting anode reaction is one of the most difficult reactions.[23] To extract proton, one of the O-H bond must be broken from water molecule which is very stable. At the same time, two of these O-H intermediates must be located in close distance(by probabilistic chance), followed by O-O bond. Finally, remaining hydrogen atoms leave from this secondary intermediate. This complex nature-4 electrons and 4 protons cascade reactions and physical proximity limitation- makes anode reaction a "holy grail" of electrochemistry. This complexity inevitably comes with high overpotential requirement resulting in an intrinsic loss. Thus, it is essential to introduce catalyst. As described in figure 1.10, catalyst can form temporary bond with high energy intermediate, effectively lowering the free energy.
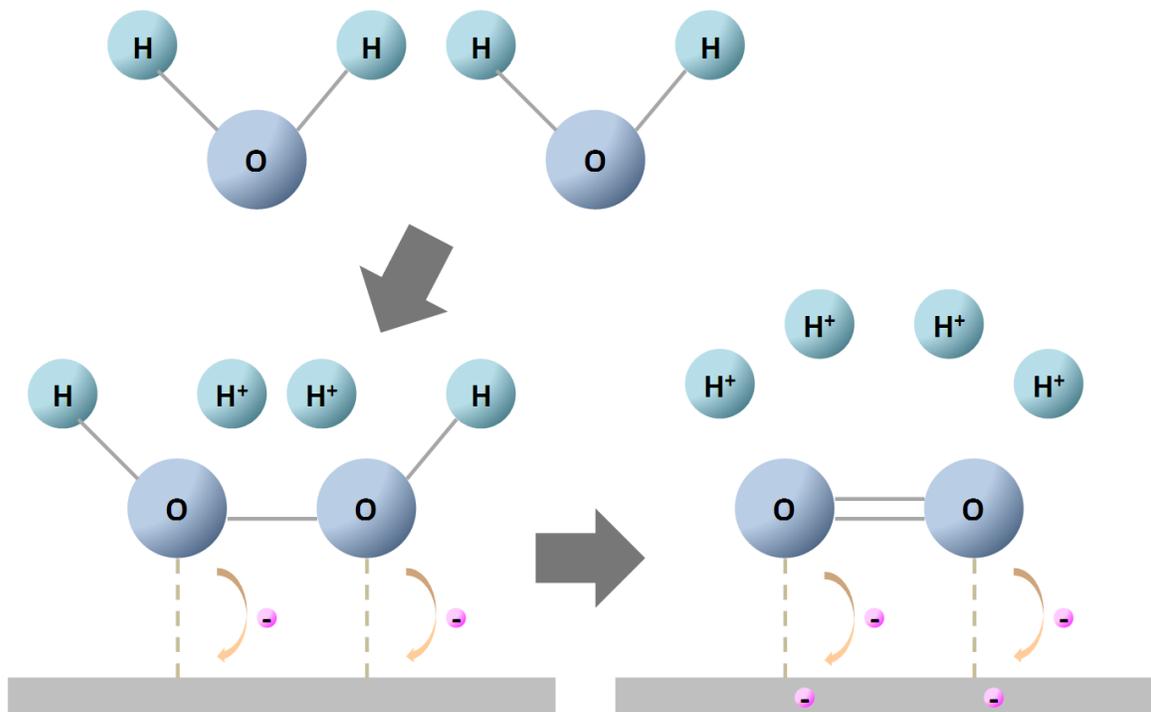
Figure 1.10 Water splitting catalysis of anode reaction

Since catalyst needs to make bridges with dangling bonds of ionic species, transition metal compounds are preferred since their electron configurations are easily changed by d-orbital; generally a transitions metal has several oxidation states. In addition, other factors such as lattice distance and crystal direction also affect the activity. Typically, good catalytic functionality has been shown in noble metals or their compounds including platinum, ruthenium and iridium. Recently, low cost catalysts have been developed like cobalt phosphate[24, 25] and nickel borate.[26]

1.2.1.3 pH dependency

Although redox potentials are unique at a given condition, the values change with respect to electrochemical environment. Indeed, reduction and oxidation are chemical reactions, so changing molar concentrations of the participants changes corresponding chemical potential, which results in new equilibrium point. This relationship is formulated as Nernst equation:

$$E_{red} = E^0_{red} - \frac{RT}{zF} \ln \frac{a_{Red}}{a_{ox}}$$

E_{red}: reduction potential
E^0_{red}: standard reduction potential
R: universal gas constant
T: temperature
z: valence number
F: Faraday constant
a_{red}: chemical activity of reductant
a_{ox}: chemical activity of oxidant

Equation 1.3 Nernst equation

The slope of RT/F at standard condition is 0.0591 V, and if a reaction follows redox potential change of 0.0591 V per log concentration, it is said to follow Nernst relation. In case of water redox reactions, since oxygen and water concentration is assumed constant, the proton concentration is the sole variable of the reaction potential, which can be expressed by pH as in equation 1.4 and figure 1.11.[27]

Cathode: $2H^+ + 2e^- \leftrightarrow H_2(g)$ (0 V vs. NHE)

$$E = 0 - \frac{0.0591}{2} \cdot \log \frac{1}{(a_{H^+})^2} = -0.0591 \cdot pH$$

Anode: $O_2(g) + 4H^+ + 4e^- \leftrightarrow 2H_2O$ (1.23 V vs. NHE)

$$E = 1.23 - \frac{0.0591}{4} \cdot \log \frac{1}{(a_{H^+})^4} = 1.23 - 0.0591 \cdot pH$$

Equation 1.4 Water redox potential in terms of pH
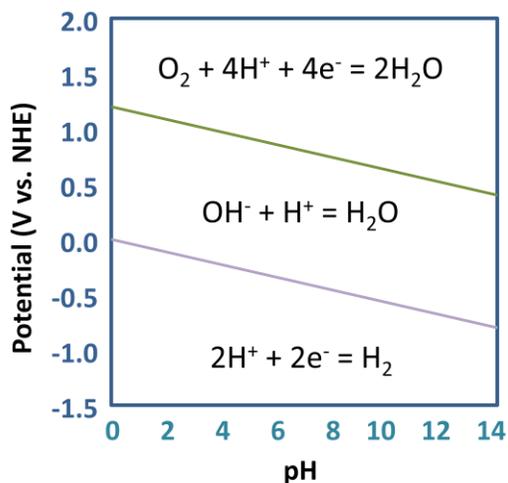
Figure 1.11 Water pourbaix diagram

1.2.1.4 Semiconductor photoelectrode

Photoresponsive semiconductors can generate photovoltages. Photoelectrodes are engineered semiconductor cells to generate desired photovoltages and to supply this electricity to electrolyte. Therefore, the first consideration is semiconductor energy band gap and band edge positions. As described in section 1.2.1.2, the minimum required photovoltage for water splitting is 1.23 V. However, in real operation, the photovoltage must be larger than 1.23 V, to compensate thermodynamic loss and overpotential. Due to this reason, minimum band gap of 1.9~2.0 eV[21] is required. Since this is visible wavelength range on which majority of photocell researches are focusing, seemingly photocells can be readily implanted for photoelectrodes fabrication. However, the nature of electrochemical operation adds more complex criteria which are unnecessary in photocells.

First, band edge position must be aligned with water redox potential. To sustain the oxidation reaction, anode must supply holes to electrolyte. Since most of the holes are concentrated near the valence band edge, valence band edge must locate below water oxidation potential. For the same reason, cathode conduction band edge must be above water reduction potential.

Second consideration is the chemical stability. Photoelectrodes are immersed in water throughout their lifetime. Also, during operation, they are facing corrosive chemical species such as oxygen. These harsh environments limit the spectrum of usable semiconductors.
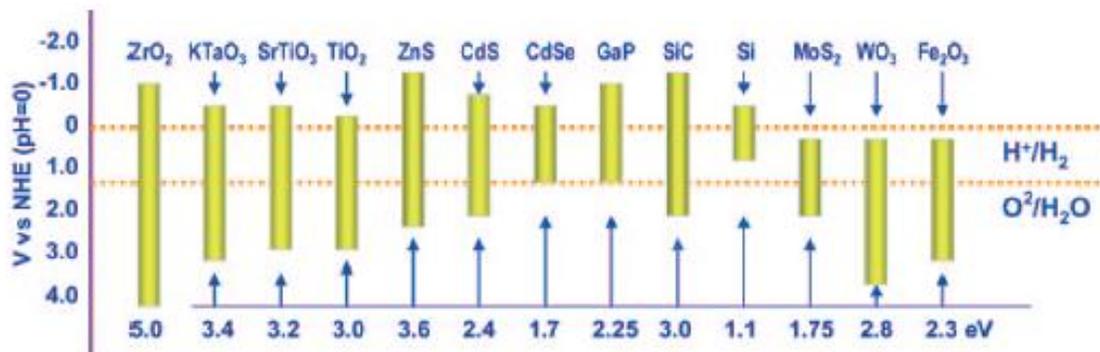
Figure 1.12 Various semiconductors band edge positions.

Figure 1.12[28] lists band gap energies and band edge positions of selected photovoltaic semiconductors relative to the water redox potential at pH=0. High efficiency compound semiconductors(III-V or II-VI) are typically prone to corrosion in water environment. Therefore unless special protective layer is combined, long term operation is easily compromised. In this reason, oxide semiconductors have advantage due to their exceptional stability, but in many cases, they are suffered from inferior photovoltaic properties such as wide band gap or poor electrical characteristics.

Since it is hard to satisfy all the requirements using single semiconductor material, heterojunction or tandem cell construction is currently preferred. Based on this heterojunction concept, researches have been split into photocathodes and photoanodes. On each side, optimum materials and structures are being sought to maximize photocurrent at half cell reaction.

1.2.2 Previous researches

Since the landmark research of the TiO_2 photocatalyst,[29] many efforts have been brought into the performance improvement of photoelectrodes. There are good reviews on various researches and topics regarding photoelectrode fabrications.[21, 28, 30-33] Here, some notable researches will be summarized.

For photoanode fabrication, titanium oxide is still a popular material due to the chemical stability. However, its wide band gap, about 3.2 eV is a general problem since only ultra violet light can be utilized. To activate titanium dioxide or its compound alloy like $SrTiO_3$ under visible light, various cations were doped including V, Mn, Fe, Cr, Sb and Ta.[34-36] Although these cations provide intermediate levels in the forbidden band to allow visible light absorption, they also play as recombination centers which scavenge excited carriers. To minimize the adverse effect, fine control of doping level becomes very important. As

an alternative method, anion doping[37, 38] such as nitrogen and carbon was tried instead and showed improvement in visible light responses, which is believed to be less affected by recombination.

Another issue in titanium dioxide is limited light absorption capability. Titanium dioxide suffers from small absorption cross-section. In addition, the doping into titanium dioxide is typically difficult due to low solubility, subsequently overall light absorption is low even though doped. In this problem, nanostuctured TiO_2 can enhance the light absorption by light scattering inside the matrix, resulting in increased absorption cross-section. Also, photogenerated carriers only need to travel short distance in the range of the shortest length scale of the nanostructure, therefore the chances that carriers are scavenged by recombination could be minimized. For this purpose, researchers fabricated TiO_2 nanostructures with cation or anion doping(figure 1.13(a) and (b)). and showed improved photocatalytic responses compared to their flat film counterparts.[39, 40] In addition, nanostructured heterojunction photoanode using TiO_2 was also fabricated. In this case, thin TiO_2 film was deposited on silicon nanowires array as in figure 1.3(c), which allows improved light absorption as well as expansion of usable solar spectrum by heterojunction combined with narrow band gap semiconductor.[41]
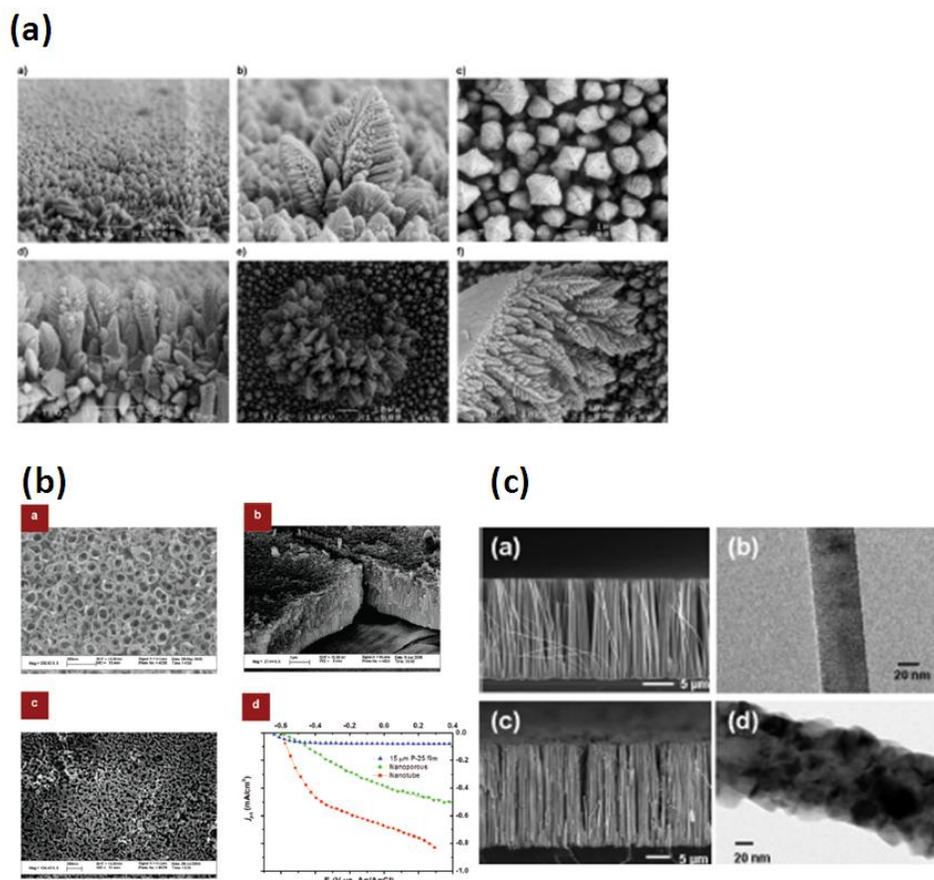
Figure 1.13 (a) TiO_2 nano structure with cation doping, (b) TiO_2 nanotubes with anion doping and (c) TiO_2 catalyzed silicon nanowires.

Tungsten oxide(WO_3) is another interesting metal oxide semiconductor for photoanode. It has narrower band gap(about 2.8 eV) than titanium dioxide. Although WO_3 has the limitation that it is stable only at acidic condition, the nanocrystalline structure(figure 1.14[42]) showed impressive photoelectrochemical responses[42, 43] with high incident photon to current efficiency. Since WO_3 conduction band edge locates below hydrogen reduction potential, tandem structures along with dye sensitized solar cell[31] or silicon solar cell[44] were fabricated to achieve direct water cleavage.
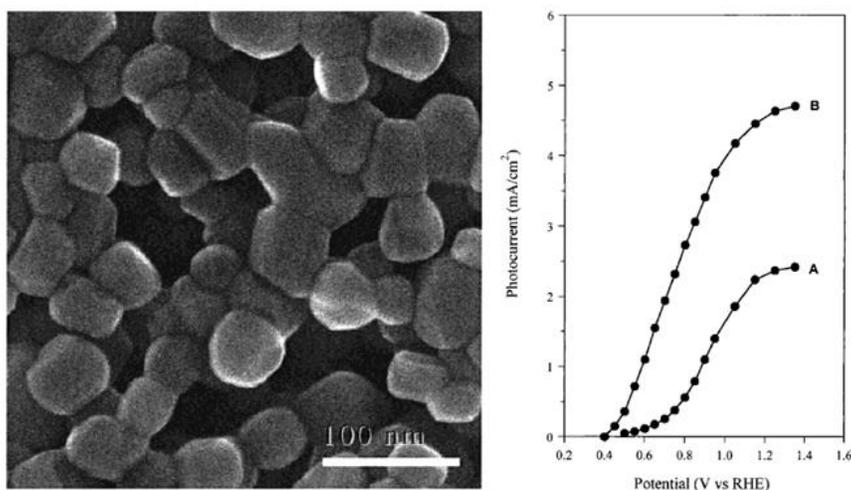
Figure 1.14 WO_3 film and photoresponses in acidic environment.

Recently, iron-oxide(α-Fe_2O_3, hematite) attracts a great attention as a prospective photoanode material.[33] It has the narrowest band gap(about 2.1 eV) among popular metal oxide semiconductors as well as generally good chemical stability except strong acid. The biggest problem is its short hole diffusion length; it is known that hole diffusion length is only about 2~20 nm. However, since doping is found to effectively increase the carrier density and conductivity, the performance of iron-oxide photoanode has been significantly improved. Dopants including Mg, Cu, Zn(p-type), Ti, Sn, Zr, Si, Ge(n-type)[33, 45-47] are well known for improving photoelectrochemical properties of iron-oxide by substituting Fe site and donating carriers.

In addition to electronic modifications, structural manipulation has been applied to iron-oxide. Aluminum is not directly involved in carrier donation, but Al doping helps iron-oxide crystal structures to be directed into certain favorable way,[48, 49] for example reduced Fe-Fe distance which precipitates hopping. Also, similar to TiO_2 cases, nanostructured iron-oxide improves photocarrier harvesting. Flake-like nanocrystal(figure 1.15(a))[50], dendrite shape[51] or meta-stable phases[52] were achieved by simply

doping Si during chemical vapor deposition growth. Other trials including iron-oxide coated nanonet(figure 1.15(b))[53] and 1D wires structures(figure 1.15(c))[54, 55] were another approaches for nanostructured iron-oxide.

Surface treatments were also demonstrated to affect the iron-oxide properties in various ways. Fluoride treated iron-oxide experienced flat band potential shift,[56] so no bias was necessary for water splitting. Conventional, but still robust co-catalyzing method also helps to decrease onset potential.[51, 57, 58] By this way, high photocurrent more than 3 mA/cm^2 has been achieved by iridium-oxide decorated iron-oxide(figure 1.15(d))[57].
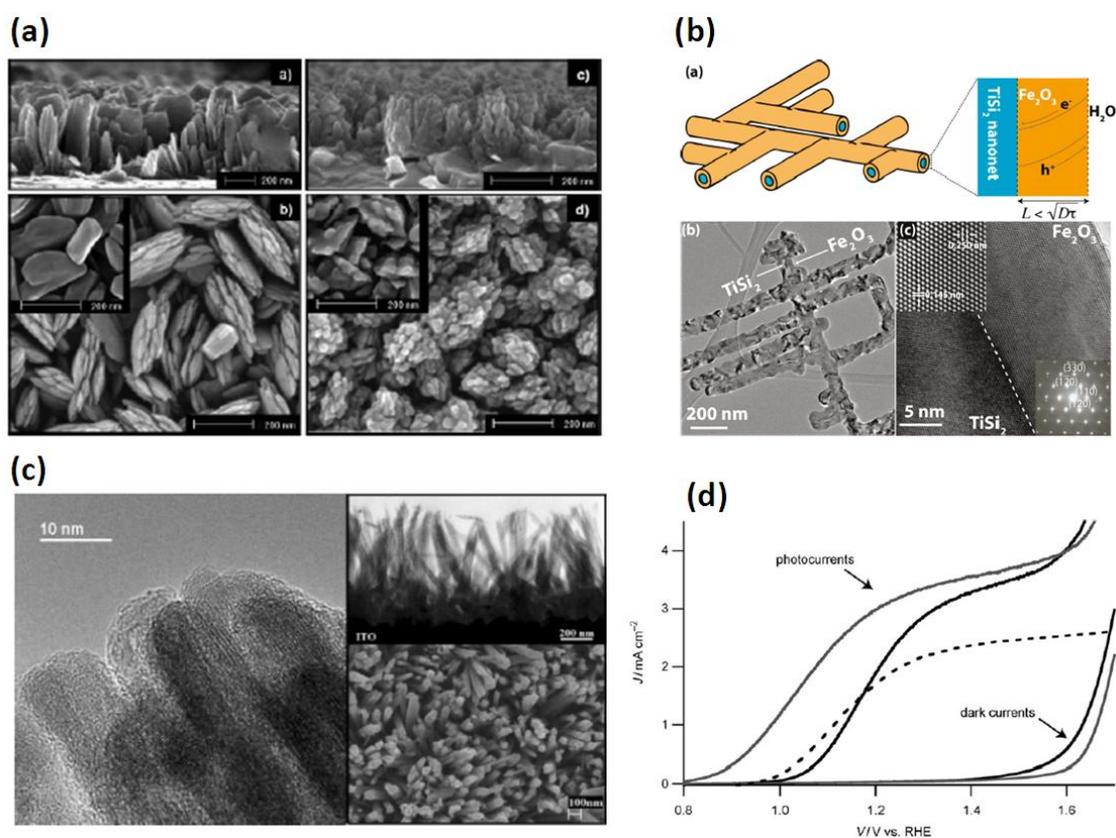
Figure 1.15 Iron-oxide nanostructured photoanodes. (a) flake-like nanostructure, (b) silicide nanonets coated with iron-oxide, (c) iron-oxide nanowires and (d) photoresponse of iridium-oxide co-catalyzed iron-oxide photoanode.

Cathode reaction requires much lower overpotential, so are readily achieved by inert metallic electrodes. However, to practically replace high cost noble metals as well as to facilitate additional potentials provided by photogenerated carriers, photocathodes are also explored by researchers. Although photocathodes are also exposed to water environment, the hydrogen-evolving nature provides some

protection against corrosion mainly induced by oxygen. This allows more flexibility of materials choice. For example, p-type silicon photocathodes decorated with platinum(figure 1.16(a)) successfully demonstrated high current density more than 20 mA/cm^2.[59] Recently, cuprous-oxide photocathode with thin zinc-oxide and titanium-oxide protection layer showed high performance(> 7 mA/cm^2) as well as good stability for extended operation time(figure 1.16(b))[60].
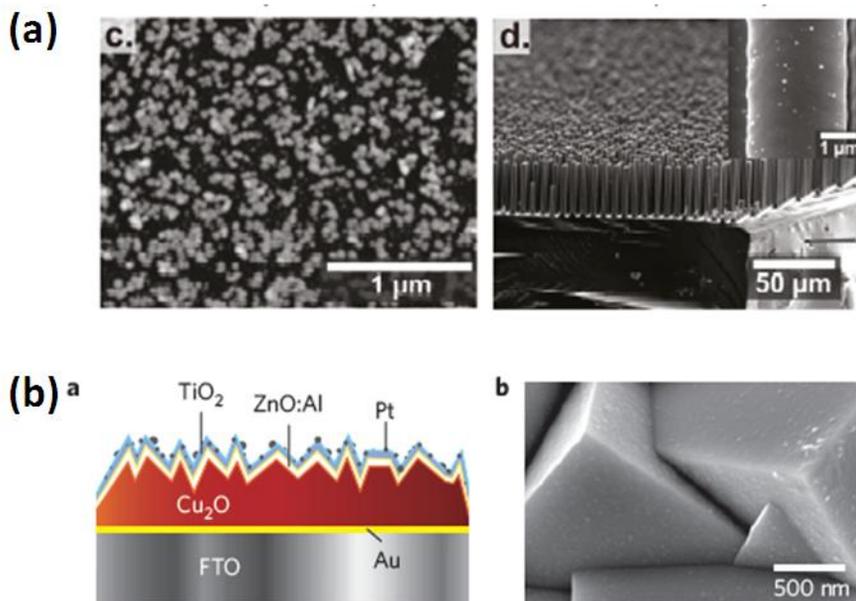
Figure 1.16 Various photocathodes. (a) silicon wires photocathode catalyzed by platinum and (b) cuprous oxide photocathode with protection layers.

The structures described above are fundamentally semiconductor-to-liquid junction. Semiconductor mobile carriers are directly interacting with ions in the electrolyte. On the contrary, there are groups of researches using the structure of photocell combined with electrolyzer. The photocell is made of photovoltaic semiconductors. At each end of the photocell, current collectors(metallic electrodes) are located and electrolysis catalysts are deposited on these electrodes. Sometimes, the current collectors themselves are made of catalysts like platinum. In this structure, semiconductor photocells are fully hidden under the electrodes. This approach prevents corrosion by semiconductor-to-liquid contact, thus allows such semiconductors as silicon and III-V semiconductors as shown in figure 1.17.[61-67] Since high performance photocells can be embedded, high photocurrent more than 13 mA/cm^2 has been achieved using GaInP$_2$/GaAs/Pt stack without the necessity of additional bias for full cell reaction.[64] Even with multijunction amorphous silicon solar cell and platinum catalyst, 6 mA/cm^2 current density or 7.8 % solar-to-hydrogen conversion efficiency has been achieved.

(a) H$_2$ O$_2$ — Oxygen catalyst / Hydrogen catalyst — Multijunction photocell — Transparent protective film

(b) A — I — Pt — p-GaAs — n-GaAs — p-GaInP$_2$ — Ohmic contact — Interconnect

(c) a Photohydrolysis System
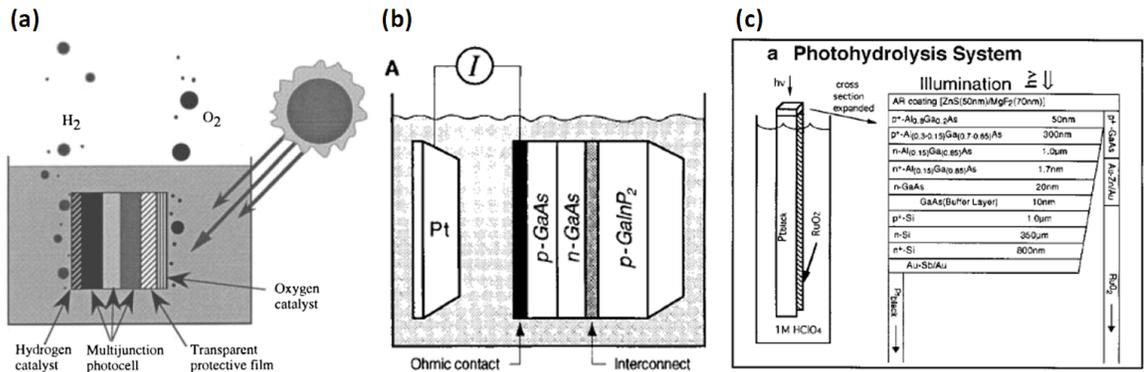
Figure 1.17 Photocell and electrolyzer structure. (a) suggested basic scheme, (b) III-V semiconductor system and (c) multijunction III-V and silicon tandem cell structure.

The drawback of this structure is unavoidable loss by catalyst overpotential. In case of semiconductor-to-liquid junction, upward(anode) or downward(cathode) band bending of semiconductors contributes to decreased overpotential. However, in electrolyzer structure, at least one electrode has no intimate contact between semiconductor and liquid, but catalyst or metal electrode makes contact with liquid. Therefore, the unique current versus potential characteristic of the catalyst is inherited regardless of the photocell. The high output of the photocell may overdrive the current curve resulting in high photocurrent, but significant amount of this electric output is wasted to overdrive the overpotential.

Chapter 2   Research outline

2.1 Overview

To pursue practical pathway toward recyclable hydrogen generation by water splitting, both high efficiency photoanode and photocathode must be developed simultaneously. Due to simple reaction nature, cathode reaction can be achieved at low overpotential using various common electrode materials including metals and semiconductors. However, anode still needs a lot of improvement. Therefore, this research particularly aims to fabricate and characterize high efficiency photoanode. In previous chapter, the concept and general mechanism of semiconductor based solar water splitting were presented. In this chapter, issues and plans on practical photoanode fabrication will be discussed ranging from materials choice to physical construction.

For full cell reactions, the foremost consideration is energy band gap, since cell voltage must be larger than 1.23 V. However, if only anode reaction is considered, this precondition can be released. Therefore, using optimal materials and constructions for anode half cell reaction, this research will focus on high efficiency semiconductor photoanode fabrication.

2.2 Materials choice

2.2.1 Silicon photoanode

Silicon is widely used for photovoltaic applications, since it can absorb wide range of solar spectrum up to near infrared light. Also, high quality silicon of both crystalline and amorphous phase can be readily prepared, which minimizes loss due to unwanted carrier recombination. The matured technologies as well as abundance in earth crust can maintain production cost relatively low compared to other exotic semiconductors. These all advantages make silicon an attractive option for photoelectrode.

However, silicon is thought to be unsuitable for use as a water splitting photoanode due to two reasons. One is the high valence band edge position. As shown in figure 1.12, silicon valence band edge locates higher than oxygen evolution potential, which prohibits holes from being transferred to water molecule. Due to this fundamental problem, silicon has been generally used as secondary layer in tandem cell instead of direct liquid junction. Other semiconductors, which have band alignment, are typically deposited on silicon and exposed to liquid electrolyte.

The key to resolve this problem is the unique pH response of silicon. Most of metal oxide semiconductors show Nernst relation with respect to pH, that is, the flat band potential shifts -0.0591 V/pH. At the same time, water redox potential(both anode and cathode) shifts -0.0591 V/pH, too. Therefore, the relative positions between semiconductor band edges and water redox level remain unchanged regardless of pH. However, silicon behaves differently. Ionic species tends to be adsorbed on silicon and alters relative energy levels,[68] which is not observed in other semiconductors. This phenomenon induces lowered pH sensitivity in silicon than Nernst relation. In one research by Madou,[69] the slope was measured to be about -0.03 V/pH in $Fe(CN)_6^{4-}$ based aqueous electrolyte. Another report[70] in NaCl electrolyte says the slope reaches as high as 0.04 V/pH and decreases near the point of zero charge. Although slopes vary slightly depending on electrolytes, they are flatter than Nernst relation. This implies that the energy level mismatch between silicon valence band and oxygen evolution potential would be decreasing at high pH. Considering photoanode operation is typically conducted at high pH for better conversion activity,[71] it is very probable that silicon meets required band alignment at the operation condition.

Second problem is the lack of catalytic functionality. Water oxidation requires high activation potential due to its reaction complexity. However, in contrast to transition metals, silicon does not have reconfigurable electron structure to hold high energy intermediate species. Rather, the surface is easily encapsulated by passivation oxide. This cannot be solved by silicon itself, but necessitates another catalyst layer. It will be discussed in the following section.

2.2.2 Iron-oxide catalyst

As a photoanode material, iron-oxide, especially hematite(α-Fe_2O_3) is viewed as a promising material due to its optimal band gap(2.1~2.2 eV), which covers about 40 % of solar spectrum, and low valence band edge position. Also, iron-oxide has good chemical stability in wide range of pH as shown in figure 2.1.[72] By introducing dopants, co-catalysts and compound alloys, its photoelectrochemical properties are being improved as described in section 1.2.2.
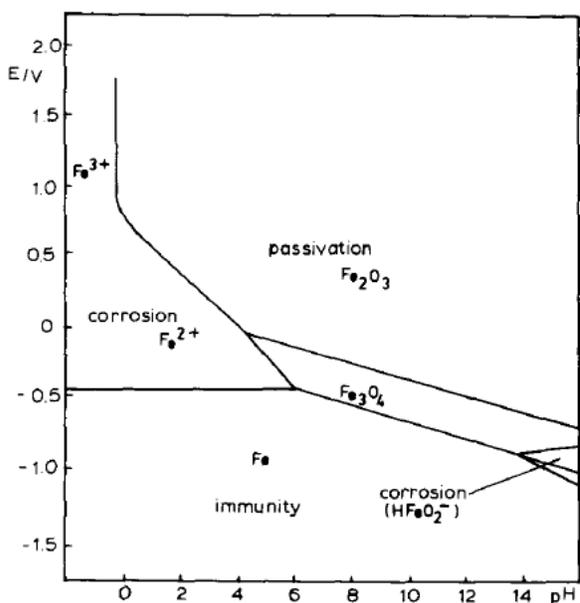
Figure 2.1 Iron oxide Pourbaix diagram.

However, it is still in question whether iron-oxide possesses good catalytic functionality. Although not many, there are reports regarding the oxygen evolution performance of iron-oxide or its transition metal compound oxides,[73] which result in poor performance compared to nickel or cobalt based catalysts. However, these relatively thick film configurations are likely suffered by the intrinsic problem of short hole diffusion length. In reports[51, 57] in which doping and nanostructure were applied to minimize the loss by short hole diffusion length, iron-oxide shows decent to good performance. Although co-catalyst helps to improve performance, the performance improvement made by this co-catalyst decoration is not a exceptionally remarkable. This implies that well engineered iron-oxide can show fairly acceptable catalytic functionality among alternative catalysts group to noble metals.

Therefore, iron-oxide and silicon hybrid photoanode will be the base structure of this research. Since it is believed that the photoresponse of silicon is better than iron-oxide, our priority would be to dedicate the role of iron-oxide to catalysis. There are reports[74-77] about similar hybrid structure, which show that it is possible but not enough to compete with other high performance photoanodes. To make a breakthrough, we will conduct more in-depth investigation based on various parameters, which includes physical film configuration as well as chemical compositions. Since doping is considered to enhance electrical properties, titanium will be used as a dopant, which seems to work best among reported elements.[47, 78]

2.3 Silicon microfabrication

In this research, silicon substrate plays as the primary light absorption and photocarrier generation layer. Also, all the electric transport is made through silicon layer. Therefore, while materials choice sets the theoretical upper limit of photovoltaic process, performance loss is expected to stem mostly from non-ideal aspects of silicon substrate. Fortunately, tremendous amount of researches has been conducted to understand and improve electrical performances of silicon, and this is one of the most important reasons silicon possesses the dominance in photocell applications.

First consideration is Schottky contact between silicon and metal wiring. On the silicon surface, there are many dangling bonds and defect sites compared to crystalline body. Therefore, this inequality of carrier density contributes to spontaneous band bending, like upward bending of n-type silicon and downward bending of p-type silicon. Common metals used in metallic contact have relatively large workfunctions.[79] Therefore, although it is easy to find good ohmic contact metals to p-type silicon, n-type silicon usually forms Schottky contact. Therefore, we need additional potential to overcome this Schottky barrier, which means loss of potential.

The most effective method to minimize Schottky behavior is to form shallow high doping layer.[80] When the doping level is high enough, space charge region gets very thin, so carrier can readily tunnel the barrier. To create shallow n+ doping, spin-on dopant will be used in this research. The process is simpler than ion implantation, but very effective especially when high surface doping level is necessary.

Second consideration is light absorption of silicon substrate. Reflected light is directly the loss of photogenerated carriers. Therefore, in photocell design, various structural solutions have been suggested including antireflection layers and surface texturing. Unfortunately, since silicon surface should make a intimate contact to liquid, it is hard to introduce antireflection layers. However, roughened surface may be not only applicable, but beneficial in several aspects. One advantage is increased surface area, and as a result, decreased current density per unit film area. As seen in Tafel equation, electrochemical current density is exponentially affected by overpotential. Therefore, by decreasing current density, required overpotential also decreases minimizing thermodynamic loss. Second advantage is the reduced carrier diffusion path length. As Atwater, Lewis and coworkers proved,[81-84] high aspect ratio wire structure requires the path length on the order of wire diameter. Consequently, unwanted carrier recombination can be reduced significantly. Also, this potentially allows low quality silicon usage whose diffusion length is much shorter than high quality silicon, further reducing the production costs. In this respect, this research will adopt a vertical wires array for silicon substrate. Various microfabrication techniques such as wet chemical silicon etching and chemical vapor deposition will be discussed and conducted to create large area and uniform silicon wires array.

2.4 Experimental plan

Based on materials and structural considerations, this research aims to pursue high efficiency photoanode fabrication using the cells in the following diagram.
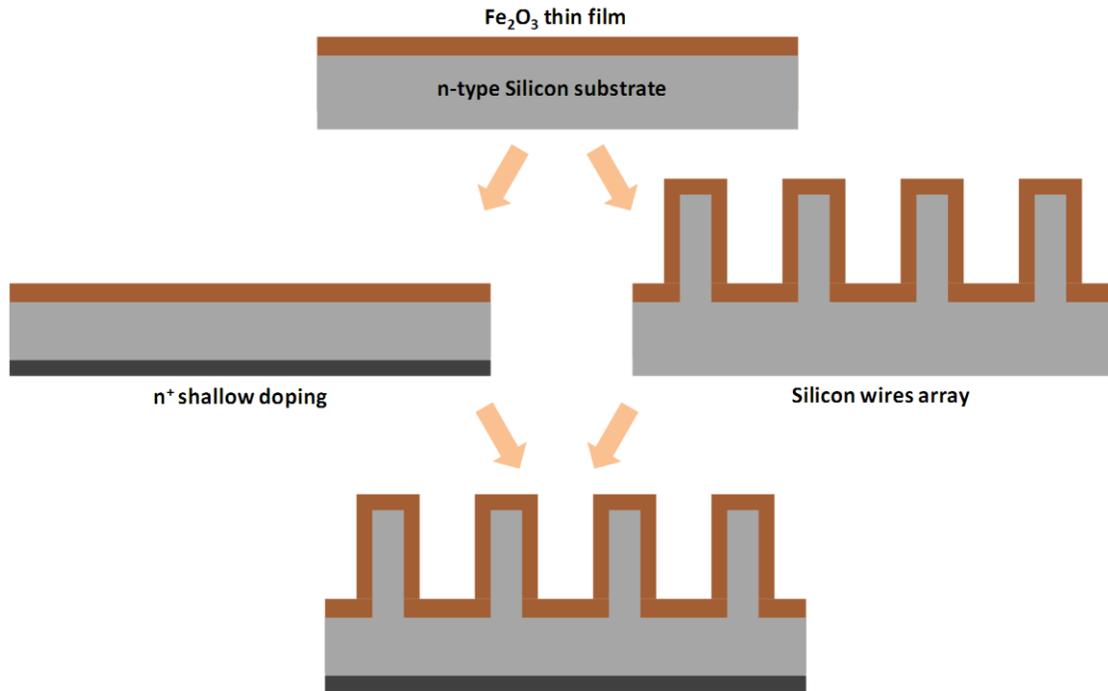
Figure 2.2 Cell structures in this research.

For the first step, experimental conditions for functional iron-oxide film deposition would be searched. The ultimate structure in figure 2.2 requires conformal deposition of iron-oxide. Among many deposition methods, atmospheric pressure chemical vapor deposition(CVD) satisfies this requirement with simple experimental setup. This CVD iron-oxide will be on n-type silicon since holes are minority carriers for photoanode reaction. Initially, flat and untreated n-type silicon will be used to measure photoelectrochemical performance and to see feasibility. CVD film properties are very sensitive to environment and deposition conditions. Therefore, film deposition, chemical characterization and photoresponse measurement will be conducted in iterative manner.

Once iron-film is optimized, microfabricated silicon structure will replace untreated silicon substrate. n^+ back doped silicon and/or vertical silicon wires array will be fabricated and applied to the photoanode device for improved performance. Afterward, the observed phenomena will be explained via analytical measurements and theoretical modeling.

Chapter 3　　Silicon photoanode device fabrication

3.1　Overview

In this chapter, all the experimental setups including device fabrication processes will be described. Section 3.2 summarizes most of the protocols except silicon wires array fabrication. In this research, silicon wires array was fabricated by wet etching of silicon wafer. However, as a potentially cost-effective method, CVD silicon wires growth is a noteworthy option. Therefore, section 3.3 will be dedicated to silicon wires growth process both in wet etching and CVD growth.

3.2　Silicon and iron oxide hybrid photoelectrode fabrication

3.2.1　Substrate preparation

3.2.1.1　Plain silicon substrate

Silicon electrodes were made of 4" n-type phosphorous doped (100) direction silicon wafer.(resistivity 5~25 Ω-cm, thickness 500~550 μm, Wafernet) Front surface of the wafer was first protected by photoresist(S1805, Shipley) spun at 2000 rpm and 40 seconds, followed by dicing into 1 cm by 1 cm pieces using diesaw(DAD-2H/6T, Disco Abrasive System). The pieces were cleaned in acetone, isopropyl alcohol(IPA) and finally deionized water(DIW) with ultrasonic agitation to remove photoresist, organic contaminants and silicon particles generated during dicing. Just before CVD, the native oxide was etched by 1:10 hydrofluoric acid(HF, 49 % wt., J.T. Baker):DIW solution for 1 minute. For temporary storage, these cleaned pieces were placed inside a nitrogen box.

3.2.1.2　Ohmic contact silicon substrate

The wafers with the same specification were used for ohmic n^+ back doping. The wafers were cleaned by organic solvents and HF. Front surface was protected by spin-on glass(SOG, IC1-200, Futurrex). SOG was spun for 40 seconds at 3000 rpm, followed by baking at 100 ℃, 60 seconds and 200 ℃, 15 minutes. Spin-on dopant(SOD, P509, Filmtronics) was spun on backside of the wafer for 40 seconds at 3000 rpm. This wafer was baked for 15 minutes at 200 ℃.

Dopant diffusion was conducted in an oxidation tube furnace(6" diameter, Lindberg) which consists of three zones with measuring thermocouples. Gas flow was controlled by mass flow controllers(MFCs)

to 6 liter per minute(lpm) nitrogen and 2 lpm oxygen. First, without wafer loading, the furnace was ramped up to 600 C. Then, quartz wafer cassette was loaded in the furnace. Sample wafers were placed in the center of the cassette, while 5 dummy wafers were place at both sides of the samples to prevent direct gas flow to the samples. After loading, temperature was increased 100 ℃ every 5 minutes until 900 ℃, and maintained for 30 minutes. After the diffusion, furnace was cooled down to 600 ℃ by natural cooling,(measured cooling rate about 18 ℃/minute) and wafers were removed at this temperature.

After process, SOD and SOG were stripped by 1:4 HF:DIW solution for more than 10 minutes. If the wafer was supposed to be used for flat substrate, the wafer was diced into 1 cm by 1 cm pieces with the same process described in plain silicon substrate preparation. If the wafer was for wires array fabrication, the full wafer was transferred to the next step.

3.2.1.3   Silicon wires array fabrication

Silicon wires array was fabricated by electroless chemical etching. To see the differences, both untreated wafers and n^+ back doped wafers were used to fabricate the array. All the topics regarding silicon wires array fabrication are presented in section 3.3 in details.

3.2.1.4   Other substrate

To measure catalytic effect of iron-oxide film, other metallic substrates were also prepared.

25 mm by 25 mm indium tin oxide(ITO) coated glass sheet(R_s = 15 ~ 25 ohm / square, thickness 1.1 mm, Delta Technologies) was protected and diced into 1 cm by 1 cm pieces similar to silicon substrate. Also, before iron-oxide deposition, acetone, IPA and DIW cleaning were conducted.

Platinum substrate was prepared on oxidized silicon wafer(4", (100) n-type silicon with 200 nm thermal oxide). On this wafer, 10 nm titanium and 20 nm platinum was deposited by sputtering machine(Orion 5, AJA International). The wafer was cut into desired size pieces for sample preparation.

3.2.2 Iron-oxide film deposition

CVD setup is home built one as shown in figure 3.1, which adopts similar setups reported elsewhere.[51, 85]
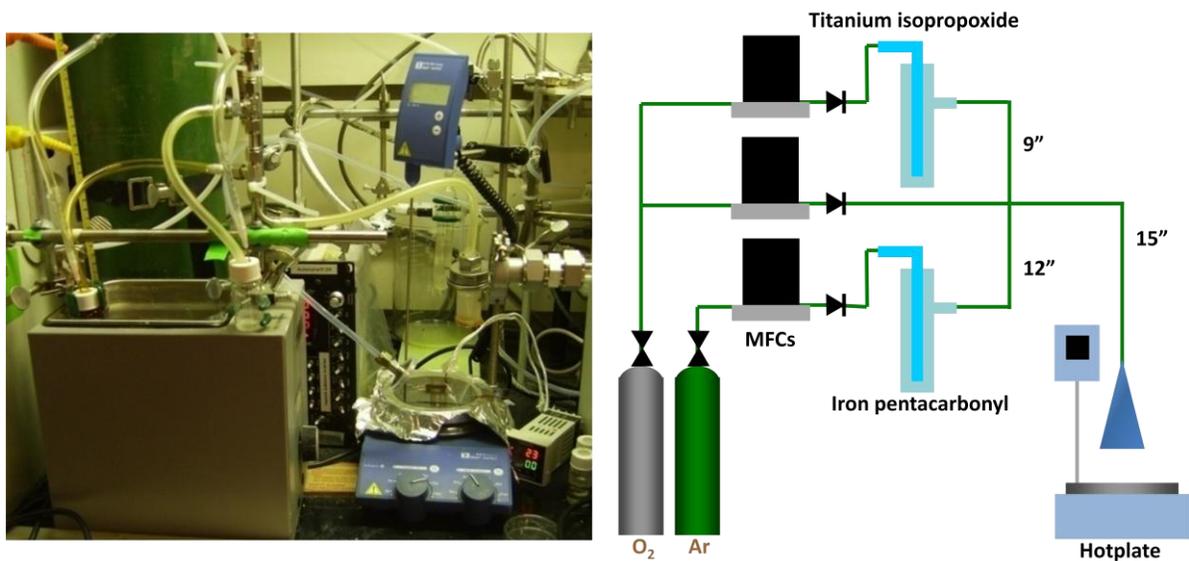
Figure 3.1 CVD setup, picture(left) and schematic diagram(right)

The setup is composed of two bubblers and three MFCs(1479A, MKS Instrument). Bubblers are made of 20 ml glass vials with rubber septum. Gas inlet is 18 gauge syringe needle with ethyl vinyl acetate tubing(0.03" I.D., 0.09" O.D., Microline) extended to the bottom, while gas outlet is Tygon tubing(0.25" I.D., 0.375" O.D., Saint Gobain). At each bubbler, 10 ml of iron pentacarbonyl(Fe(CO)$_5$, Sigma-Aldrich) and 10 ml of titanium isopropoxide(TTIP, Ti(OCH(CH$_3$)$_2$)$_4$, Sigma-Aldrich) were contained. Iron pentacarbonyl was chilled in cold water bath maintained at 5 ℃ and titanium isopropoxide was in room temperature.(20 ℃) The carrier gases were argon(iron pentacarbonyl) and oxygen(titanium isopropoxide), respectively. The gas outlets from two bubblers were joined by another oxygen line, and connected to a glass funnel(an enlarging glass adapter, 14/20 to 24/40). Gas flow rates were changed to find optimal condition, which turns out to be 10 standard cubic centimeter per minute(sccm) argon for iron pentacarbonyl, 250 sccm oxygen for titanium isopropoxide and 350 sccm extra oxygen. For all the conditions, iron pentacarbonyl carrier flow rate was maintained the same, however, titanium iropropoxide carrier flow rate was adjusted. In this case, extra oxygen flow rate was also adjusted, so total flow rate was unchanged(610 sccm).

Deposition was made on a hotplate surface. To minimize temperature variation over the heated surface, a dummy silicon wafer was placed on the hotplate. In the middle of this wafer was placed a glass support, which is 25 mm wide square assembly of 1 mm thick slide glass sheets as shown in figure 3.2.
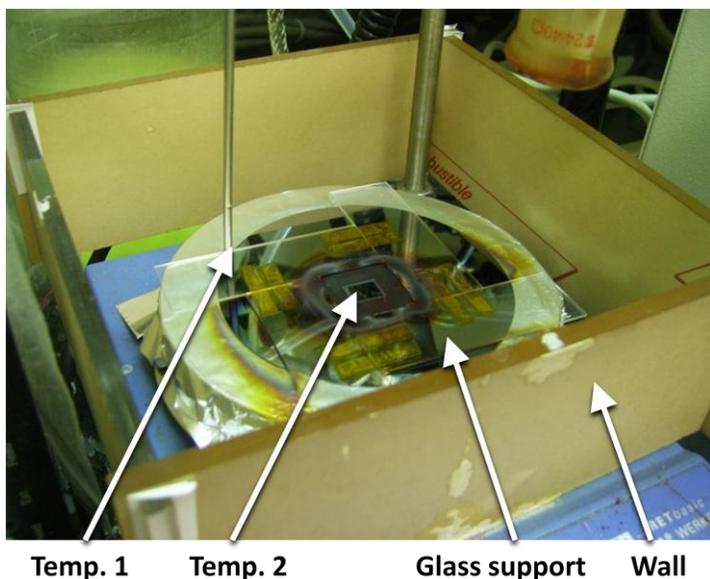
Figure 3.2 Detailed picture near hotplace surface. Two temperature measurement points, glass support and plastic wall.

Temperature measured by thermocouple is described in figure 3.2 and table 3.1. Due to airflow and conduction in hotplate, the setting value and measured temperature show non negligible discrepancy. For convenience, the experimental conditions will describe 'setting temperature'. However, the real temperature should read the corresponding measured value. Except the parametric studies about temperature, all the samples were prepared at 250 ℃ setting temperature.

Setting temperature	Measurement in point 1	Measurement in point 2
250	180	173
270	193	187
290	203	202

Table 3.1 Measured temperature, unit ℃.

Sample substrate was put in the center, and the funnel was placed over the glass support for designated time. Typically, the deposition time was 10 minutes or less.

The whole setup was placed in a hood for safety reason since iron pentacarbonyl is toxic material. To prevent the fluctuation by airflow, plastic wall was installed around the hotplate.

3.2.3 Device fabrication

Sample substrates with iron-oxide film was wired and packaged by following processes. First, the backside of silicon substrate was shortly(1 minute) cleaned by 1:10 HF:DIW solution. Right after this cleaning, 7 nm aluminum and 50 nm silver were deposited in order using thermal evaporator. Silver wire with 0.5 mm diameter was attached to the metal contact by silver paint(silver in MIBK, Ted Pella) and dried for 30 minutes at 70 ℃. Afterward, silver wire was insulated by Teflon tubing, and whole assembly was placed in a slide glass sheet. Epoxy was used to encapsulate all the back and side area for insulation from electrolyte except iron-oxide film surface. The epoxy was cured for more than 2 hours at 70 ℃. To remove organic contaminants, this device was cleaned by ozone(Aqua-6 ozone generator, A2Z Ozone) for 10 minutes. Figure 3.3 shows the picture of completed device.

Electric contact to metallic surface could not be made on the back side. Instead, during iron-oxide deposition, part of the substrate was masked by cover glass so metallic surface was exposed even after iron-oxide deposition. Then, silver wire was attached to this exposed area with silver paint. Epoxy encapsulation was similarly conducted around this sample.
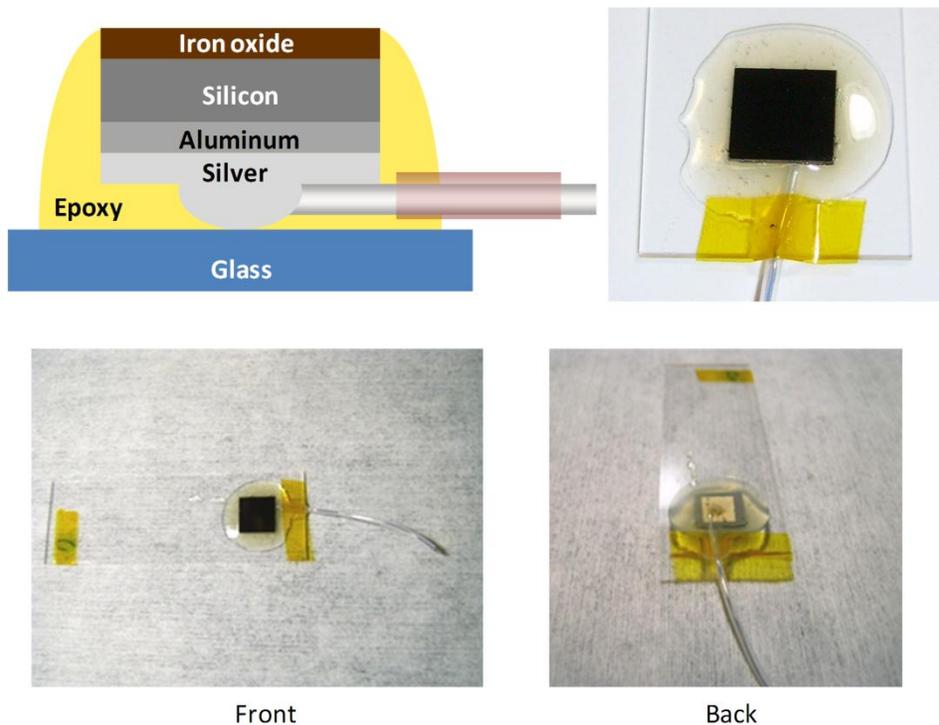
Figure 3.3 Completed device.

3.2.4 Electrochemical setup

Four different electrolytes were prepared by *in-situ* pH measurement(SevenMulti, Mettler Toledo). Highest pH was prepared by 1 M of sodium hydroxide(NaOH, Sigma-Aldrich) in deionized water.(18 ohm-cm) The measured pH was 13.8. Lower pH needs only tiny fraction of NaOH, but in this case, solution conductivity might be significantly lower than 1 M NaOH. To guarantee conductance, buffer solution was prepared using 0.5 M disodium hydrogen phosphate(Na_2HPO_4, Sigma-Aldrich), and titrated by NaOH solution to make pH 12 and 10. The pH of intrinsic Na_2HPO_4 solution is around pH=8~9. Therefore, to make acidic buffer(pH=6), potassium dihydrogen phosphate(KH_2PO_4, Sigma-Aldrich) 0.5 M solution was prepared and titrated by NaOH solution. These solutes were chosen because they are inert in our operation potential. Table 3.2 shows the summarized electrolyte contents.

pH	NaOH [mol/L]	Na_2HPO_4 [mol/L]	KH_2PO_4 [mol/L]
6	>0	0	0.5
10	>0	0.5	0
12	>0	0.5	0
13.8	1	0	0

Table 3.2 Electrolyte contents

Teflon jar containing 200 ml of the buffer solution was used as electrochemical cell. Three electrodes configuration was adopted for electrochemical measurement as shown in figure 3.4.
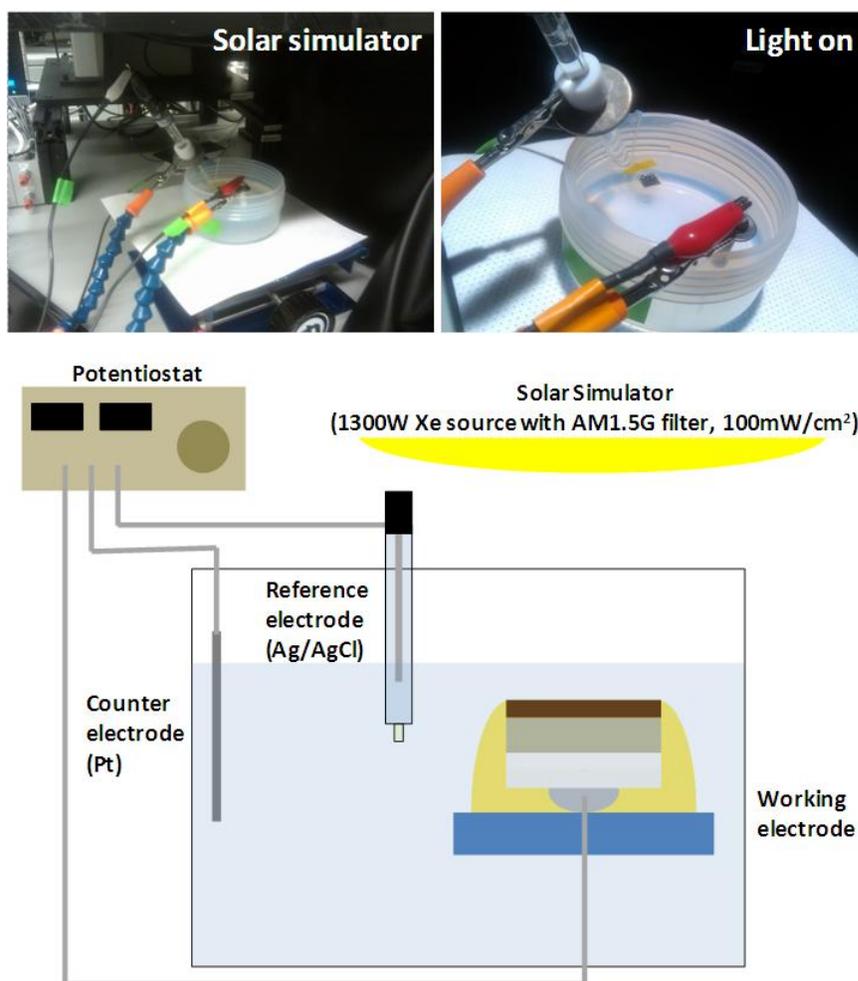
Figure 3.4 Electrochemical configuration.

Our silicon photoanode was working electrode. Silver-silver chloride(Ag/AgCl) reference electrode(Pine Instrument) and platinum wire were used as reference and counter electrode, respectively. The three electrodes were connected to potentiostat which was controlled by PC. For general DC sweep measurement, DY2311 potentiostat(Digi-Ivy) was used, while Reference600 potentiostat(Gamry) was used for AC impedance measurement. This whole setup was placed under a solar simulator(Model 91194, 1300 W Xe source with AM 1.5G filter, Newport Oriel) calibrated to 100 mW/cm^2 using an NREL-certified silicon reference cell equipped with a BK-7 window. The solar simulator was warmed up for more than 15 minutes in advance to stabilize the output.

Unless specially mentioned, all linear sweeps were conducted from cathodic(negative) to anodic(positive) potential at 50 mV/s rate. Also, no particular gas purging or stirring were conducted except gas evolution measurement experiments.

3.2.5 Materials characterization plan

Micrograph images were taken by scanning electron microscope(SEM, DB-235 dual beam machine, FEI) with 45 degree stage tilting.

Crystallographic information was obtained from X-ray diffraction(XRD, PANalytical X'Pert PRO MPD) with 45kV Cu kα source. Thin film signal was too weak to identify the meaningful signal. Therefore, thicker film(about 360 nm thick) was particularly prepared for XRD measurement.

Chemical composition and atomic bonding information was analyzed by X-ray photoelectron spectroscopy(XPS) measured by ESCALAB 250 XPS spectrometer(VG Scientifics) with 15 kV Al kα source.

Electrical resistivity of iron-oxide film was measured by semiconductor analyzer with four-point probes.

3.3 Silicon wires fabrication

Vertical silicon wires array plays a role as a substrate for photoanode catalyzed by iron-oxide. The required wire diameter is not very small; from Atwater and colleagues' research,[83] size range on the order of micrometer is optimal, which can be readily reproduced by many patterning techniques.

In this research, wet electroless etching method will be adopted since it provides advantages such as large area compatibility, relatively low contamination and fabrication easiness in our limited facilities. However, alternative method can be a good candidate. Notably, using vapor-liquid-solid(VLS) CVD method, high quality single crystal wires can be grown on selected area. Considering most of silicon photocell cost attributes to single crystal wafer production, this VLS-CVD can be a cost-effective option.

Therefore, following two sections will cover these two fabrication methods. Section 3.3.1 will describe the processes for wafer-scale vertical wires fabrication using wet chemical etching. This array will be exclusively used in this research as the photoanode substrate. The next section, 3.3.2 is about VLS-CVD wires fabrication. It is a separated project from photoanode fabrication, but the experimental procedures will give a good intuition about CVD processes. Additionally, fabrication methods for highly complex nanowire structures will be presented. In fact, complex 3-D structures could be beneficial to photoanode since it increases light scattering as well as surface area. It is expected that the methods provided here may contribute to the future photodevices directly or indirectly.

3.3.1 Bulk array by wet etching

3.3.1.1 Metal assisted silicon etching

Metal assisted silicon etching is an electroless chemical reaction. When metal catalyst is making intimate contact with silicon in electrolyte containing hydrogen peroxide(H_2O_2) and HF, cathode and anode are locally formed and following chemical reactions occur:[86]

Cathode reaction(at metal):

$H_2O_2 + 2H^+ \rightarrow 2H_2O + 2h^+$
$2H^+ + 2e^- \rightarrow H_2 \uparrow$

Anode reaction:

$Si + 4h^+ + 4HF \rightarrow SiF_4 + 4H^+$
$SiF_4 + 2HF \rightarrow H_2SiF_6$

Overall reaction:

$Si + H_2O_2 + 6HF \rightarrow 2H_2O + H_2SiF_6 + H_2 \uparrow$
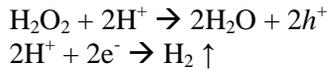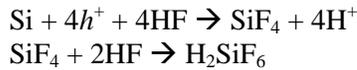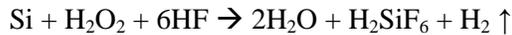
Equation 3.1 Metal assisted chemical etching

As a result, the silicon area covered by metal catalyst is selectively etched. Commonly, such metals as gold, platinum and silver work well in this reaction.

Using this method, many researches on patterned silicon wires arrays have been reported.[87-89] Conceptually, patterned metallic film is prepared on silicon substrate by random metal deposition, nanosphere lithograph or photolithography. When this substrate is subjected to H_2O_2/HF solution, the pattern is transferred to the silicon substrate. By adjusting elapsed etching time, the etching depth can be controlled.[41, 90] This method is simple and scalable, and does not require complex facilities.

In this research, the metal film will be patterned with optical photolithography since it is more reproducible in micrometer sized range than others.

3.3.1.2 Fabrication processes

3.3.1.2.1 Patterning

First, silicon wafer was cleaned by acetone, IPA and 1:10 HF:DIW before photolithography. This wafer was dried for 10 minutes at 200 ℃ on hotplate. Shipley S1805 positive resist was spin-coated at

500 rpm for 5 seconds followed by 5000 rpm for 35 seconds. Prebake was conducted for 1 minute on 115 ℃ hotplate. Typically, S1805 follows hexamethyldisilazane(HMDS) monolayer coating for good adhesion. However, it was sometimes observed that HMDS still remains even after development. This is problematic because there should be no barrier between silicon and metal catalyst. To prevent this possibility, no HMDS was used in this process. This greatly reduced the adhesion between photoresist and silicon substrate. Therefore, a careful handling was given to further processes, especially wet processes.

Chrome mask has regular 1 μm diameter circular dots pattern with 2 μm center-to-center spacing. The photoresist was exposed using mask aligner(MA-4 with 365 nm i-line lamp, Karl Suss) for 5 seconds, which is about 50 mJ/cm^2 dose. For good contact, vacuum contact mode was selected. This exposed resist was then developed by MF-321(Rohm and Haas) for 1 minute with gentle agitation.
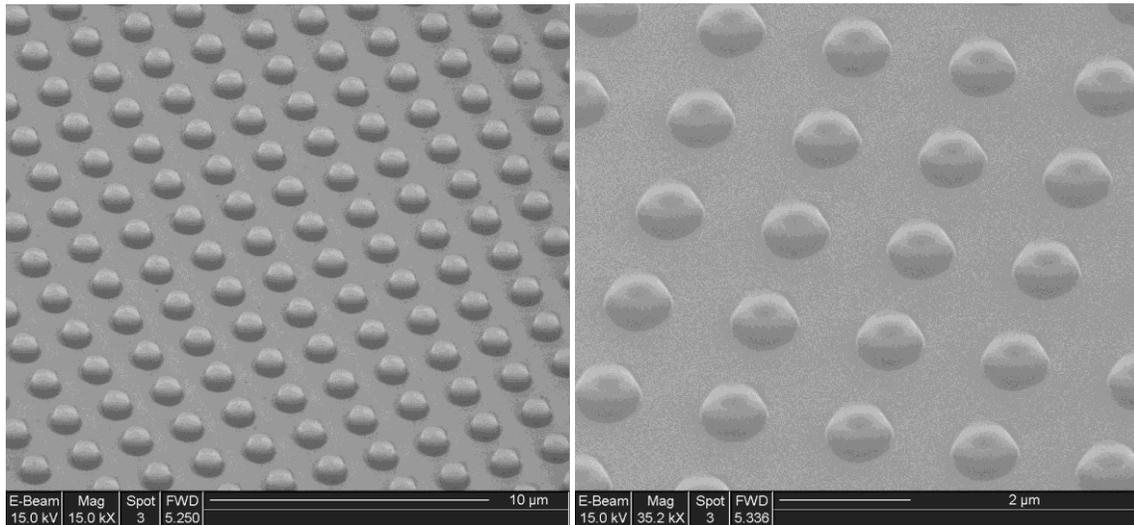
Figure 3.5 Photolithography pattern

Figure 3.5 shows final patterns. The pattern integrity primarily depended on contact quality between mask and substrate, and uniformity of incident light. Although special care was paid to the handling, imperfect contact still happened due to dust particles and non-uniform photoresist layer(mainly air bubbles during spin coating). The patterns were islands in bright mask. Therefore, when contact was not good, light diffraction unintentionally exposed the center of patterns, resulting in volcanic shape. However, these are not fundamental problems of photolithography. It is believed that better process control eliminates this pattern non-uniformity issue.

After development, oxygen plasma was used for descum, 100 W for 30 seconds. 30 nm gold film was deposited by thermal evaporator and lifted-off in acetone with ultrasonic agitation, followed by IPA and DIW cleaning. Final film pattern is given in figure 3.6.
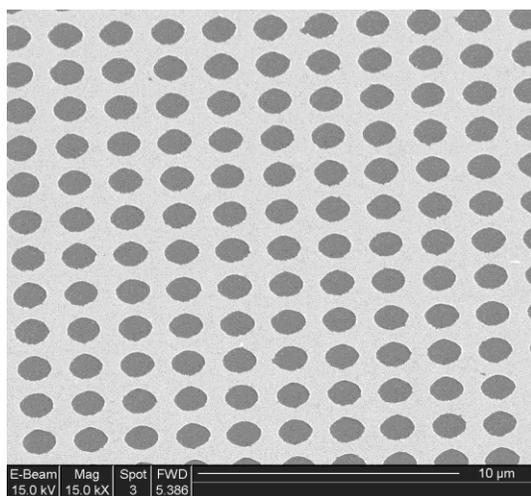
Figure 3.6 Lifted-off gold film

3.3.1.2.2   Wet etching

Etching reaction primarily occurs at the interface between metal catalyst and silicon. However, bare silicon is also etched at very slow rate. In case of untreated silicon, this is not a problem, since silicon wafer has uniform electric characteristic throughout the volume. On the contrary, n^+ back doped wafer has very shallow doping layer(on the order of 10~100 nm). Thus, this layer must be protected before wet etching, so a masking tape was affixed to the back side of wafer.

The patterned wafer with back side protection was immersed in etching solution containing 4.6 M HF and 0.4 M H_2O_2. Typical 1 liter solution consists of 163 ml HF(49 % wt.), 40.8 ml H_2O_2(30 % wt., J.T. Baker) and DIW for the remainder. In this etching condition, 30 minutes etching produces about 10 μm high silicon wires array. When silver was used in a substitution for gold, etching was generally faster. However, silver film frequently formed voids, so it was hard to maintain pattern integrity. Therefore, gold was exclusively used for etching catalyst.

After silicon etching and cleaning in DIW, gold film was removed by gold etchant(TFA, Transene) for 5 minutes and rinsed in DIW. Since evaporated gold film tends to have grain-like non-uniform shape, there were narrow spines between wires. To remove these unwanted spines as well as contamination on the silicon wires surface, the silicon substrate was etched in 50 % wt. potassium hydroxide(KOH, Sigma-

Aldrich) solution at 40 ℃ for 15 seconds. During KOH etching, silicon back side was protected by masking tape. Figure 3.7 shows the completed wires array.
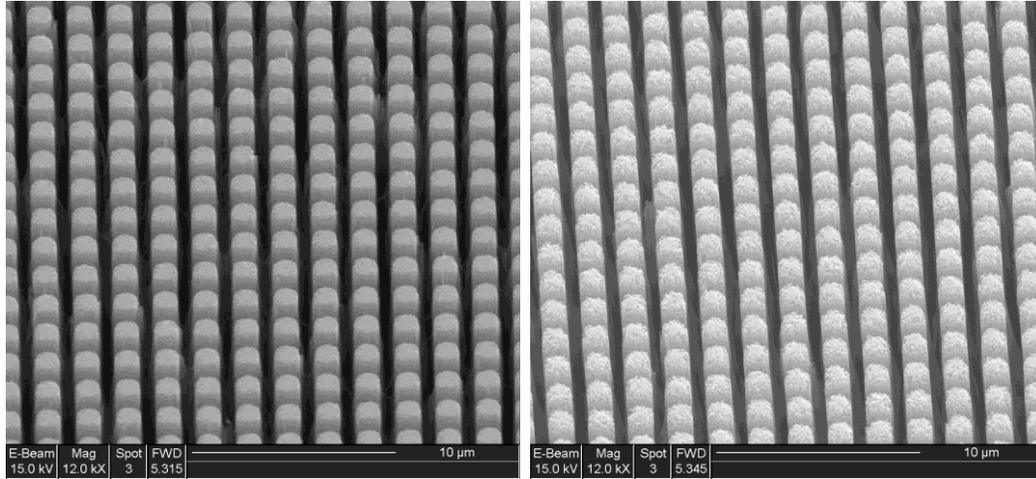
Figure 3.7 Silicon wires array after gold etching(left) and KOH etching(right)

3.3.2 Selective growth by chemical vapor deposition

CVD nanowire growth is a good alternative for nanostructure fabrication. The single crystal nature of CVD grown semiconductors provides a cost-effective measure for high quality semiconductor platform not only for solar devices[91, 92] but various electronic components.[93, 94] In this section, bulk nanowire growth mechanism and procedure will be presented first. This produces large area nanowires array which is analogous to the array fabricated by wet etching in section 3.3.1. In addition, CVD allows very selective growth. Therefore, in combination with secondary manipulation techniques, complex structure fabrication methods will be introduced. The contents here could also be found in references.[95, 96]

3.3.2.1 Overview of CVD nanowire growth

3.3.2.1.1 Mechanism

There are a couple suggested mechanisms for CVD nanowire growth, however, with the focus of silicon, it is mostly explained by vapor-liquid-solid(VLS) growth mechanism. Figure 3.8[97] describes VLS scheme.

51
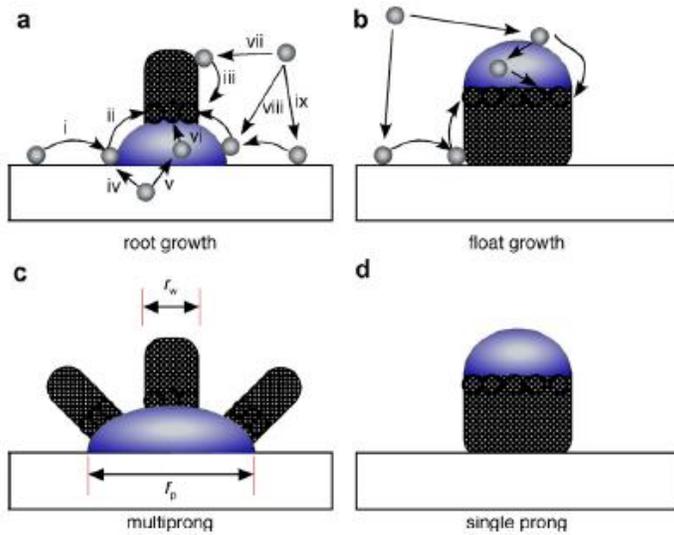
Figure 3.8 VLS nanowire growth mechanism.

VLS nanowire growth requires solid surface, catalyst and volatile chemical vapors. In high temperature environment, the chemical vapors are decomposed on the solid surface, then the atomic element is dissolved into the catalyst. The catalyst under eutectic alloy state is soon super-saturated by the extrinsic element, therefore precipitates it as a form of crystalline solid. Once nucleation is initiated, that becomes thermodynamically favorable point. Subsequently, further precipitation proceeds in the same direction, making one dimensional(1D) wire shape.

For optimal VLS growth of nanowires, certain conditions must be satisfied. Since catalyst must be stable liquid state throughout the growth process for continuous growth, it is ideal that there are not many solid alloy states consist of catalyst and wire material. Otherwise, unintended precipitation or catalyst poisoning could happen. Figure 3.9[98] shows the case of silicon and gold.
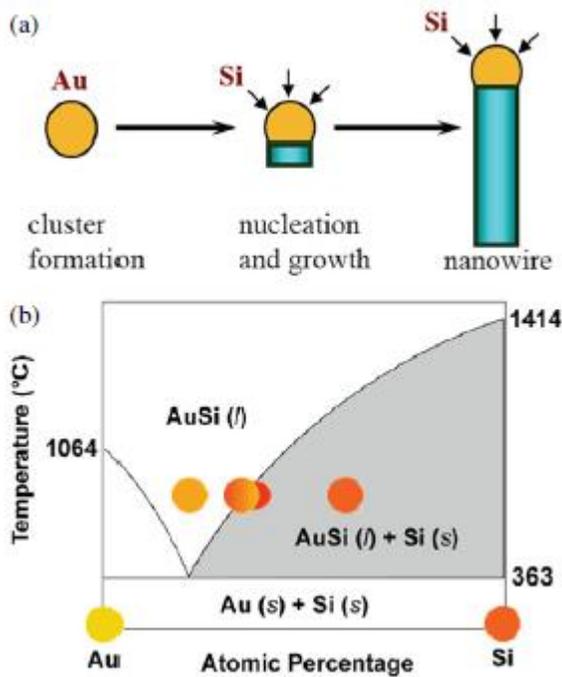
Figure 3.9 Phase diagram of gold and silicon alloy, and silicon nanowire growth process with gold catalyst.

Silicon forms simple eutectic alloys with many metals, which makes it a popular choice for CVD nanowire. Among those catalysts, gold is preferred due to its very low eutectic temperature, about 363 ℃. Low temperature is desirable because it prevents homogeneous decomposition of volatile chemical vapors causing unintended deposition or nucleation. This improves the selectivity, resulting in nanowire growth exclusively on catalyst sites.

The control of morphology is mainly conducted by catalyst and substrate. Since the catalyst size determines the nanowire diameter as shown in figure 3.9, fine nanoparticles or nanopatterns are used for well controlled nanowire array. Alternatively, thin catalyst film which dewets on the substrate can be used for high density wires fabrication. Substrate determines the growth direction. There are energetically favorable crystalline faces depending on materials and the size regime. If a substrate has matching crystal structure, it leads to epitaxial growth. Figure 3.10[99-101] shows various nanowires grown epitaxially using nanoparticles.
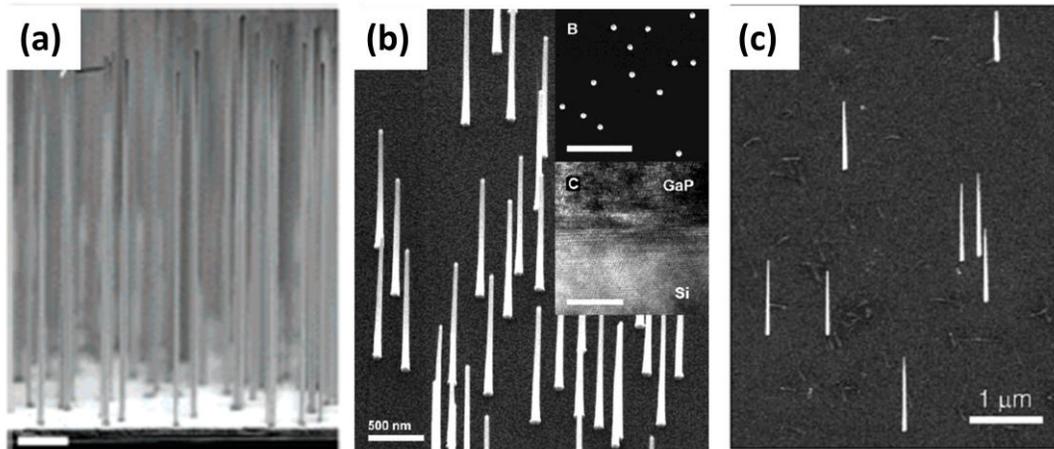
Figure 3.10 Epitaxial nanowire growth. (a) Si nanowires on Si(111) surface, (b) GaP nanowires on Si(111) surface and (c) GaAs nanowires on Ge(111) surface.

3.3.2.1.2 Complex system realization

Beyond photovoltaic applications, nanowires are also attracting a significant attention as a potential nanoscale building block for future nanoscale devices or structures. The scaling effect has already been proven in many nanoscale devices. However, if the structure can be extended from simple 1D shape to 3D configuration, it would be ultimately possible to fabricate complex circuitry analogous biological neural logic.[102] In this path, beam processes provide usable toolkits since they enable 3D manipulation with machining and deposition capabilities. Therefore, we demonstrated focused ion beam(FIB) based nanowire complex structures by two approaches.

First method is nanowire bending by FIB direct irradiation. Implanted ions induce stresses on the structure[103-106] followed by spontaneous bending. By changing the beam irradiation direction, complex structures could be successfully demonstrated. Also, it was also expected that FIB deposited material may induce stress on the structure. To demonstrate this hypothesis, FIB-CVD was used to deposit platinum on the nanowire, and bending behavior was observed.

Second method is cascade branching. Although branching has been demonstrated,[107-112] the branch points have been randomly defined, which hinders the deterministic structures fabrication. Therefore, we used FIB to exactly pattern the branch point. Ideally, if direct FIB gold deposition is possible, simple repetition of FIB catalyst deposition and nanowire growth can generate branched structures as illustrated in figure 3.11. Although gold FIB-CVD has been demonstrated,[113] the system is not commercially available. Therefore, we adopted indirect method. Pre-grown silicon nanowires array was oxidized to form thin protective oxide layer. Then, using FIB, branch points were defined by etching the oxide to

54

expose silicon underlayer. Gold particles could be selectively deposited on these exposed silicon points by galvanic displacement. These particles became the next catalytic points to grow secondary nanowires. By repetition, several generations of parent/child pair were demonstrated.
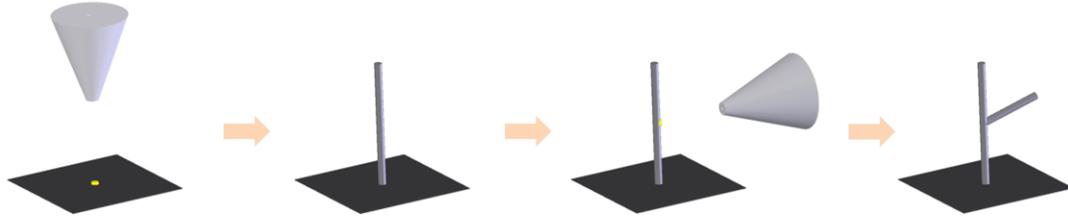
Figure 3.11 Ideal FIB branching method. FIB deposition of catalyst followed by nanowire growth.

3.3.2.2 Experiments

3.3.2.2.1 Nanopattern generation

Gold nanodot patterns were created by e-beam lithography and gold lift-off. It started with substrate preparation. Silicon wafer(4" n-type arsenic doping, (111) direction, resistivity 0.002~0.003 Ω-cm, thickness 500~550 μm, Wafernet) was diced into 1 cm by 1 cm pieces by diesaw. These silicon pieces served as the substrates. They were thoroughly cleaned by acetone, IPA and DIW with ultrasonic agitation.

After cleaning, the substrate was dried, typically on 180 ℃ hotplate for more than 1 minute. Then, poly(methyl methacrylate)(PMMA, 950 series, 3 % solid contents in chlorobenzene, Microchem) were spun at 4000 rpm for 45 seconds. This spin-coated substrate was baked at 180 ℃ for 90 seconds.

E-beam lithography was conducted by SEM(XL-30, FEI) equipped with nanopattern generation system(NPGS, Nabity). Patterns were drawn under the conditions of 30 kV acceleration voltage, 2000x magnification, spot 1 and 350 $\mu C/cm^2$ dose. After patterning, the resist was developed by IPA:MIBK=3:1 developer for 60 seconds, and rinsed by IPA. To remove residual organic contaminants, descum was performed by oxygen plasma cleaner for 10 seconds at 50 W. This substrate was loaded in metal evaporator, and 60 nm gold film was deposited. The gold film was later lifted-off by acetone.

3.3.2.2.2 Silicon nanowire growth by CVD

Silicon nanowires were grown by home-built atmospheric pressure CVD setup as described in figure 3.12.
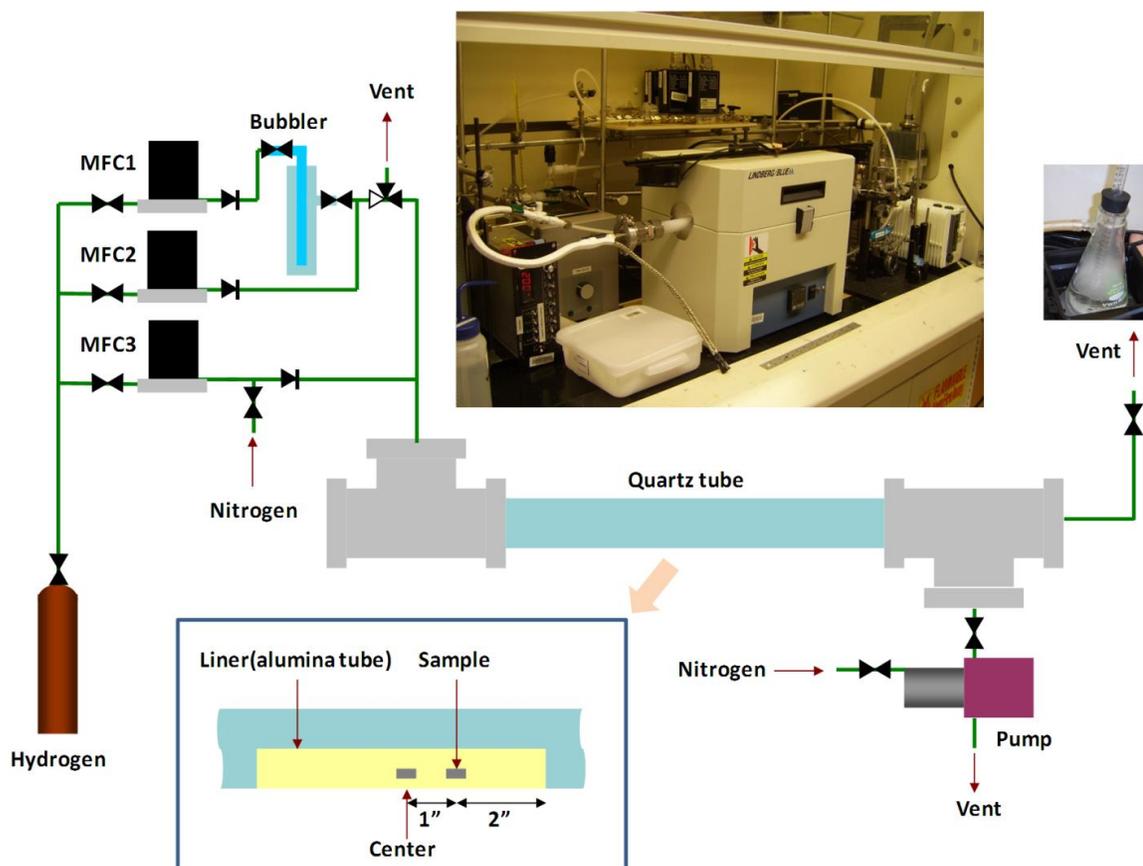
Figure 3.12 CVD nanowire growth setup. Upper picture captures the installation. Upper right is the picture of chlorine trap. Bottom inset shows the details of sample loading. Prepared substrates are placed inside the alumina tube, and this alumina tube is inserted to the quartz tube. Alumina tube center position is aligned with furnace center.

Silicon tetrachloride(SiCl$_4$, Sigma-Aldrich) was used as silicon precursor, and hydrogen(99.999 %) was used as carrier and dilution gas via MFCs. SiCl$_4$ was maintained to 5 ℃ in cold water bath, and all the tubing from bubbler to reactor was wrapped by heating band to prevent precipitation of the precursor. The bubbled precursor gas was fed into quartz tube(60 cm length and 1" O.D.) placed in a tube furnace(Blue M, Lindberg). Venting port at the end of the quartz tube was connected to a glass flask filled with calcium carbonate(CaCO$_3$, Sigma-Aldrich) solution to trap exhaust chlorine gas. Separately, a vacuum pump was installed to quench the reaction quickly. When pump is operating, valves connected to bubbler and trap were closed.

One dummy and one sample substrates were placed in the liner(alumina tube, 6" length, 0.75" O.D. and 0.5" I.D). The dummy substrate was in the center of the liner(and eventually, in the center of the furnace) and sample substrate was 1" apart from dummy. This liner was inserted to the quartz tube, and the tube was sealed by clamp. Afterward, the quartz tube was evacuated by pumping, followed by hydrogen back-filling to atmospheric pressure. This process is to prevent oxidation during nanowire growth.

The furnace was heated to 890 ℃ with the rate of 50 ℃/minute while flowing 175 sccm hydrogen through MFC3 in figure 3.12. MFC1 and MFC2 were set to 50 sccm and 15 sccm, respectively, and stabilized before growth process. When the furnace temperature reached 890 ℃, all gases from MFC1~3 were fed into the quartz tube and maintained for about 1 minute. The nanowire growth rate was typically about 10 μm/minute. After the growth, the precursor supply was shut off, and the quartz tube was evacuated by pump for about 30 seconds to quickly quench the growth. This was followed by hydrogen back-filling through MFC3. When the pressure in the quartz tube reached to atmosphere(which takes about 2 minutes in our setup), the backside venting port was open and the furnace was cooled down to room temperature.

To maintain reliable CVD condition, which means repeatable epitaxial growth condition, quartz tube was regularly cleaned by KOH solution. Also, after every cycle, alumina tube was cleaned by KOH, so the environment nearby the sample was always consistent. Before the experimental cycle, at least one dummy cycle was run to stabilize all the setup. Figure 3.13 shows the epitaxially grown nanowires(toward (111) direction) prepared from catalysts array in section 3.3.2.2.1.
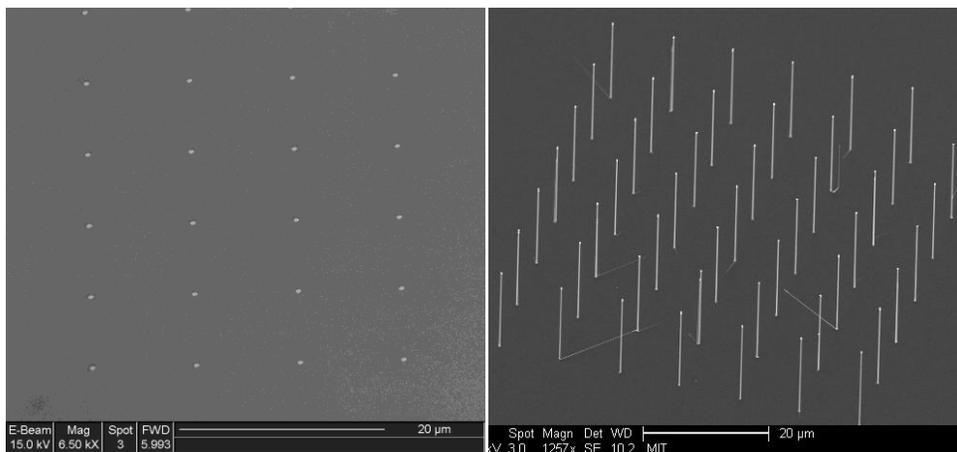
Figure 3.13 (left) Patterned catalyst array and (right) nanowires grown from catalysts array.

3.3.2.2.3 Shape manipulation

Shape manipulation was conducted using FIB(dual beam machine, DB-235, FEI) patterning function with 30 kV acceleration voltage, 10 pA aperture, 1 μs dwell time and 50 % overlap conditions. These conditions were applied to all the ion beam irradiation experiments except platinum deposition whose conditions were 30 kV acceleration voltage, 10 pA aperture, 0.4 μs dwell time and 0 % overlap.

3.3.2.2.3.1 Direct FIB bending

Bending by high dose gallium implantation was conducted by drawing small ion beam pattern on the nanowire sidewall. Unless specified, the default incident angle was 90 °, meaning the beam was perpendicular to the nanowire. The ion beam pattern was single pixel width line of 0.5 μm length. This line length was determined to be slightly longer than the nanowire diameter, to prevent any misalignment issue coming from the beam drift. The beam dose was altered by changing overall process time.

Low dose gallium implantation was conducted by raster scanning of the ion beam in large area. With 15000X magnification, the ion beam was irradiated for 30 seconds with 66.8 ° of incident angle.

For platinum induced bending, gas injection system(GIS) containing methylcyclopentadienyl trimethyl platinum($(CH_3)_3(CH_3C_5H_4)Pt$) was activated during ion beam patterning. Platinum patterns of 0.4 μm by 0.2 μm rectangle were drawn on the side of the nanowires with the beam incidence angle of 66.8 ° for 20 seconds. After platinum deposition on the wires, the substrate was annealed at 800~900 ℃ for 30 minutes in argon atmosphere.

3.3.2.2.3.2 Consecutive branching

The nanowires array were cleaned by 1:10 HF:DIW solution for 2 minutes, TFA gold etchant for 2 minutes and again HF solution for 10 seconds to remove the gold catalyst used for primary nanowire growth. Then, this substrate was oxidized in our tube furnace at 900 ℃ for 5 minutes with 200 sccm oxygen flow. This formed 2~3 nm thin oxide film all over the substrate. This oxidized substrate was loaded in FIB chamber and square patterns, typically 0.2~0.3 μm size, were drawn on the sidewall of the nanowires with 5.6 mC/cm^2 dose. Through this etching was exposed underlying silicon. Galvanic displacement was conducted in 0.01 M of potassium gold(III) chloride($KAuCl_4$, Sigma-Aldrich) solution. This solution was dropped on the patterned substrate by pipet and maintained for 1 minute. The substrate was then cleaned by IPA and quickly dried on a hot plate at 200 ℃. This process created gold nanoclusters selectively on the exposed silicon while the oxide layer served as a mask. IPA was used for

cleaning, if possible, instead of DIW because it has lower surface tension so decreases the chance of accidental breakage of the nanowires or detachment of gold nanoclusters. This treated substrate was subject to secondary nanowire growth, and the overall cycle was repeated for the next generation.

For nanotube fabrication, the branched nanowires were oxidized for 60 minutes at 900 ℃ in oxygen environment to form a thick oxide on the nanowires surface, making silicon-silicon dioxide core-shell structure. After oxidation, small holes (0.1 μm by 0.1 μm square) were patterned near the tip of nanowire branches to expose silicon core. Then, this substrate was placed in xenon difluoride(XeF_2) isotropic silicon etcher(ES-2000XM, SE Tech), and etched for 60 seconds and 3 cycles(total 180 seconds).

3.3.2.3 Fabricated structures

3.3.2.3.1 Direct FIB bending

Figure 3.14 shows the scheme and high magnification transmission electron microscope(TEM, JEM-2010F, JEOL) images as well as energy dispersive X-ray spectroscopy(EDS) results.
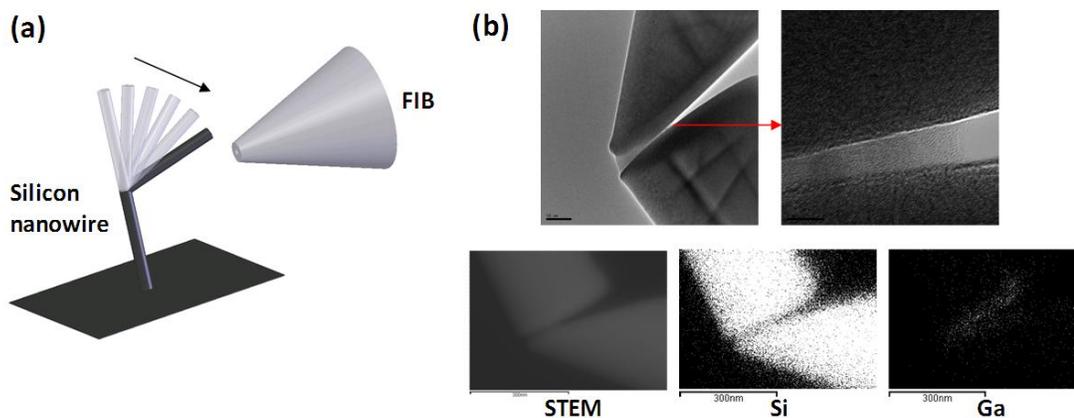
Figure 3.14 (a) Direct FIB bending scheme, and (b) TEM images and EDS results showing silicon and gallium distribution.

Along with deep cut shape, large distribution of amorphous silicon and implanted gallium is observed. It is believed that the amorphous silicon, which derives from mechanical impact and redeposition, experiences crystallization by large amount heat generated during implantation. This crystallization induces tensile stress,[114] and the nanowire is subject to bending force toward beam irradiation direction. And, by changing the line dose, the bending angle can be as large as beam incidence angle(figure 3.15).
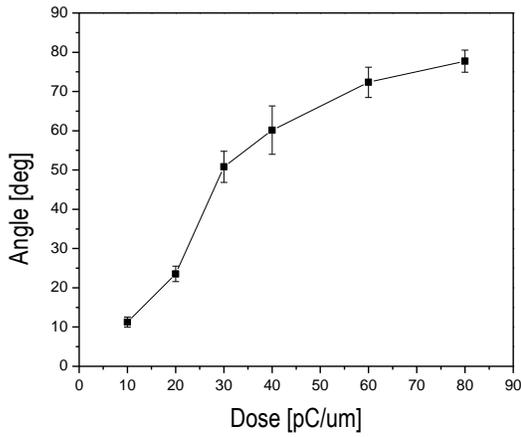
Figure 3.15 Bending angle vs. beam dose plot.

Since both bending angle(by dose) and direction(by beam irradiation direction) can be controlled, very complex bending structures could be successfully fabricated as shown in figure 3.16.
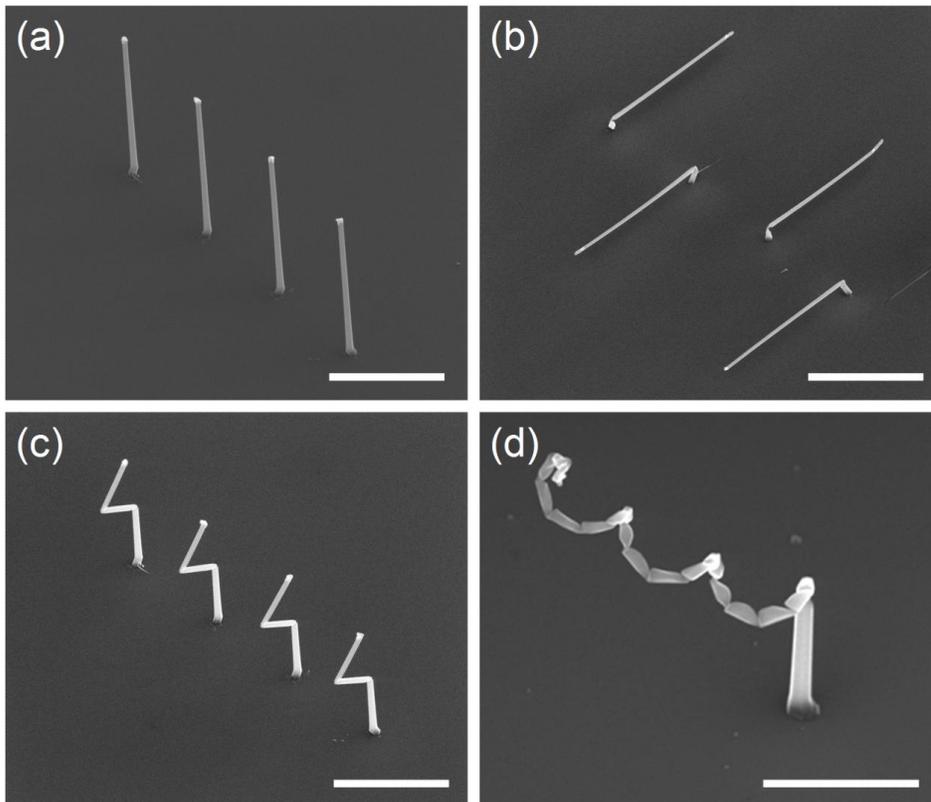
Figure 3.16 Nanowire bending SEM pictures. (a) Vertically grown silicon nanowires array. (b) Fully bent nanowires with ion beam irradiation on the nanowire bases. Ion beam was irradiated from the top-right direction on (from the

left) the first and third nanowires, and from the bottom-left direction on the second and fourth nanowires. (c) Hook shaped nanowires. First irradiation from top-right direction, followed by second irradiation from bottomleft direction. (d) Spring shaped nanowire. 45° inclined line pattern was repeated several times on side view of nanowire. Scale bars: (a)-(c) 5 μm and (d) 2 μm.

If the tensile stress induces bending in the beam incident direction, compressive stress may lead to bending away from the beam direction. In this standpoint, we devised methods to change the stress mode to compressive stress. One possible way is to implant interstitial gallium in the silicon matrix with a minimal damage as possible. It is known that implanted gallium ion distribution can be expressed as a combination of error functions, in which the peak locates near the incident surface.[115] However, since focused patterning makes a deep damage due to the local high dose, we conducted low dose raster scanning in large area. Figure 3.17 shows (a) before and (b) after the raster scans that resulted in bending away from the beam incident direction. This means that there would be a threshold dose in which the tensile stress beats the compressive stress, consequently the bending direction reverses.
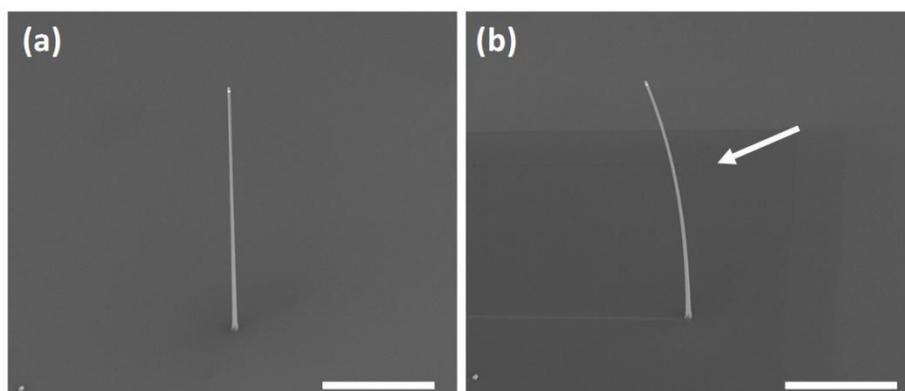
Figure 3.17 Low dose ion implantation (a) before and (b) after irradiation. Beam incidence from right side as indicated by arrow in (b). Scale bars: 5 μm.

Although dose control can select the bending direction, low-dose requirement for the compressive stress limits the bending angle, allowing only small angle. Therefore, it is desirable to find an alternative way to induce a strong compressive stress without making significant damage to the nanowire. In this respect, it is notable that some of metallic silicides formed on silicon exert a compressive stress.[116] Figure 3.18 shows the silicon nanowires after platinum deposition and annealing. Bending occurs away from platinum deposition face due to the compressive stress occurred by platinum silicide. Because many bending points can be defined before the nanowire really bends, this "programmable" bending will be able to generate more complex structure, which is prohibited in high-dose implantation bending by

geometric restrictions. Figure 3.18 depicts various bending shapes with different platinum deposition points.
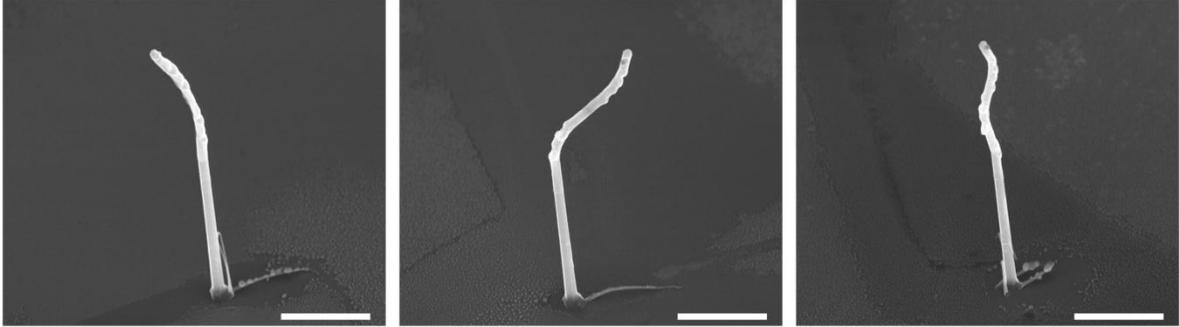
Figure 3.18 Platinum silicide bending. Scale bars: 2 μm.

3.3.2.3.2 Consecutive branching

Galvanic displacement is an electroless plating method using two redox couples with large redox potential difference.[117-120] If the ionic species in solution has more positive redox potential compared to silicon, that ion displaces silicon and is reduced. Since the reaction is species-specific, very localized gold deposition is possible in wide range of pattern sizes as shown in figure 3.19.
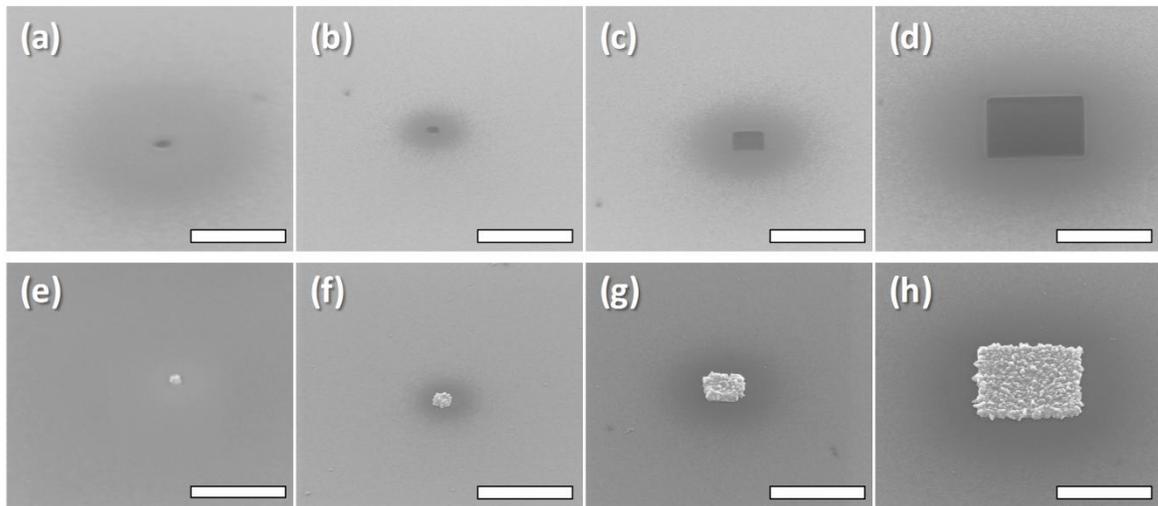
Figure 3.19 Galvanic displacement demonstration on flat silicon surface with oxide mask. (a)-(d) FIB patterned substrate, (e)-(h) after galvanic displacement, showing selective gold cluster deposition. Scale bars: (a)(e) 500 nm, (b)-(d)(f)-(h) 1 μm.

The fabrication processes are described in figure 3.20. On the oxidized wire, small hole was made by FIB, and this substrate was subject to galvanic displacement solution to deposit gold catalyst on the defined spot. From this catalyst, secondary wire was grown.
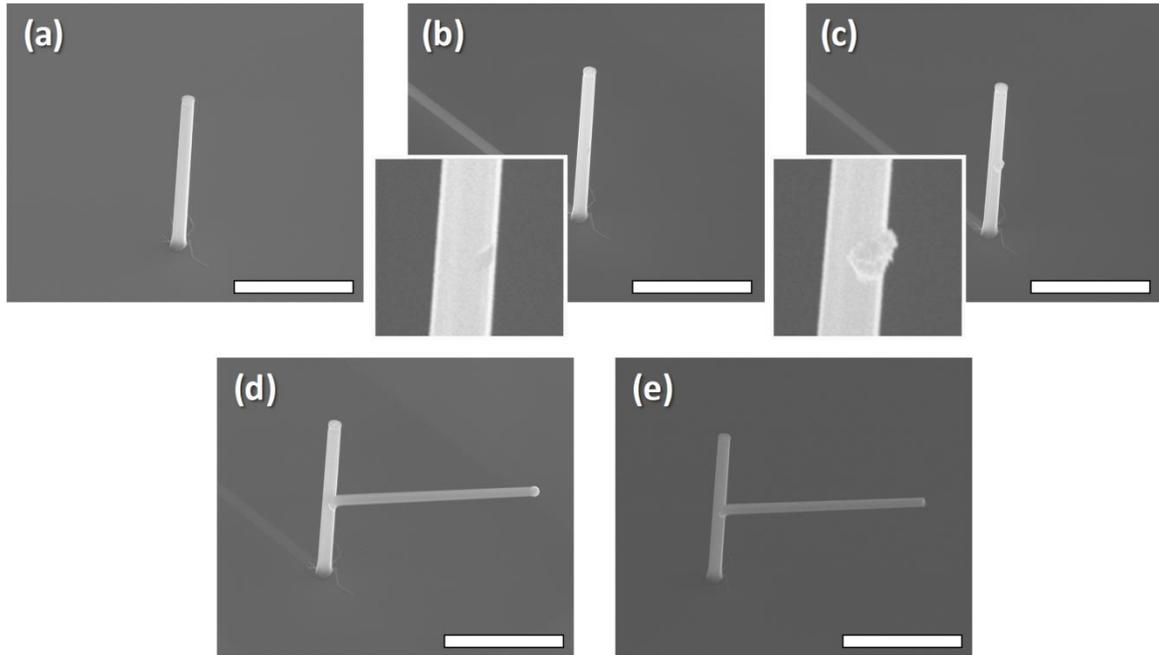
Figure 3.20 Branching procedure, (a) oxidized wires, (b) small hole made by FIB, (c) gold deposition by galvanic displacement, (d) secondary wire growth and (e) gold and oxide etching. Scale bars: 5 μm.

Figure 3.21 shows various shapes by combining or repeating the branching technique. Notably, repeated cycles allow multiple parent/child pairs of nanowire branches as shown in figure 3.21(c). Furthermore, figure 3.21(d) demonstrates that 3D interconnection like neural network is also possible by ingenious design of the processes.
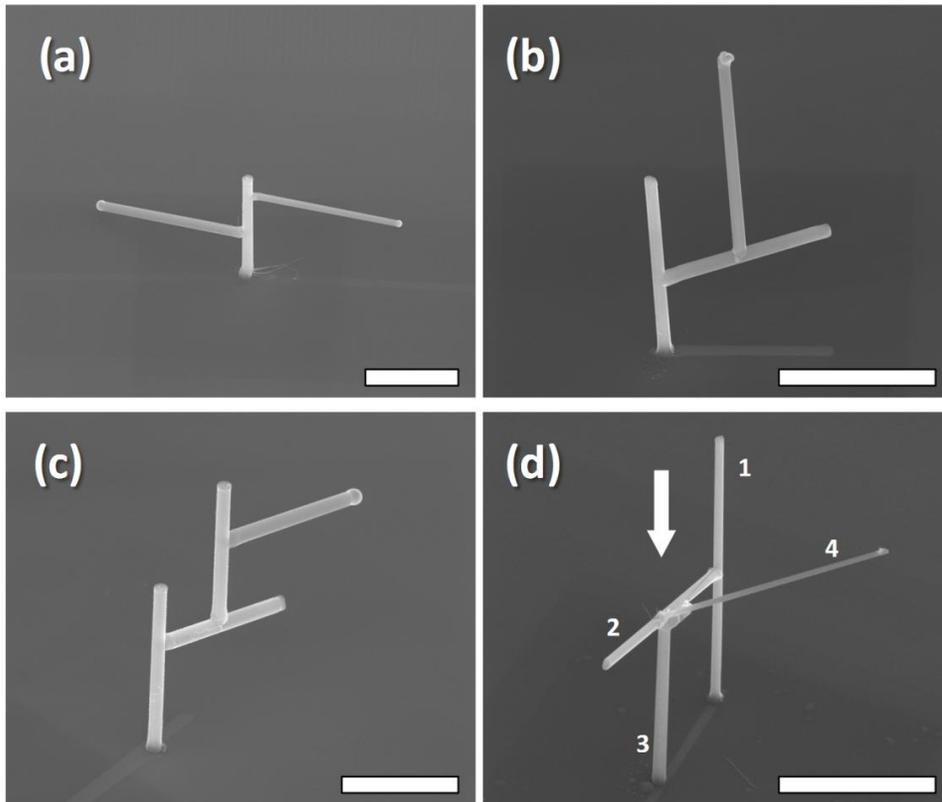
Figure 3.21 Complex branch structures. (a) Multiple branches from single core, (b) three generations and (c) four generations of child branches. (d) Interconnected branch structure. 1 and 2 branches growth followed by FIB etching of seed points on 2 and bottom. 3 and 4 branches growth afterward. Scale bars: 5 μm.

This nanowire branching method was further extended to branched nanotube fabrication in the similar manner as reported before[121]. Global oxidation created an oxide shell, while the inner silicon core was connected throughout the branched structure. After making a small hole on the oxide shell to expose the silicon core(figure 3.22(a) and (b)), selective isotropic silicon etching was conducted to remove this core(figure 3.22(c) and (d)). Etching gas penetrated through the silicon core up to the substrate. In figure 3.22(c), dark circular mark on the base shows etched silicon substrate, which makes it a free-standing nanotube on a silica membrane. To see the hollow inside, each end of the backbone and branch were cut by FIB as shown in figure 3.22(e) and (f). Since the shell thickness can be readily controlled by oxidation time and temperature,[122] it would be possible to synthesize branched nanochannel with predetermined diameter. Also, encapsulated hollow nanostructure may be fabricated by filling the etch hole with FIB-CVD or ion-beam sculpting.[123]
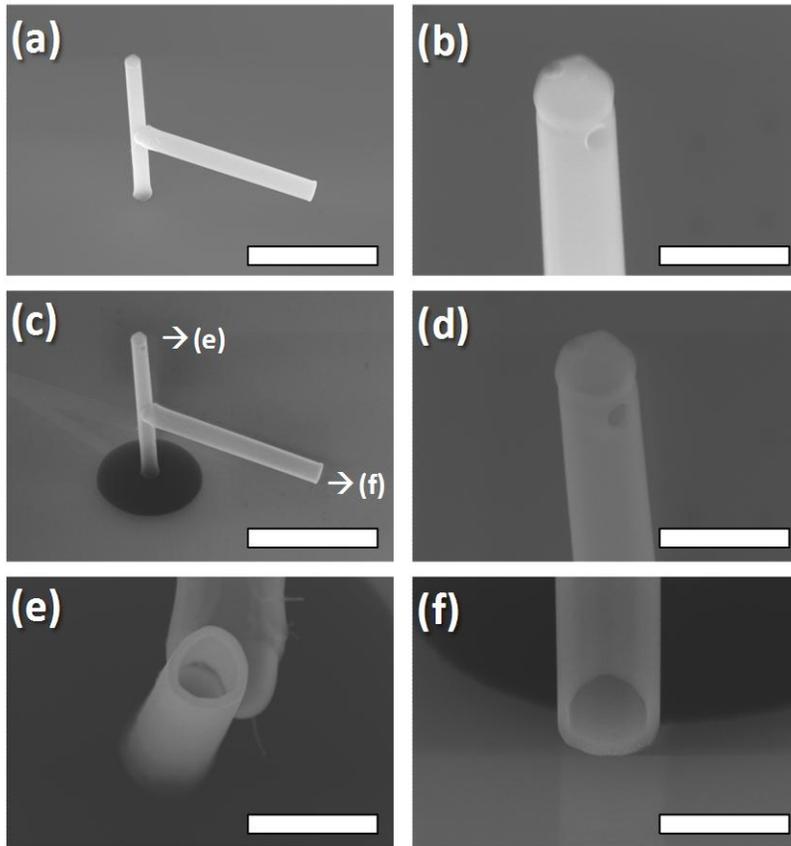
Figure 3.22 Branched nanotube fabrication, (a) branched nanowire with thick oxide, (b) magnified view of (a) near the backbone tip showing FIB etched hole, (c) after XeF$_2$ etching, (d) magnified view of (c) near the tip, (e)(f) magnified views of (c) after FIB cutting. Scale bars: (a)(c) 5 μm, (b)(d)(e)(f) 1 μm.

As in the case of epitaxial nanowire growth from crystalline substrate, the nanowires grown from parental nanowire also follows the crystal direction. Figure 3.23 illustrates three branches nanowires structure and selected area electron diffraction(SAED) images taken by TEM(JEM-200CX, JEOL) for each branch. All three branches have identical crystal structure and growth toward (111) direction.
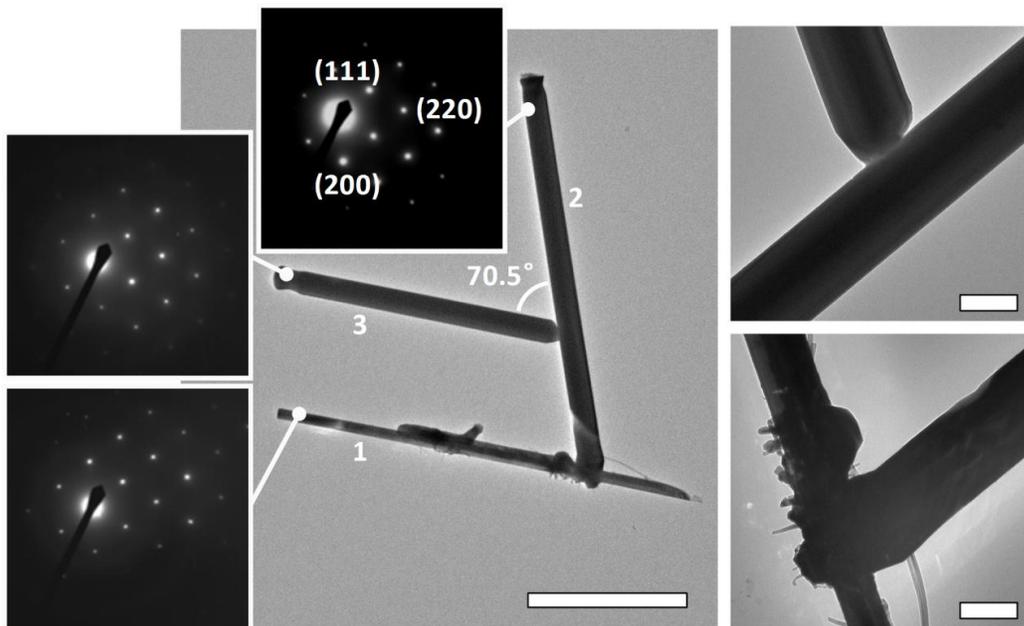
Figure 3.23 TEM image of three branches structure. (Left insets, SAED patterns on each branch; right insets, magnified junction images). Scale bars: 5 μm for main image, 500 nm for right insets.

This epitaxial growth nature enables rational complexity by selecting appropriate crystalline direction. In summary, without being compromised by randomness, our process demonstrated deterministic 3D complex structure concept with the combination of CVD nanowire and beam manipulation.

Chapter 4   Results and discussion

4.1 Iron-oxide film characterization

4.1.1 Morphology

Figure 4.1 shows SEM images of iron-oxide film, under the deposition condition of 10 sccm argon for iron precursor, 250 sccm oxygen for titanium precursor and 350 sccm oxygen for dilution. Deposition was conducted at 250 ℃ for 10 minutes(figure 4.1(a)) and 150 minutes(figure 4.1(b) and (c)), respectively.
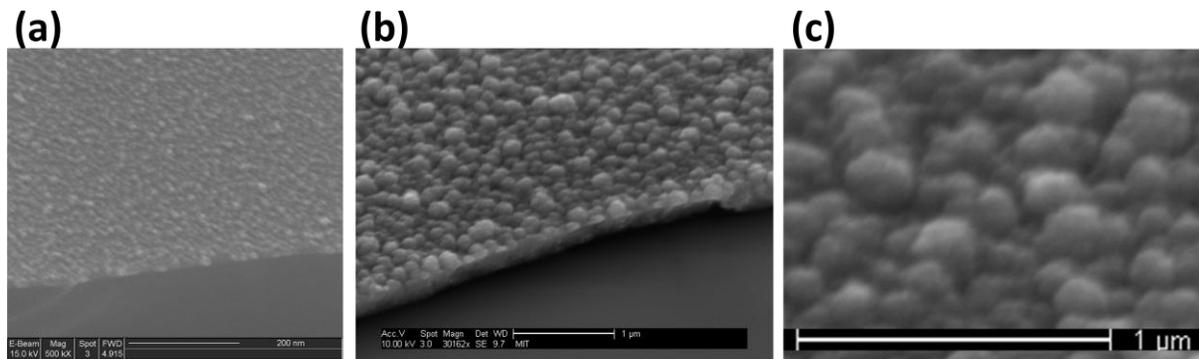
Figure 4.1 SEM image of deposited iron oxide film. (a) 10 minutes deposited film, (b) 150 minutes deposited film and (c) magnified view of (b).

Nominal thicknesses of the films are about 20 nm and 300 nm. Therefore, the deposition rate does not change during the deposition time window, which is about 2 nm/minute.

Iron oxide is generally known to be in polycrystalline phase. In figure 4.1(a), individual grain size ranges from 5 to 20 nm. Seemingly, thicker film has much larger grains, ranging 100 to 200 nm. When these grains are magnified, smaller grains-these will be called primary grains from now on- can be observed but very hard to clearly distinguish each other since most of them are smoothly connected like coalesced particles.
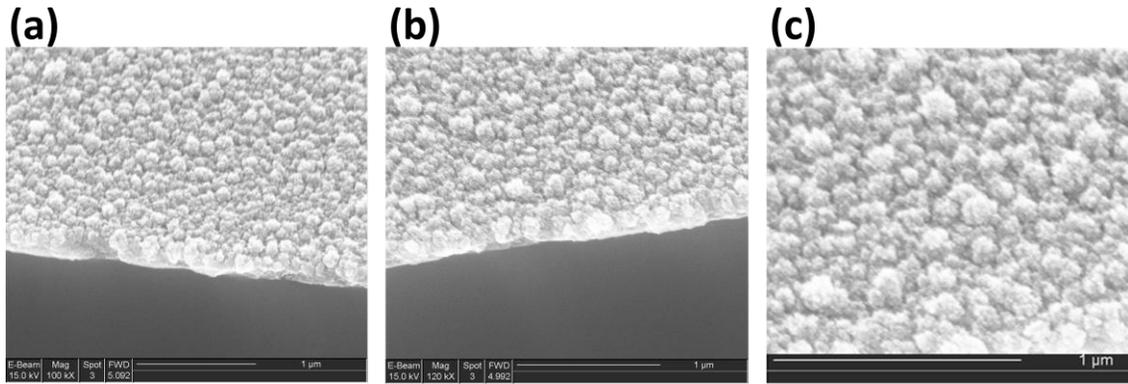
Figure 4.2 SEM images of titanium isopropoxide (a) 100 sccm and (b)200 sccm at 270 C, (c) magnified view of (b).

By changing temperature, the grain shape changes. Figure 4.2 shows films grown at similar gas flow but higher temperature(270 ℃) than figure 4.1. The measured growth rate was about 8~9 nm/min. At this higher deposition rate, the primary grains are more clearly observed as in figure 4.2(c), and this contributes to the sharp edges of the grains. From this observation, it is believed that, although high temperature is favorable condition for coalescence, deposition rate increases more rapidly than coalescence rate. This also implies that the iron-oxide deposition lies in reaction limited regime at this condition.
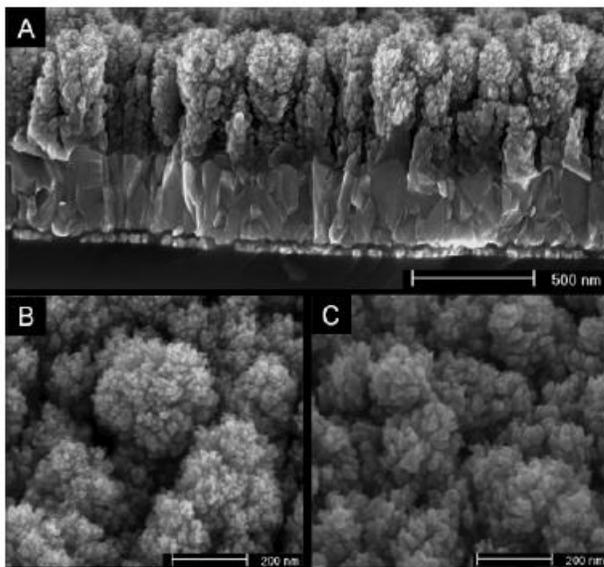
Figure 4.3 Dendrite structure deposited at higher temperature(about 415 ℃) at 100 nm/min rate.

Research conducted by Grätzel and coworkers[51] reveals the case of even higher temperature deposition. Using the same iron-oxide precursor, dendrite structure is observed in figure 4.3 under the conditions of 415 ℃ and 100 nm/min rate, which is consistent with our trend.

In the same research, the authors explains the advantage of this dendrite is shortened hole diffusion path, in similar manner to nanowires. Therefore, our coalesced grains grown at low temperature are not favorable structure. However, our film thickness is very thin, typically less than 20 nm. In this case, the film thickness itself is comparable or even thinner than iron-oxide hole diffusion length. Consequently, the coalesced grains would not levy a meaningful handicap.

4.1.2　Chemical composition

XPS measurement was used to quantify elemental composition of the iron-oxide film, and to identify chemical bonding states. Figure 4.4(a) and (b) are elemental survey and Fe2p fine scan result from the native film surface, and figure 4.4(c) and (d) are those after 20 second argon etching. Iron-oxide film was deposited at the same conditions to figure 4.1, saying 10 sccm argon for iron pentacarbonyl, 250 sccn oxygen for titanium isopropoxyde and 350 sccm extra oxygen at 250 ℃ for 10 minutes. All signals were obtained from 400 μm spot.
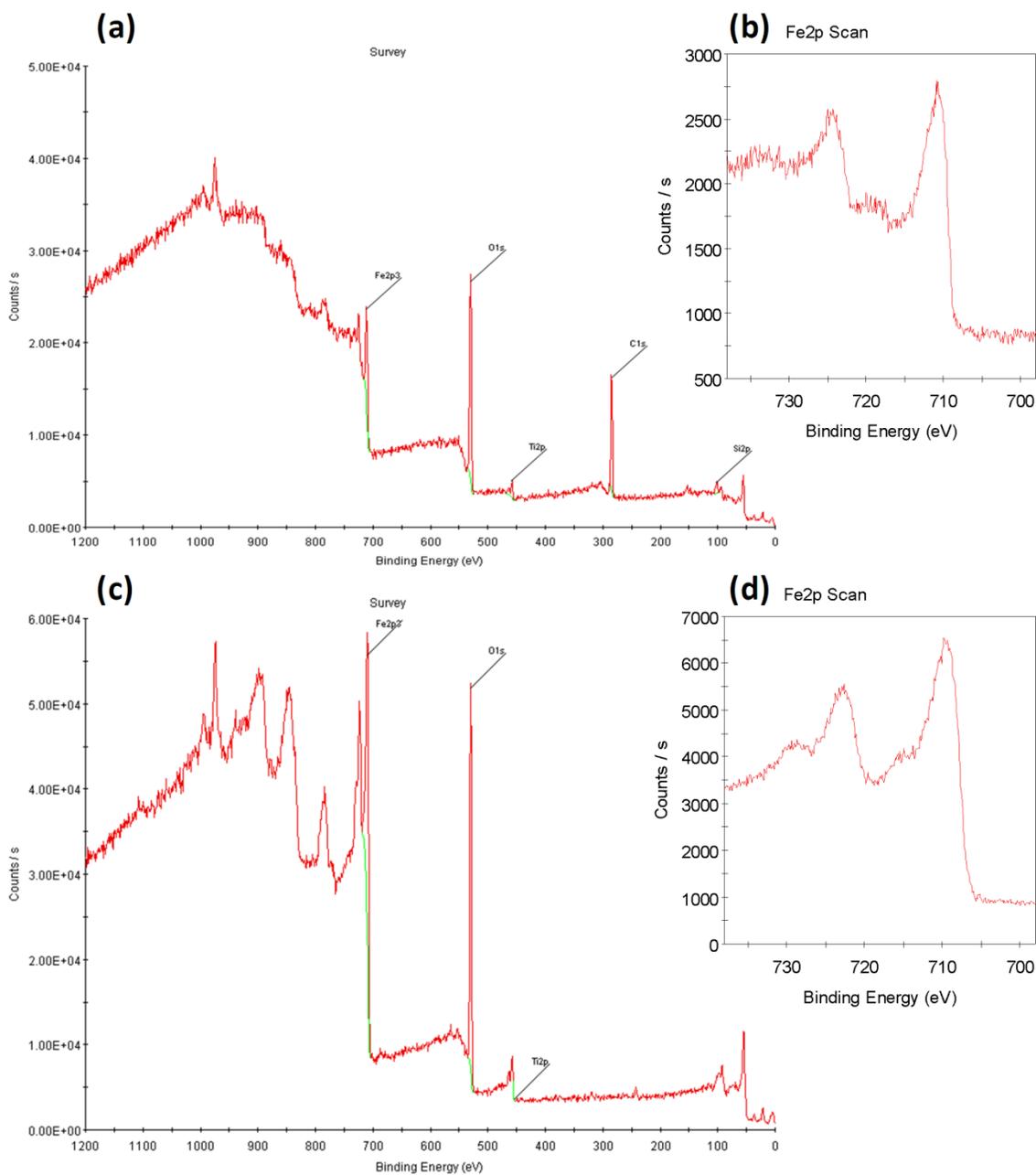
Figure 4.4 XPS results. (a) elemental survey and (b) Fe2p fine scan from native iron-oxide film, (c) elemental survey and (d) Fe2p fine scan from iron-oxide film after 20 second argon etching.

The measurement was conducted overseas, so the sample had been exposed to atmosphere for a long time during shipping. In the mean time, organic species may adsorb on the film, which possibly changes chemical composition of the surface since XPS signals are coming from the very surface, typically less than 5 nm collection depths. High contents of carbon in figure 4.4(a) are thought to derive from these

organic contaminants. Therefore, the surface was etched by argon for 20 seconds, and the subsequent carbon-free elemental composition(figure 4.4(c)) looks like this:

Name	At. %
C1s	2.49
Fe2p3	28.79
O1s	64.99
Ti2p	3.73

Table 4.1 Elemental composition of iron-oxide film

Notably, in this condition, iron shows atomic contents of 28.79 % and titanium 3.73 %. The relative ratio, about 13 % titanium with respect to iron, is very high value. If this dopant is well activated, iron-oxide, which is nondegenerate semiconductor, should have extremely high carrier density, turning it into degenerate regime. However, the resistivity turns out on the order of 10^5 Ω-cm. This means, although titanium contents are high, dopant activation is very limited. Further details will be discussed in iron-oxide electric property section 4.3.4.

This argon etching locally heats up the film, possibly changing the iron-oxide phase. Comparison between figure 4.4(b) and figure 4.4(d) clearly depicts the shift of Fe2p satellite peak. On that account, the signal from native iron-oxide film is thought to better represent the original iron-oxide phase.

Figure 4.5 is a comparison plot for iron oxidation states from reference.[124] By comparing figure 4.4(b) and figure 4.5, it is clear that our iron-oxide has Fe_2O_3 characteristic, showing satellite peak near 720 eV. Interestingly, figure 4.4(d), which describes the iron state after argon etching, reveals mixed signals of several phases. Overall, the peaks shift to lower energy, and at least two different signals overlap for each peak positions, with 728 and 723 eV for 2p 1/2, and 714 and 709 for 2p 3/2. It is hard to exactly identify the corresponding phases, but at least, it is clear that iron oxidation state is changed to lower oxidation value. This can be understood since annealing under vacuum or hydrogen environment is commonly used reduction method. Considering the analyzed elemental survey in table 4.1, it is thought that original iron-oxide film is in very oxygen-rich state. This may derive from oxygen environment during deposition process, or water adsorption from atmosphere.
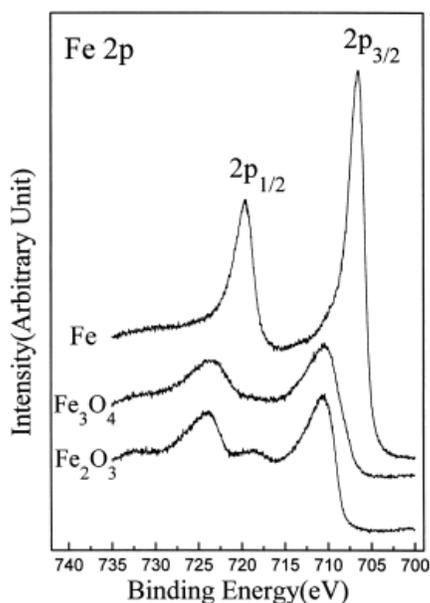
Figure 4.5 Fe2p XPS binding energy according to Fe chemical compositions

4.1.3 Crystallographic analysis

Crystallographic information was obtained from XRD measurement. Thin iron-oxide film resulted in too weak signal, which made it impossible to distinguish from background noise. Therefore, a thick film, 3 hours deposition or about 360 nm thickness, was prepared for XRD measurement.
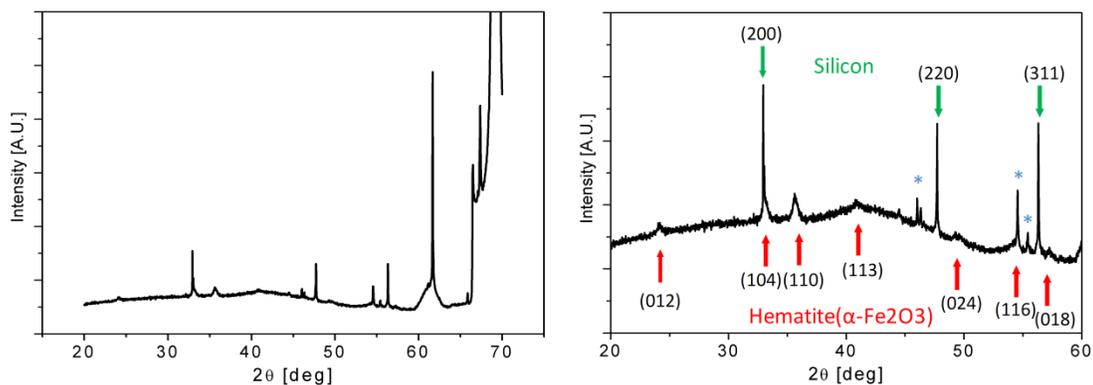
Figure 4.6 XRD measurement: (left) spectrum from 20 ° to 70 °, (right) magnified view from 20 ° to 60 °.

The sample was prepared on crystalline (100) silicon surface. Therefore, to minimize the strong silicon peaks(figure 4.6(a)), the information was trimmed to narrower window, from 20 ° to 60 ° as shown in figure 4.6(b). From references,[125-127] the iron-oxide peaks indicated as red arrows coincide with hematite(α-Fe_2O_3). This is of no surprise since hematite is known to be stable phase in atmospheric condition, and also our CVD condition is oxygen rich.

In the XRD plot, green arrows are silicon peaks. Although titanium contents are relatively high, no distinguishable peaks of titanium or its compounds are observed. Therefore, it is believed that titanium is uniformly dispersed instead of forming segregated domains. Additionally, there are a few unidentified peaks indicated as asterisks. These do not correspond to any of iron or titanium compounds. However, their very narrow full width half maximum(FWHM) implies that they may not come from iron or titanium oxide film since this film tends to have small polycrystalline microstructure as shown in SEM images. Therefore, it is very likely that these originate from silicon substrate.

4.2 Photocurrent measurement on plain silicon photoanode

In previous section, iron-oxide films were characterized under standard deposition conditions. In section 4.2, photoanode will be fabricated on plain silicon substrate, which experiences no special treatment except cleaning. Therefore, the intrinsic responses of silicon and iron-oxide photoanode as well as parametric studies on film or electrochemical variations will be presented.

4.2.1 Photocurrent by film thickness

The first step is to verify the photoresponse of bare silicon. Figure 4.7 shows dark and illuminated current of silicon without any iron-oxide deposition, showing no photoresponse of bare silicon. The sample had 10 minutes deposited iron-oxide film(~20 nm) and was measured at pH=13.8.
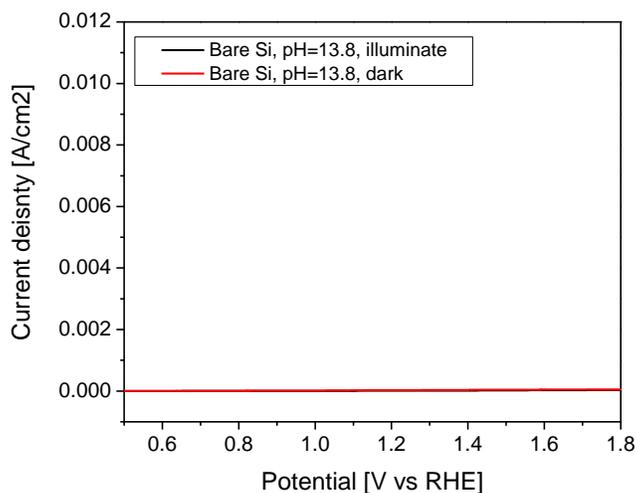
Figure 4.7 Bare silicon photoresponse, 20 nm iron-oxide film at pH=13.8.

Figure 4.8 depicts the photocurrent at pH=13.8 from silicon photoanode with thick(200 nm) iron-oxide film whose titanium precursor flow rate varied from 50 to 150 sccm.
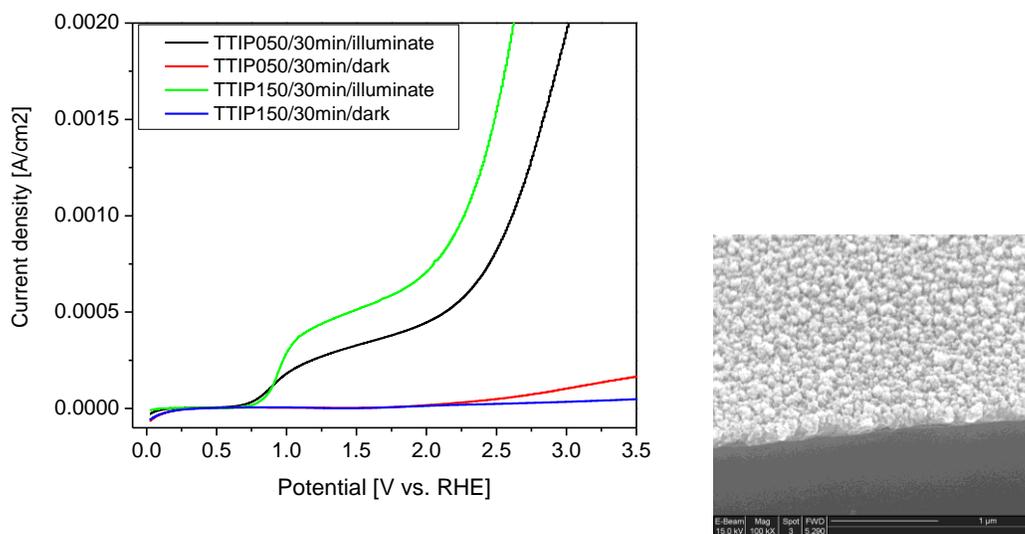
Figure 4.8 Photoresponses of thick iron-oxide films. Two samples with dopant flow rate of 50 sccm and 150 sccm, respectively. (right) SEM image of the thick film sample. 30 minutes deposition at 270 ℃.

The devices do show photoresponses with onset potential of 0.7~0.8 V vs. RHE. At zero overpotential(1.23 V vs. RHE), the current density reaches 0.2~0.4 mA/cm^2. When this result is compared

to previously reported iron-oxide photoresponse on metallic surface in figure 4.9,[51] similar pattern of current evolution is observed. That is, at a similar level of onset potential, current begins to increase with a large slope, followed by modest plateau in the potential range from 0.8~2.0 V vs. RHE. Therefore, it is assumed that the photocurrents observed in these samples attribute to photocarriers generated mostly in iron-oxide films. However, the current density is much lower than figure 4.9.

Actually, our thick iron-oxide and silicon device is a heterojunction structure in which recombination junction exists. The number concentration of holes generated in silicon and electrons generated in iron-oxide must be balanced, otherwise, the current is limited by lower concentration carriers. If ideally designed, this heterojunction device produces higher circuit voltage and lower current than single cell, but overall equivalent or better light harvesting capability. However, photovoltaic performance of iron-oxide is not as efficient as silicon because its short diffusion length easily scavenges generated carriers, decreasing collectable carrier concentration. Since one layer is much poorer than the other, the heterojunction devices of silicon and iron-oxide semiconductors likely perform poorer than standalone silicon photovoltaic devices.
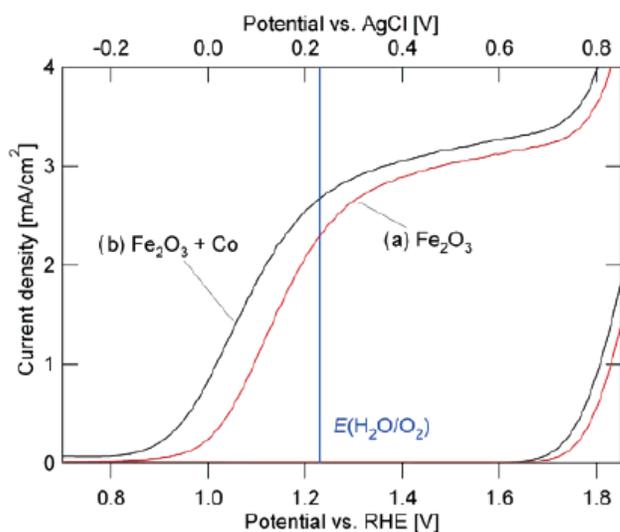
Figure 4.9 Photocurrent at dendrite iron-oxide photoanode

Consequently, our trial comes down to avoid heterojunction, but facilitate silicon as an exclusive light absorption material. To achieve this, very thin film must be deposited. Figure 4.10 plots photocurrents from iron-oxide films deposited at the same conditions(250 sccm titanium precursor, 10 minutes deposition time) but deposition temperatures(250~290 ℃). Since our condition is reaction limited regime, temperature control impacts greatly on thickness. Figure 4.10(left) plots both illuminated

and dark current on all samples. Apparently, dark currents remain near zero throughout the potential range. For simplicity, only illuminated currents will be plotted unless specified.
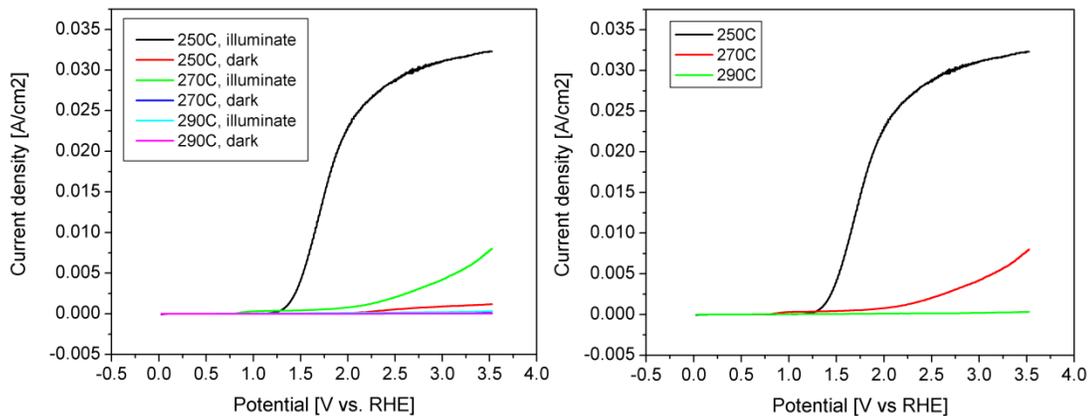
Figure 4.10 Photocurrent of iron-oxide films deposited at different temperatures(250, 270 and 290 ℃) with 250 sccm Ti precursor flow rate. Measurement at pH=13.8. (left) illuminated and dark currents and (right) illuminated currents only.

Surprisingly, at 250 ℃, very high photocurrent was observed. At gentle overpotential, on the order of 10 mA/cm^2 current density was easily achieved. There is a notable transition between 250 ℃ film(about 20 nm) and 270 ℃ film(about 80~90 nm). To see more precise picture, it is necessary to deposit films with thickness in the range of 20~90 nm. However, temperature sensitivity of deposition rate makes it hard to control. Also, different temperatures possibly lead to different film characteristics. Therefore, using slow deposition rate at a fixed temperature(250 ℃, 2 nm/min), time was instead controlled to prepare finely controlled film thickness.
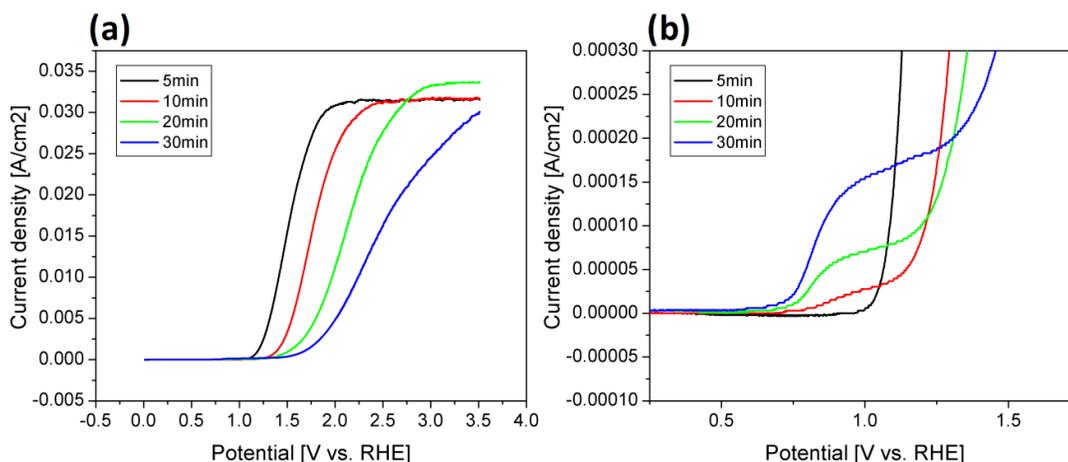
Figure 4.11 Photocurrent of iron-oxide films at different deposition time(5 to 30 minutes). (a) full scale plot and (b) magnified plot near 1 V vs. RHE.

Figure 4.11(a) shows results of 5, 10, 20 and 30 minutes deposited films, that is, 10, 20, 40 and 60 nm thickness. Consistently, thicker films yield lower photocurrent at a given potential, or require high overpotentials for a designated current density. This performance aggravation becomes obvious on 30 minutes(60 nm) film with observable inflection in slope. Therefore, it is believed that the photoresponse experiences a major change of mechanism in the film thickness of 60~80 nm, although the physical and chemical differences between films grown at 250 ℃ and 270 ℃ may induce some variation.

Seemingly, the photocurrents begin their onset at and after 1.1 V vs. RHE. However, when figure 4.11(a) is magnified as in figure 4.11(b) near the onset potential, 'real' onset starts at 0.8 V vs. RHE, resembling isolated iron-oxide photoanode.[49, 51, 57, 128] This initial photocurrent is proportional to iron-oxide film thickness, which is opposite to macroscopic trend. It is understood that iron-oxide photocarrier generation increases according to film thickness to some extent, typically to a few hundreds of nanometers due to long absorption depth.[129] And, this plot manifests the existence of heterojunction, even though weak. However, the current level at this potential is negligibly small, so soon overwhelmed by major current starting from 1.1 V vs. RHE.
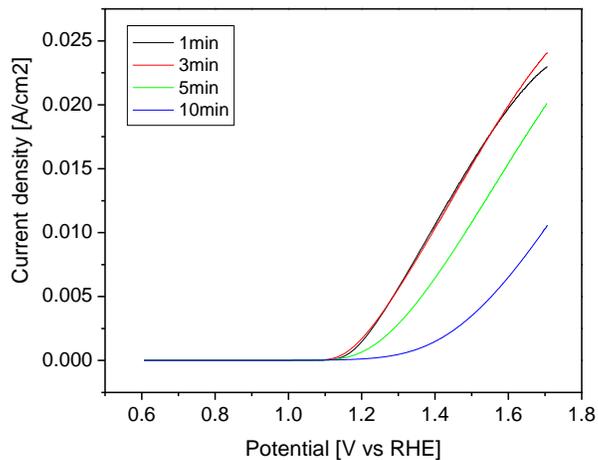
Figure 4.12 Photocurrent of iron-oxide films of very thin deposition, pH=12.

In previous experiments, qualitatively, thinner film shows better performance. By decreasing the thickness more, figure 4.12 is plotted for films ranging from 1 to 10 minutes deposition. From this plot, photocurrent continues to increase till 3 minutes film, and saturate from this point on.

Note that 1 and 3 minutes are so short time that it is hard to say the CVD process reaches to stable deposition rate. Therefore, unless deposited in the same batch, films frequently show inconsistent performance. In this reason, 5 minutes(10 nm) film will be regarded as the thinnest film with reliably reproducible characteristic.

4.2.2 Photocurrent by chemical composition
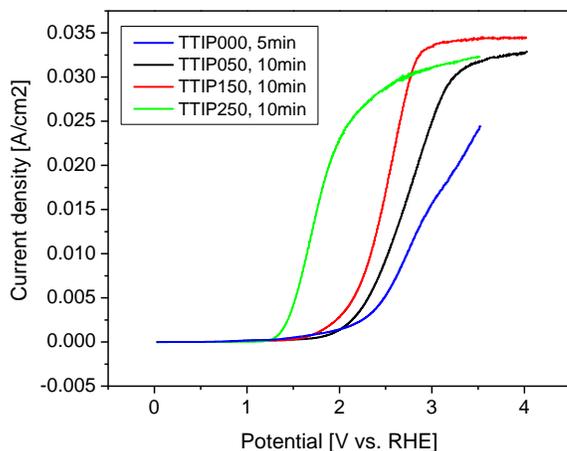
Figure 4.13 Photoresponse of iron-oxide films at different doping compositions.(dopant gas flow rate) Doped samples with 10 minutes deposition and undoped sample with 5 minutes deposition. Measurement at pH=13.8.

Titanium contents were varied and corresponding photoresponses are presented in figure 4.13. Titanium precursor gas flow rate changed from 0 to 250 sccm, while substrate temperature was maintained to 250 ℃. Deposition time for titanium doped samples was 10 minutes and iron-oxide only sample was 5 minutes.

The photocurrents increase with titanium precursor flow rate. Although non-doped iron-oxide shows photoresponse, the operational potential far exceeds practical operation limit, compared to other doped samples. Therefore, titanium doping seems to play an important role to decrease overpotential. Generally, titanium doping is intended to improve photoresponse of iron-oxide. However, considering the expected effect is to improve electrical property, doping should also be beneficial to catalytic performance, since iron-oxide is also a current flow channel between electrolyte and silicon.

Here, 250 sccm is the maximum flow rate in our small bubbling system, so further increase couldn't be tested. Seeing titanium content plays an important role, it was questionable whether pure titanium oxide film can catalyst the reaction. As a simple check, a titanium oxide film was deposited on silicon; iron precursor was removed and only titanium precursor was supplied at 250 ℃. Two deposition times, 10 and 30 minutes samples were prepared and measured at pH=13.8 as in figure 4.14(a) and (b).
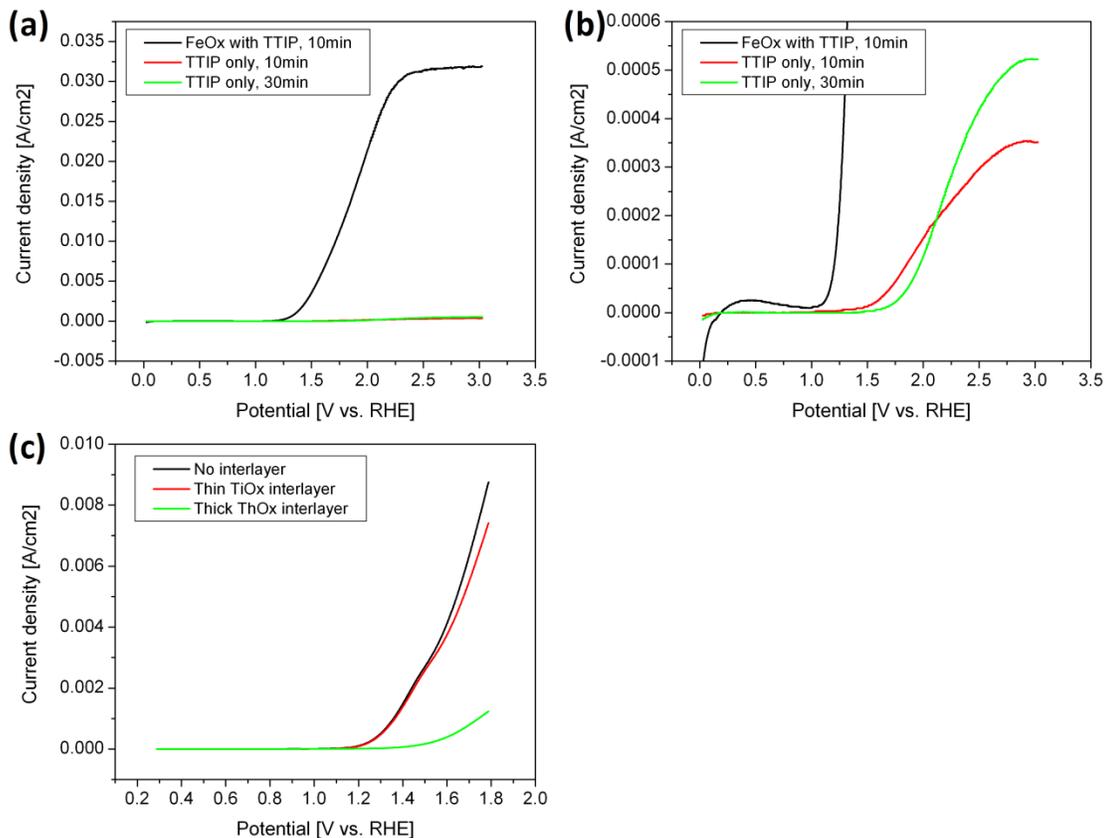
Figure 4.14 (a) Photocurrent comparison of Ti doped iron-oxide and pure titanium-oxide with different thickness, (b) magnified plot of (a), (c) photocurrent of samples with titanium-oxide interlayer between iron-oxide and silicon, thin and thick(about 10 seconds and 10 minutes TTIP flow before iron pentacarbonyl initiation, respectively), (a)(b) measured at pH=13.8 and (c) at pH=10.

Only with titanium-oxide, no meaningful photocurrent was detected. Although the titanium-oxide is not an optimized film, it seems obvious that titanium alone cannot catalyze the anode reaction. Indeed, it is a supporting element for iron-oxide functioning.

Finally, titanium-oxide film was deposited as a interlayer between iron-oxide(doped with titanium) and silicon. Initially, only titanium isopropoxide carrier was turned on while iron pentacarbonyl carrier was off. After designated time(delay time), iron pentacarbonyl carrier was turned on and deposited for 10 minutes. For thin and thick interlayer deposition, the delay time was set to 10 seconds and 10 minutes. The result in figure 4.14(c) indicates that when the interlayer is very thin, the original characteristic is maintained. However, as the interlayer gets thicker, photoresponse decreases. From this observation, it is believed that very thin interlayer may be added for the purpose of silicon protection or adhesion promotion without disturbing the device characteristics.

80

4.2.3 Annealing effect

Typically, CVD film experiences improvements in various properties after high temperature annealing because polycrystalline film is sintered to form larger domain. This contributes improved electrical and mechanical properties. Also, dopant usually requires activation process, which is high temperature annealing. Therefore, we conducted an annealing of iron-oxide film(20 nm thick) deposited with 250 sccm titanium doping.
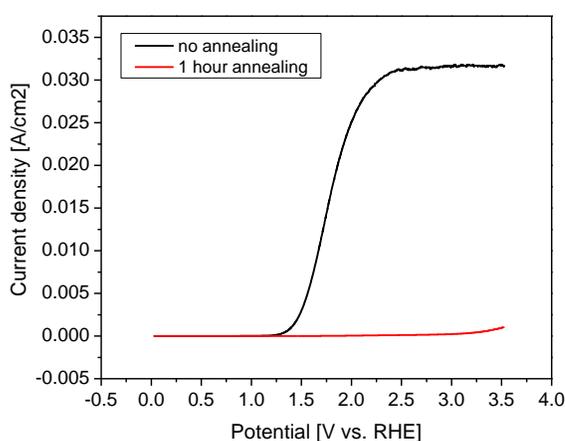
Figure 4.15 Photocurrent measurement after iron-oxide film annealing

Figure 4.15 illustrates the illuminated photoresponses of the sample before and after annealing at 580 ℃ for 1 hour in argon environment. This temperature was chosen to prevent reduction, rather promote hematite transition.[125, 130] Clearly, the activity of the photoanode disappeared after the annealing, which is opposite to other research.[131] A couple possibilities can be suggested to explain this observation.

First is silicide formation. At elevated temperature(~600 C), silicon-rich iron silicon(β-FeSi2) can be formed.[132] Even at room temperature, when bulk Fe-Si system exists, silicide formation has been reported.[133] Since our iron-oxide is very thin, it is possible that iron-oxide is fully depleted once silicidation is initiated.

Second is the iron-oxide phase change. The XPS result implies that our iron-oxide film is very vulnerable to external stimulation, and easily changes its phase. From a report,[134] it is assumed that iron-oxide is prone to reduction at high temperature compared to other oxides like TiO_2. On this account, instead of argon, annealing under oxygen atmosphere was tried, but shows no big difference. Rather than

chemical composition, structural changes could be more plausible cause. It has been reported that lattice parameter in '*c*' direction changes by thermal treatment.[131, 135] Although this is beneficial to optical property by red-shift, catalytic functionality might be hampered by the structural change.

Finally, titanium might be overly activated, so iron-oxide becomes degenerate semiconductor. In spite of large titanium content, it is believed that only tiny fraction of titanium is electrically activated. However, at elevated temperature, it is possible that significant portion of titanium might be activated so donate carriers. Further details about this issue will be discussed in section 4.3.4.

Since annealing was proven to aggravate the performance, no annealing was conducted for later experiments.

4.2.4 Photocurrent by solution pH
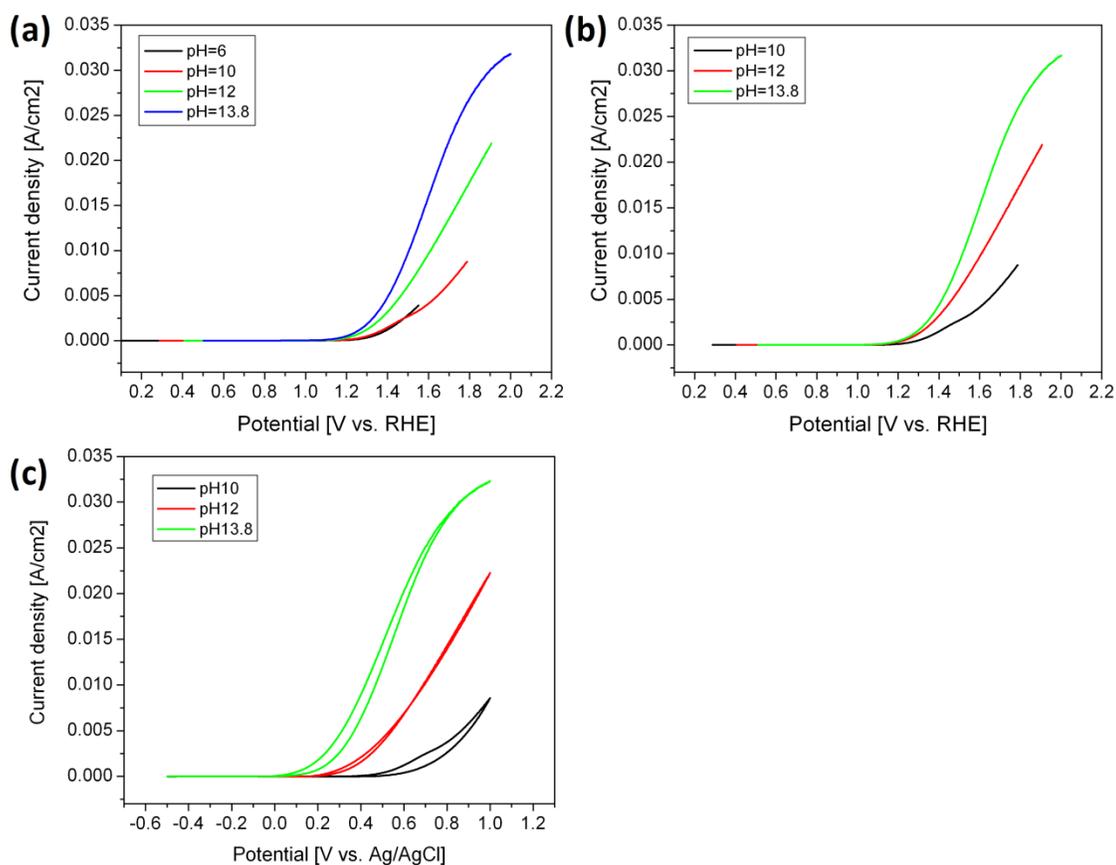
Figure 4.16 Photocurrent of iron-oxide film deposited for 10 minutes. Measured at different pH. (a) all pH values, (b) excluding pH=6, (c) cyclic voltammetry of (b).

Photoresponses were measured at different pH using identical samples, silicon photoanode with 10 minutes deposition iron-oxide with 250 sccm titanium doping. Figure 4.16 describes photoresponse at pH=6, 10, 12 and 13.8, respectively, showing steep slope at higher pH. From a literature,[71] it is explained that increased concentration of OH^- group effectively traps hole from the electrode surface fast enough, therefore resultant carrier-to-ion transfer rate increases. This implies high pH operation is beneficial for our photoanode operation.

However, practical consideration is the electrode stability. Although iron-oxide itself is stable in this pH and potential range,[72] silicon electrode can be attacked by hydroxyl ions by following reactions.[136, 137]

$$Si + 2OH^- \rightarrow Si(OH)_2^{2+} + 2e^-$$
$$Si(OH)_2^{2+} + 2OH^- \rightarrow Si(OH)_4 + 2e^-$$
$$Si(OH)_4 + 4e^- + 4H_2O \rightarrow Si(OH)_6^{2-} + 2H_2$$
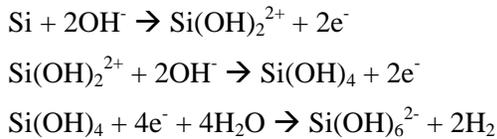
Equation 4.1 Silicon etching in basic solution.

Although iron-oxide film may play a role as a protection layer, the very thin film may not completely protect the underlying silicon. Consequently, in addition to other protection methods, it is desirable to operate at low pH, so low pH response is also ponderable. In this reason, later experiments will characterize photoanode performances both at pH 13.8 and 12.

About this issue, if the photoelectrode is compatible with (111) directed silicon, the substrate stability could be improved greatly. Following figure 4.17 compares the performance of (100) and (111) silicon with the same iron-oxide film, indicating no difference in photoresponse. Simple metric yields 2~3 order of etching resistance in basic solution. Further discussion about operation stability will be in section 4.5.1.
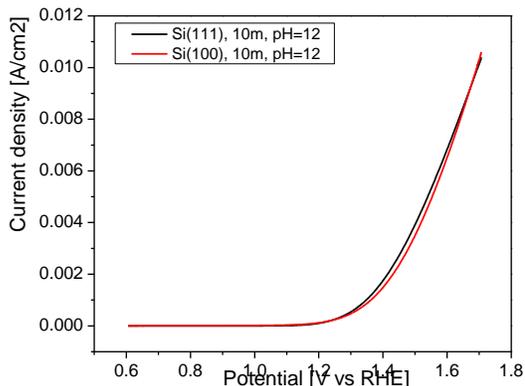
Figure 4.17 Photoresponse comparison of (100) and (111) oriented silicon substrate.

4.3 Analytical investigation of photocurrent origin

In section 4.2, high photocurrent was observed in silicon based photoanode. Bare silicon is not compatible with anode reaction as shown in figure 4.7, however when catalyzed by iron-oxide, the reaction seems to work with a good performance. In this section, the working mechanism of silicon photoanode will be explored using various analytical measurements and theories.

4.3.1 Light absorption by iron-oxide film

First step is to clarify the origin of photocarriers. In our earlier discussion, 200 nm film was defined as 'thick', while 10 nm was defined as 'thin'. The criteria must be whether the carrier generation by iron-oxide is large enough to contribute obvious heterojunction characteristic. Although absorbed light cannot be directly translated into photocarrier generation, these two are closely related. Therefore, calculating light absorption by iron-oxide film is a good starting point.

Light absorption of planar iron-oxide film on silicon substrate was calculated from 400 nm to 700 nm wavelength. Figure 4.18(a) draws the model and equation 4.2 list the formula used in the calculation.[138] Fitted materials' data(refractive index) is provided in Appendix 6.1.
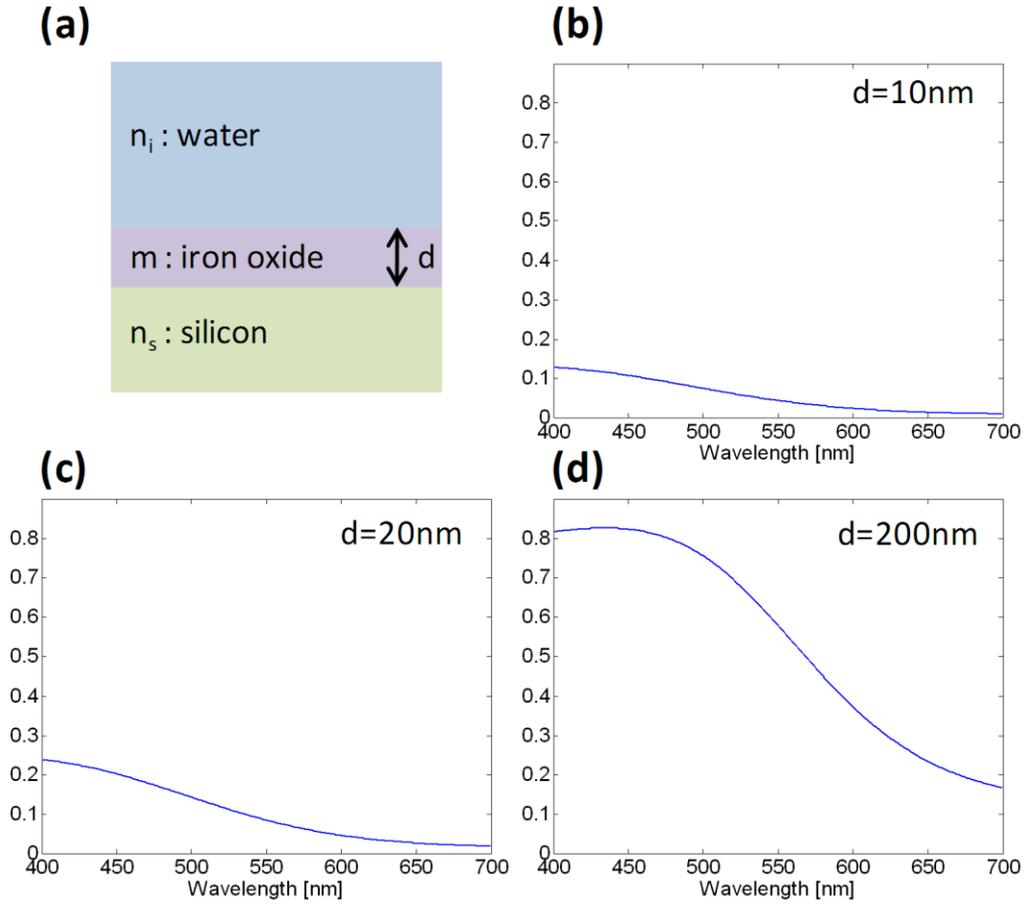
Figure 4.18 Light absorption model and calculated results.

$$A = 1 - |\bar{r}|^2 - C|\bar{t}|^2$$

$$\bar{r} = \frac{r_i - r_s\gamma^2}{1 - r_i r_s \gamma^2}, \quad \bar{t} = \frac{(1+r_i)(1-r_s)\gamma}{1 - r_i r_s \gamma^2} \exp(-in_s\delta), \quad C = \frac{n_s}{n_i}$$

$$m = n + i\kappa, \quad r_x = \frac{(n_x - m)}{(n_x + m)} \text{ with } x = i, s$$

wavelength λ_0, wavenumber $q_0 = \dfrac{2\pi}{\lambda_0}$

$\delta \equiv q_0 d$ with thickness d, $\gamma \equiv \exp(im\delta)$

Equation 4.2 Formulas for light absorption calculation.

From figure 4.18(b)~(d), light absorption near iron-oxide band gap(~560 nm) decreases over 200~300 nm range. Thin films like 10 and 20 nm absorb less than 10~20 % of incident light, while 200 nm film can absorb as much as 80 % of light. Experimentally,[129] a 31 nm iron-oxide photoanode showed only about 0.15 mA/cm^2 of photocurrent compared to the previous result(about 3 mA/cm^2) of thicker film reported by the same group. Therefore, it should be possible to call 10~20 nm or less film as 'thin film'. This is consistent with the very small current onset driven by thin iron-oxide photocarriers in figure 4.11(b).

4.3.2 Incident Photon to Current Efficiency(IPCE)

In section 4.3.1, it was shown that the majority of the photocarriers are not coming from iron-oxide. Then, it looks obvious that silicon is the primary light absorption layer. To verify the silicon photocarrier generation as well as the performance of silicon photoelectrode, incident photon to current efficiency(IPCE) was measured.

Measurement conditions were 1.6 V vs. RHE at pH=12 using 10 minutes deposition sample. Initially, photocurrent at each wavelength was measured by a quantum efficiency measurement system(QEX7, PV Measurements) and potentiostat(Reference600, Gamry). Scanning was set to 10 nm step with 5 second measurement without chopping.

To calculate IPCE, we need reflectance information. Our sample is immersed in electrolyte, consequently, there are two reflection interfaces, air-to-water and water-to-substrate(Figure 4.19(a)). This reflection cannot be directly measured by the spectrometer due to the water environment. Instead, we decided to adopt a theoretical calculation with the model used for the light absorption calculation. However, it was uncertain whether this model can reliably predict reflectance. To verify the validity of this model, we did following comparison.

First, the reflectance at the air-to-substrate interface was calculated by the model.(Actually, air to substrate interface consists of two interfaces: air-to-iron oxide and iron oxide-to-silicon. The model does consider these two combined effects. For convenience, it will be called a single interface.) At the same time, the sample's reflectance in the air environment was measured using UV-VIS-NIR spectrophotometer(Lambda 950, PerkinElmer, with Thorlab P01 coating silver mirror). Then, these two results were compared as in Figure 4.19(b), which shows general coincidence below 1050 nm. This indicates that the model can be reliably applied to calculate reflectance.

After confirming the validity, we calculated the reflected and transmitted light intensity in a water environment as plotted in figure 4.19(c). The computation details are summarized in Appendix 6.2.
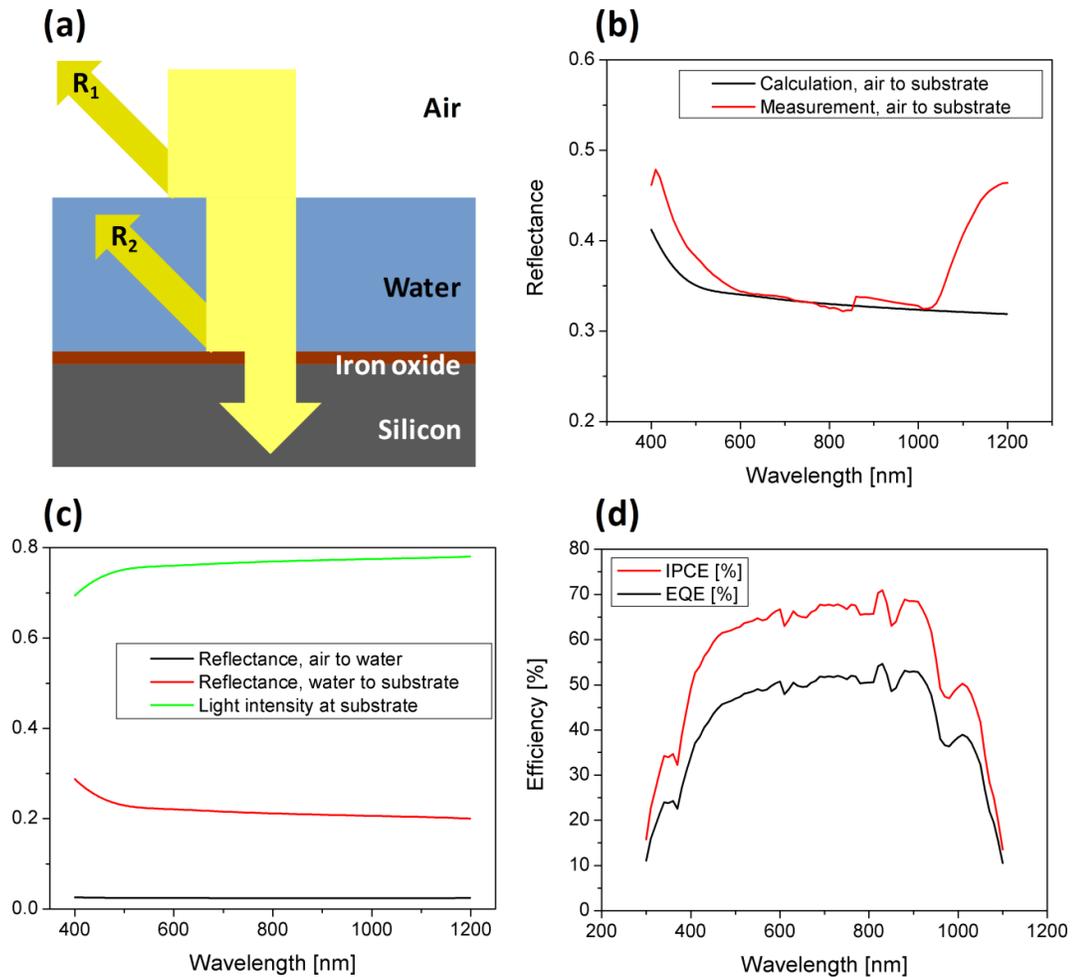
Figure 4.19 IPCE calculation (a) reflectance model, (b) reference data comparing modeled and measured ait-to-substrate reflectance, (c) calculated air-to-water and water-to-substrate reflectance, and resultant light intensity on immersed substrate, (d) measured EQE and calculated IPCE.

Measured external quantum efficiency(EQE) is the black line in figure 4.19(d), and IPCE(red line) is calculated using EQE and light intensity data in figure 4.19(c). It is worth pointing two observations. First is the light absorption in wide wavelength range. Quantum efficiency drops around 1000 nm, which corresponds to silicon band gap energy of 1.12 eV(λ = 1109 nm). This clearly demonstrates that the carrier generation dominantly happens in silicon. Note that short wavelength performance(400~600 nm) is slightly poorer than long wavelength performance. Typically, photovoltaic semiconductors including silicon devices show higher performance at short wavelength. In our case, thin iron-oxide top layer

absorbs 10~20 % of short wavelength spectrum, which may be the reason of slight loss of incident light. If thinner iron-oxide film is used, some of this loss could be recovered.

Second point is the high IPCE numeric values in wide wavelength range. We gave up heterojunction of iron-oxide and silicon due to the assumption of low photoconversion efficiency in oxide semiconductor. Reported iron-oxide IPCE as shown in figure 4.20,[57] which is from one of the highest performance iron-oxide photoanodes, supports this assumption. At very short wavelength, IPCE reaches as high as 50 %. However, although the iron-oxide band gap of 2.2 eV is regarded ideal for visible light absorption, the absorption edge is not sharp. Instead, IPCE gradually decreases, so in the highest energy solar spectrum range, 400~550 nm, IPCE is merely 35 % or less. Then, energy equivalent band-gap of iron-oxide is wider than its nominal 2.2 eV value. On the contrary, our silicon device maintains 60~70 % of IPCE over the usable spectrum ranges. This is clear evidence of single cell silicon device advantage.
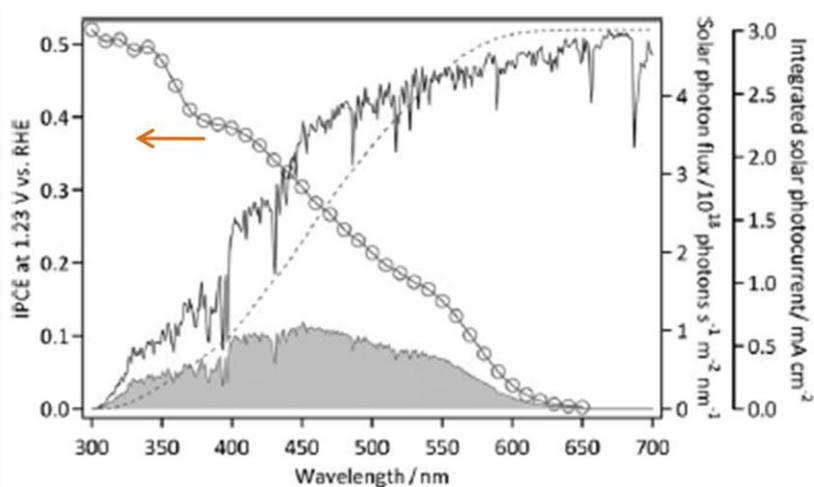
Figure 4.20 IPCE measurement of iron-oxide film.

4.3.3 Catalytic effect of iron-oxide

Since photocarriers are generated by silicon, the role of iron-oxide should be catalysis of water oxidation. Thus, the catalytic functionality of iron-oxide was further evaluated in controlled conditions.

First evaluation is the relationship between catalysis and light absorption. When iron-oxide sits on silicon surface, its intrinsic catalytic functionality is mixed with photovoltaic performance of the cell. Therefore, to eliminate photocarriers effect, iron-oxide was deposited on metallic ITO substrate for 10 minutes(~20 nm), and the current density was measured with and without light illumination at pH=13.8 as in figure 4.21(a) and (b). Regardless of the light illumination, the current curves were identical. This

implies that light absorption is so negligible that the catalytic functionality of this thin iron-oxide film is independent of illumination in this metallic substrate.

Next, iron-oxide(20 nm, 10 minutes deposition) and platinum(5 nm by sputtering) were deposited on ITO substrate respectively and their dark currents were recorded as described in figure 4.21(c) and (d). Compared to bare ITO substrate, both platinum and iron-oxide possess catalytic functionality. Relative comparison between these two catalysts reveals that iron-oxide performs better than platinum. In similar comparison of figure 4.21(e) where iron-oxide was deposited on platinum substrate, iron-oxide sample again showed better catalytic effect than bare platinum substrate. Similar level of onset potential(1.6 ~ 1.7 V vs. RHE) has been reported in dark current experiments elsewhere.[139, 140]

Differences on substrates were observed when iron-oxide films were deposited on different types of substrates. Three different cases are drawn in figure 4.21(f) – that is, iron-oxide on ITO substrate, iron-oxide on platinum and iron-oxide on silicon. All iron-oxide films were deposited at the same conditions for 10 minutes. Former two are the values of dark measurements, which are identical to illuminated measurements, and the latter is illuminated measurement. Notably, from zero to decent overpotential region,(1.23~2.0 V vs. RHE) silicon electrode outperformed platinum and ITO substrates. Since conductive surfaces have much higher carrier density than silicon, the current in this potential region is believed to be controlled by reaction rate rather than absolute carrier density. Later at high potential region, metallic surfaces perform better than silicon substrate because the number concentration of silicon photocarriers is limited, so the carriers are depleted at certain point. But this potential is far beyond practical operation potential.

From this observation, it is thought that, although iron-oxide is a decent catalyst for water oxidation, the high photocurrent in our photoanode does not originate solely from iron-oxide functionality. Similarly, silicon alone cannot provide high photoresponse when combined with other catalysts except iron-oxide as in figure 4.21(g). Rather, there seems to be a synergic interaction between iron-oxide and silicon.
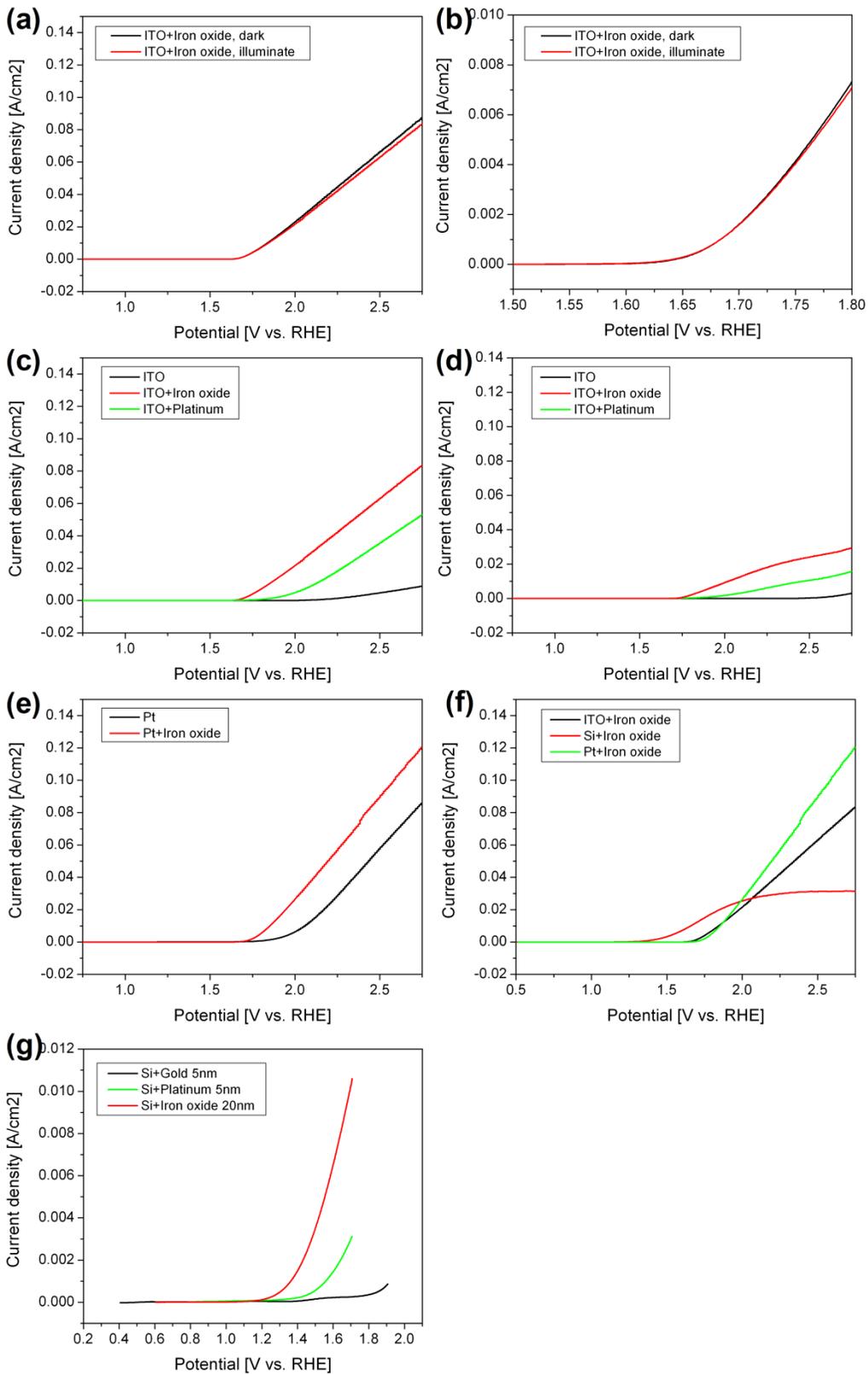
Figure 4.21 Catalytic effect comparison. (a) photoresponse comparison, 20nm iron-oxide on ITO substrate, (b) magnified figure of (a), (c) different catalysts on ITO substrate, bare ITO, iron-oxide(20 nm) and platinum(5 nm) deposited ITO measured at pH=13.8, (d) same experiment of (c) measured in pH=12, (e) iron-oxide catalysis comparison, bare platinum substrate and iron-oxide(20 nm) deposited platinum substrate, (f) substrate comparison, iron-oxide(20 nm) deposition on ITO, silicon and platinum substrate, (g) catalyst comparison on silicon substrate, golf(5 nm), platinum(5 nm) and iron-oxide(20 nm) on silicon substrate. Measurement conditions: (a)(b)(c)(e)(f) pH=13.8, (d)(g) pH=12, all silicon substrates under illuminated condition, all metallic substrates under dark condition except (a).

4.3.4 Electronic property of iron-oxide film

The differences of substrate, metallic or semiconducting, made a significant difference of performance in section 4.3.3. Therefore, the reaction mechanisms of two different types of electrodes, metal electrode and semiconductor electrode were analyzed. Before doing this analysis, the electronic property of iron-oxide must be identified for the following reason.

The circuit consists of a serial connection of silicon, iron-oxide and electrolyte. Depending on iron-oxide coverage on silicon surface, there could be direct contact between electrolyte and silicon, and it is very probable because polycrystalline film with less than 10 nm thickness cannot cover the underlying layer without voids. However, no current exchange is observed in silicon and electrolyte direct junction. Therefore, at any case, current must flow through silicon, iron-oxide and electrolyte path(figure 4.22).
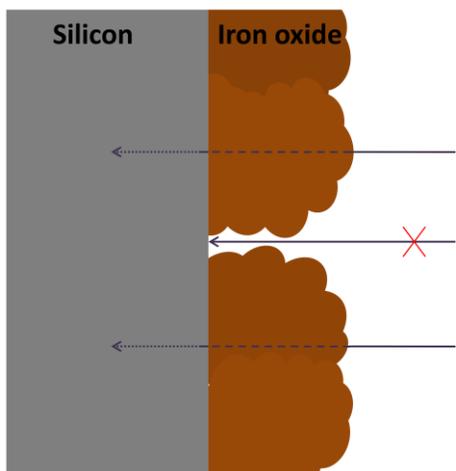
Figure 4.22 Schematic diagram of silicon, iron-oxide and electrolyte junction.

If we are supposed to apply semiconductor electrode scheme between silicon and electrolyte, iron-oxide must not be metallic or degenerate. Otherwise, no space charge is allowed in iron-oxide, and Fermi

level is pinned in the iron-oxide. However, considering very high titanium content, which is about 4 %, it is also possible that our iron-oxide falls in degenerate regime.

The most straightforward method is to measure Hall voltage, by which we can calculate carrier density. For Hall measurement, 300 nm film(150 minutes deposition) was prepared on oxidized silicon substrate, followed by 30 nm gold evaporation at four corners of the substrate as electrode contacts. Unfortunately, this sample could not provide meaningful signal from Hall measurement. As an alternative approach, we calculated resistivity using four point I-V measurement as shown in figure 4.23.
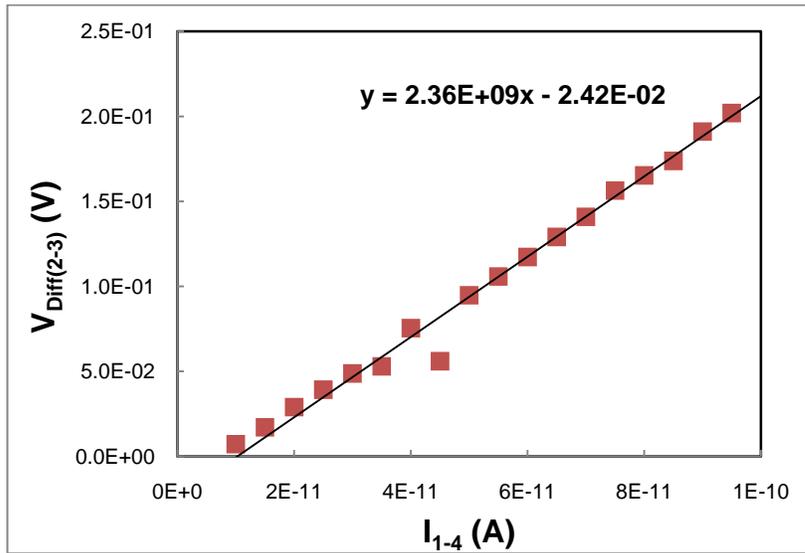
Resistance = $2.36*10^9$ Ω ➔ Sheet resistance = $10.7*10^9$ Ω/sq. ➔ Resistivity = $3.21*10^5$ Ω-cm where L/W = 4.532 and film thickness = 300 nm

Figure 4.23 Iron oxide film I-V curve.

Considering the thickness, film resistivity is estimated to be about $3*10^5$ Ω-cm. From references,[141, 142] this is very close to intrinsic iron-oxide resistivity. In another reference,[143] iron-oxide(hematite) film with resistivity of about 1 Ω-cm shows carrier concentration of 10^{16}~10^{17} cm^{-3}. Therefore, our iron-oxide should have much lower carrier density, meaning it is clearly in nondegenerate semiconductor regime.

If the dopants are properly activated, carrier density of 10^{18}~10^{20} cm^{-3} is easily observed.[78, 144] However, in this case, the activation requires high temperature annealing. For example, titanium is known to necessitate as high as 800 ℃ temperature.[131, 145] Since our deposition temperature is merely 200 ℃ or less with no extra annealing, the portion of activated titanium must be significantly lower than the nominal 4 % content. Still, it is uncertain whether there is another role of titanium in iron-oxide matrix

except doping. If doping is the only contribution, proper titanium activation without losing degenerate nature is expected to improve the catalytic performance.

4.3.5 Flat band potential of photoanode

To establish semiconductor electrode and electrolyte junction model, the last piece of missing information is the band edge positions of our photoanode in electrolyte. Compared to other semiconductor materials, silicon band edge position is rather obscure because it does not follow Nernst relation. Although there are some published values,[70] the deviation is large. Also, we need other conditions such as solution pH, solutes and substrate doping level. Considering all these factors, it is necessary to measure the flat band potential of our photoelectrode, and calculate the band edge positions.

For flat band potential measurement, devices were made of n^+ back doped silicon substrates to minimize the effect of Schottky space charge region. Iron-oxide films were prepared for various thickness of 0, 6, 10 and 20 nm,(0, 3, 5 and 10 minutes deposition) and three different pH electrolytes(10, 12 and 13.8) were also prepared. Potentiostat(Reference600, Gamry) environment was configured to draw Mott-Schottky plot. Fluctuation voltage was set to 5 mV rms. Potential scan started from 0.5 V vs. Ag/AgCl to cathodic direction.(End points vary on samples, typically -0.8 ~ -0.9 V vs. Ag/AgCl) Operation frequency was 20 and 50 kHz, which gave almost identical values. All measurements were conducted after 5 minutes open circuit delay under dark environment. For analysis, a model with series connection of a resistor and a capacitor was adopted.
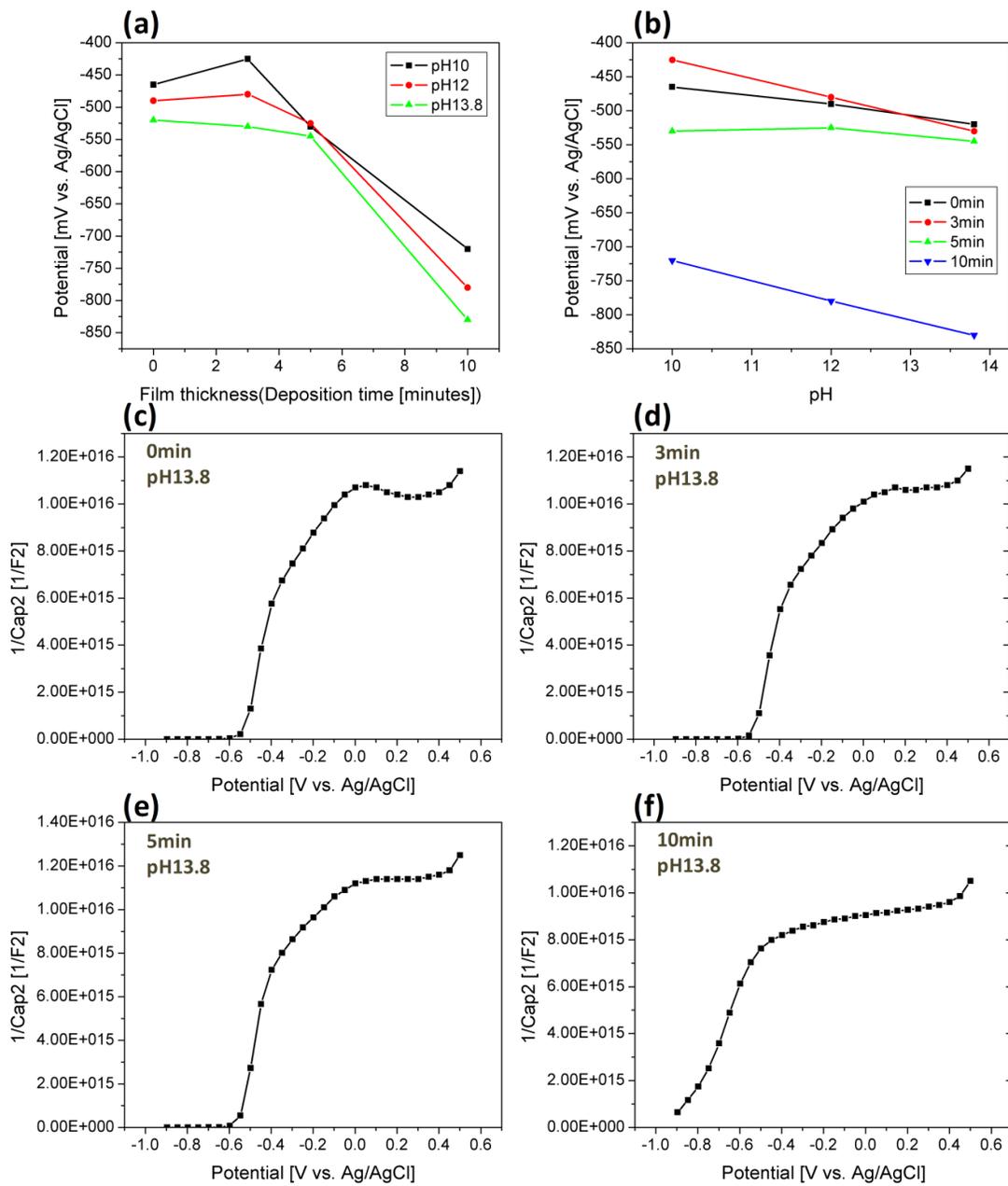
Figure 4.24 Flat band potential. (a) flat band potential vs. film thickness at each pH, (b) flat band potential vs. pH at each film thickness, (c)~(f) Mott-Schottky plot of various thickness film at pH=13.8.

Deposition time [s] (Thickness [nm])	Flat band potential [mV vs. Ag/AgCl]			Avg. slope [mV/pH]
	pH 10	pH 12	pH 13.8	
0 (0)	-465	-490	-520	-14.47
3 (6)	-425	-480	-530	-27.63
5 (10)	-530	-525	-545	-3.94
10 (20)	-720	-780	-830	-28.95

Table 4.2 Slope and flat band potential data

Figure 4.24(a) illustrates flat band potential vs. film thickness plot. Notably, when the iron-oxide is thin(< 10 nm), flat band potential remains similar to bare silicon value, around -0.5 V vs. Ag/AgCl. 20 nm films show rapid shifts of flat band potential. From figure 4.24(b) of flat band potential vs. pH, the slope is -10~-30 mV/pH excluding rather erratic 5 minutes samples. As predicted, the slope of all samples including the thickest 20 nm sample is much smaller than Nernst relation, -59 mV/pH as shown in table 4.2. Figure 4.24(c)~(f) show the Mott-Schottky diagrams of four different film thickness samples at pH=13.8.

From this observation, it is thought that the electronic characteristics of the electrodes are governed by silicon characteristic when iron-oxide film, which follows Nernst relation,[78] is thin. This is also consistent with our intention to facilitate silicon as photovoltaic semiconductor but to suppress iron-oxide's involvement in photovoltaic process.

4.3.6 Energy band model

From the information we collected so far, junction energy band diagram can be drawn. Silicon has flat band potential of about -0.5 V vs. Ag/AgCl, and its carrier density is estimated to be about $2.0 * 10^{14}$ cm^{-3} from silicon Mott-Schottky plot, which corresponds to 22 Ω-cm in equation 4.3.[19]

$$\frac{1}{C_{sc}^{2}} = \frac{2}{qN_{sc}\kappa\varepsilon_{0}A^{2}}\left(V - V_{FB} - \frac{kT}{q}\right)$$

$q = 1.6*10^{-19}$ C
$\kappa = 11.68$ for silicon
$\varepsilon_{0} = 8.85*10^{-14}$ F/cm
$A = 1$ cm^{2}
$V =$ applied voltage
$V_{FB} =$ flat band potential
$kT/q = 0.026$ V
$N_{sc} =$ carrier density of space charge region

Example: From measured data at pH=13.8:
$C^{-2} = 5.76*10^{15}$ F^{-2}
$V = -0.398$ V vs. Ag/AgCl
$V_{FB} = -0.52$ V vs. Ag/AgCl
Then, $N_{sc} = 2.0*10^{14}$ cm^{-3}, which correspond to 22 Ω-cm

Equation 4.3 Relationship of space charge capacity and flat band potential, induced from Poisson's equation and Mott-Schottky equation.

$$E_{f} - E_{i} = kT \ln\left(\frac{n_{0}}{n_{i}}\right)$$

$n_{i} = 1.45*10^{10}$ cm^{-3}
$n_{0} = N_{sc}$
$kT = 0.026$ eV
$E_{f} =$ Fermi energy level
$E_{i} =$ intrinsic level
$E_{f} - E_{i} = 0.25$ eV

$V_{FB} = -0.52$ V vs. Ag/AgCl
$E_{g} = 1.12$ eV (silicon band gap)
$E_{c} = -0.83$ V vs. Ag/AgCl (silicon conduction band edge)
$E_{v} = 0.29$ V vs. Ag/AgCl (silicon valence band edge)
OEP=0.2174 V vs. Ag/AgCl at pH=13.8

Equation 4.4 Calculation of various energy levels and band edge positions

Vacuum NHE pH = 0 pH = 14

-3.5 -1.0

2H$^+$ + 2e$^-$ $\leftrightarrow$ H$_2$
0 - 0.0591 x pH (V vs. NHE)

-4.0 -0.5

-4.5 0.0

O$_2$ + 4H$^+$ + 4e$^-$ $\leftrightarrow$ 2H$_2$O
0 - 0.0591 x pH + 1.23 (V vs. NHE)

-5.0 0.5

Si

-5.5 1.0

-6.0 1.5

-6.5 2.0 α-Fe$_2$O$_3$

-7.0 2.5

Flat band condition

E$_c$

0.31

E$_f$

0.25

E$_i$

0.52

0.56

Ag/AgCl

0.29 0.22

OEP

E$_v$
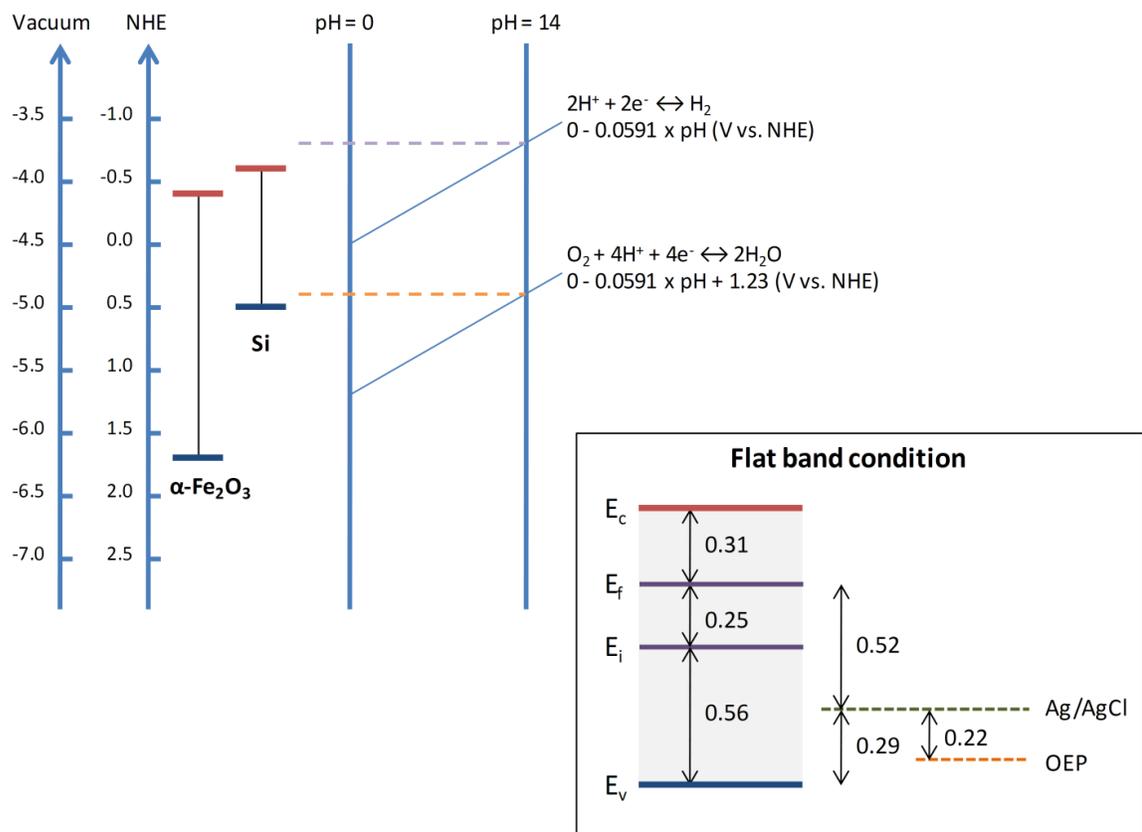
Figure 4.25 Silicon band edge positions and water oxidation potential

From the calculation of equation 4.4, conduction and valence band edge of silicon locate at -0.83 V vs. Ag/AgCl and 0.29 V vs. Ag/AgCl, respectively. By the way, OEP at pH=13.8 is 0.22 V vs. Ag/AgCl. Figure 4.25 draws the relative positions of all these energy levels. Note that these reconstructed silicon band edge positions are numerically similar to those reported previously.[146]

If the electrode-electrolyte junction is in thermal equilibrium, Fermi level of silicon and oxygen evolution potential become continuous. The resultant junction diagram looks like figure 4.26.
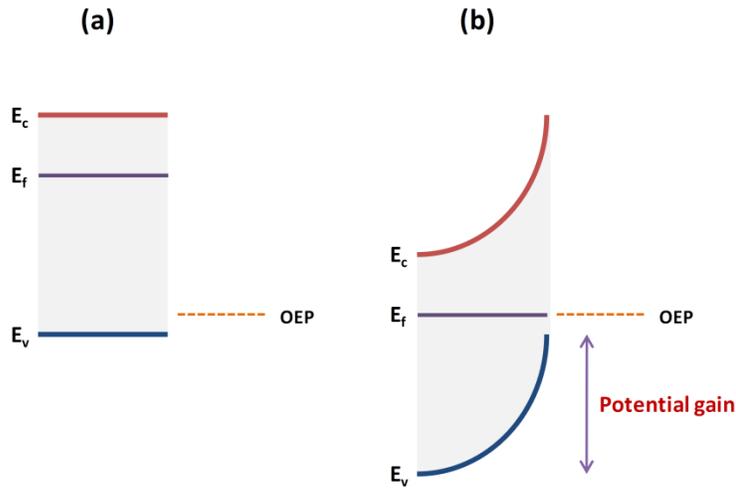
Figure 4.26 Energy band model of the junction. (a) before and (b) after equilibrium.

Indeed, OEP locates higher(more cathodic) than silicon valence band edge. Therefore, energetically, oxygen evolution reaction must happen in silicon and electrolyte junction. However, it is believed that the lack of catalytic functionality of silicon prohibits the procession of the reaction. If proper catalyst like iron-oxide is introduced, now the charge carriers can pass through the junction.

Another important part is the band bending in semiconductor. First, consider the junction of iron-oxide and electrolyte. From Poisson's equation(equation 4.5), the space charge region width can be calculated.

$$V_s = qN_{sc}x_0^2 / 2\kappa\varepsilon_0$$

V_s = surface barrier [V]
$q = 1.6*10^{-19}$ C
N_{sc} = density of positive charge in the space charge layer, a.k.a. doping level
x_0 = depletion thickness [cm]
κ = dielectric constant
ε_0 = vacuum permittivity = $8.85*10^{-12}$ F/m = $8.85*10^{-14}$ F/cm

Iron oxide example:
$V_s = 0.7$ V
$\kappa = 60$
$N_{sc} = 1*10^{16}$ cm^{-3}
$x_0 = 680$ nm

Equation 4.5 Poisson's equation and calculated space charge thickness in iron-oxide

Since we don't know the Fermi level of our iron-oxide, it was estimated from known flat band potential.(-0.6 V vs. standard calomel electrode(SCE))[147] Then, the surface barrier(difference between iron-oxide Fermi level and OEP) is about 0.7 V. When iron-oxide carrier concentration is assumed about 10^{16} cm^{-3} with dielectric constant about 60,[142, 148] space charge region thickness is about 680 nm. In fact, our iron-oxide has much lower carrier concentration, which means even thicker space charge region. Definitely, this is much thicker than iron-oxide physical thickness. Therefore, the potential drop by iron-oxide is negligible, and most of the space charge region appears in silicon instead. This induces steep upward bending in silicon energy band structure, so provides potential gain as indicated in figure 4.26. This built-in potential is believed the reason silicon substrate performs better than metallic surface. On the contrary, in metallic substrate, the energy level is not altered, because of ample carrier population. Therefore, the driving force is simply the difference between metals' Fermi energy and OEP which cannot readily exceed the silicon-electrolyte junction built-in potential.

4.3.7 Tafel analysis

Based on semiconductor-electrolyte junction model, the observed photoresponses can be explained by electrochemical anaylsis. Following figures are log-normal plots of thickness and pH variations.

Commonly, current-potential curves start with linear profiles, but soon saturates in log-normal plots. The linear evolution can be explained by Tafel relation in equation 1.2. That is, initially the current is limited by reaction rate since there are enough carriers to sustain the low current level. However, as current increases, it enters to transport limited regime. In metal electrode, the limiting factor is mass transfer in electrolyte, however, in semiconductor electrode, carriers in semiconductor are depleted earlier than mass transport. This eventually induces fully saturated current value, in our silicon photoanode, about 30~40 mA/cm^2.
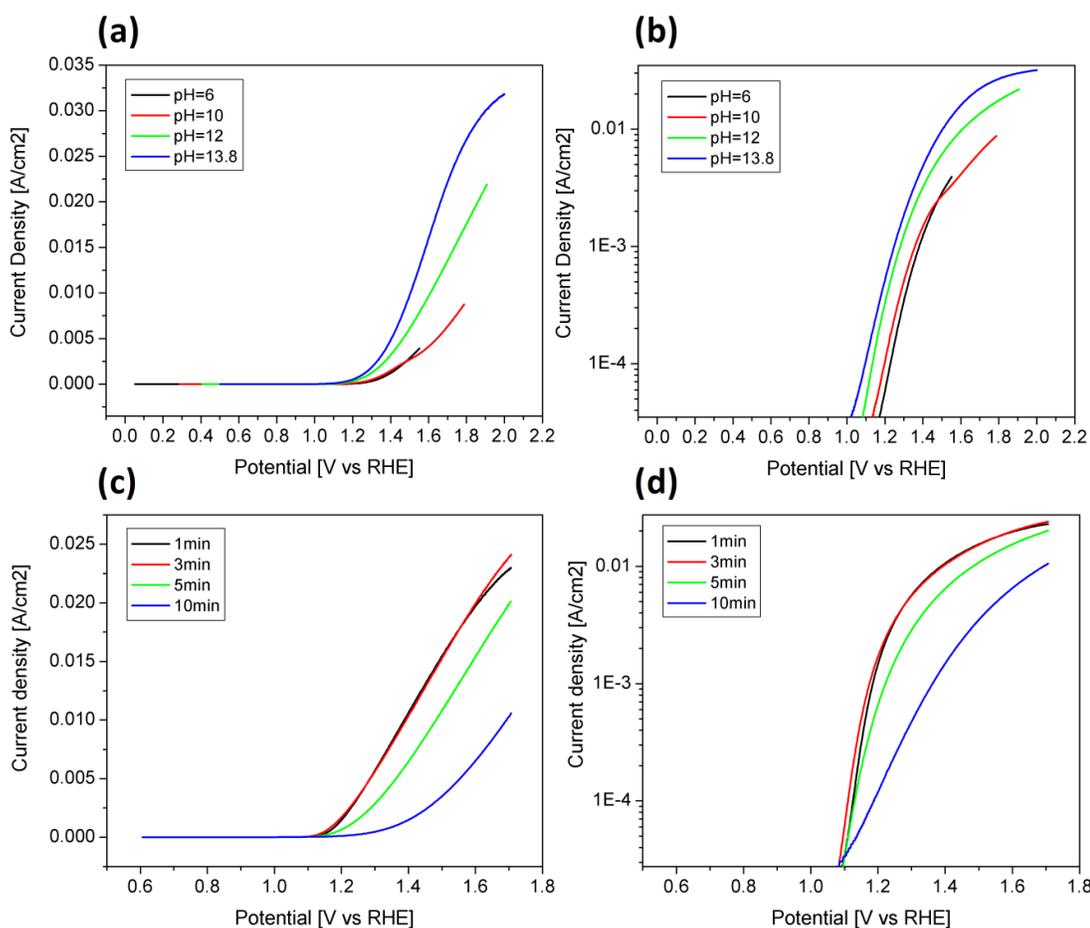
Figure 4.27 (a), (b) Thickness varied photoresponses plots. (a) linear and (b) log-normal. (c), (d) thickness varies photoresponses plots (c) linear and (d) log-normal. (a)(b) 10 minutes deposition film, (c)(d) at pH=12.

In figure 4.27(a) and (b), samples have the same film thickness, but measurement pH changes. Figure 4.27(b) shows same slope among different pH, which means charge transfer coefficients are all the same. Since charge transfer coefficient represents the kinetics of electrochemical reaction, this implies that pH change only induces the overpotential, but no change of physical mechanism.

On the other hand, in the figure 4.27(c) and (d) which plot different thickness films at constant pH, slopes change according to film thickness. Thicker film shows more gradual slope, meaning lagging in current evolution with respect to potential. This changing slope, or charge transfer coefficient, means film thickness does affect the electrochemical kinetics. However, considering the surface characteristic of the electrode does not change with thickness, it should be more reasonable to assume that the carrier transport through the iron-oxide film is affected. As seen in flat band potential, film thickness, even though small, changes the band structure of the hybrid photoanode. More importantly, there is a loss occurred by current

path length through high resistivity iron-oxide film. Therefore, the carrier transport characteristic is thought to be modified by film thickness, resulting in altered electrochemical responses.

4.4 Photoresponse improvement by silicon microfabrication

Until previous section, various parametric studies were conducted mostly on iron-oxide film conditions and electrochemical environment. While chemical reactions are mediated by iron-oxide, photocarriers are generated and transported in silicon substrate. Therefore, device performance relies on the photovoltaic characteristics of silicon, which stresses the importance of silicon manipulation.

Although a rapid current evolution demonstrates a high potential in iron-oxide and silicon photoanode, the photocurrent at zero overpotential(1.23 V vs. RHE) is still low, which is believed to originate from high onset potential. In our silicon device, there are several obvious loss factors. Using well known microfabrication techniques as discussed in section 2.3, an improvement of photoresponse was pursued.

4.4.1 Improvement by silicon wires array

Silicon wires array was fabricated as described in section 3.3. Using the same CVD setup, iron-oxide film was deposited as seen in figure 4.28.
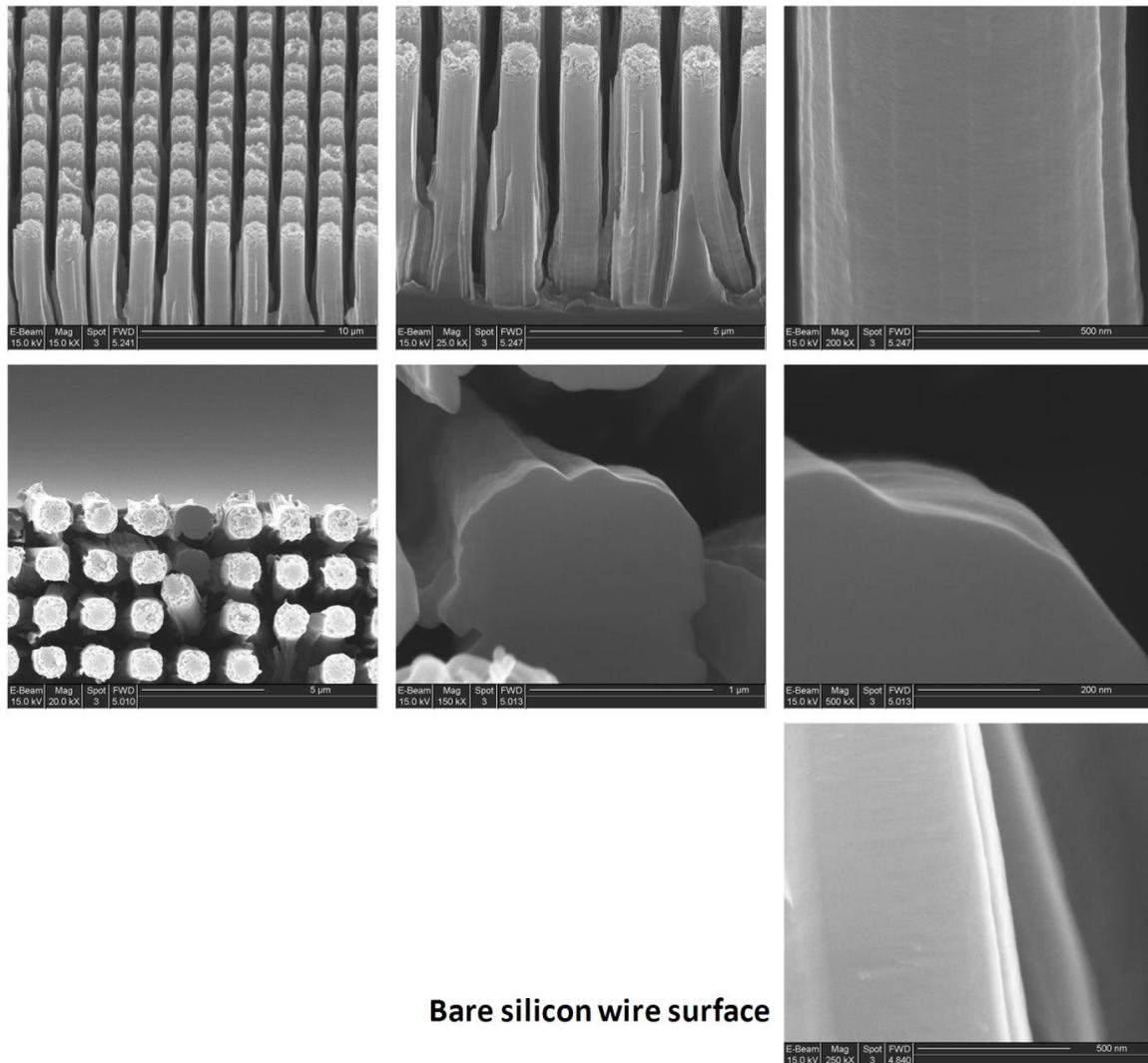
Figure 4.28 Silicon wires array with iron-oxide film deposition, (first row) side view and (second row) top view, (third row) bare silicon wire surface for comparison.

Figures in 4.28 first and third row compare the wire surface morphology with and without iron-oxide film. The film was deposited on 8~10 μm long silicon wires array for 10 minutes. The deposition rate(about 1 nm/min) is slower than flat substrate, estimated half of the flat substrate deposition rate. Figures in 4.28 first row are the observed images from the side, and those in second row are images taken from the top after FIB cutting of wires. Notably, it is very hard to see polycrystalline grains, but surface is generally smooth with random corrugations. In previous film morphology analysis, fast deposition rate produces more rough and spiny shape, while low deposition results in more rounded and coalesced shape. Therefore, the smooth surface is believed to attribute to the slow deposition rate on the sidewall.
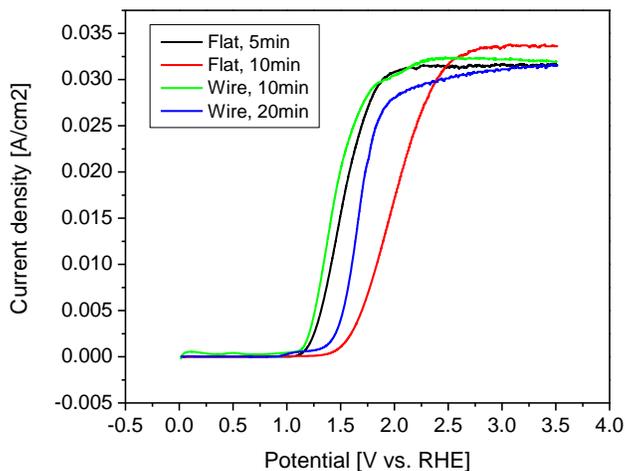
Figure 4.29 Measured photocurrents of iron-oxide and silicon wires array compared to flat silicon substrate. Fiat 5min and wire 10min with 10 nm iron-oxide films, flat 10min and wire 20min with 20 nm iron-oxide films.

Figure 4.29 illustrates the measured photocurrents of two different film thickness wires and flat silicon photoanodes at pH=13.8. In terms of current density at zero overpotential(1.23 V vs. RHE) with 10nm iron-oxide film, wires array showed 3.44 mA/cm^2, while flat substrate showed 1.84 mA/cm^2. The improvement is mainly achieved by steeper slope. Although both of the photoanodes have similar onset potential, about 1.1 V vs. RHE, wires array experiences faster current increase than flat substrate. This trend is also observed in 20 nm film on wires array and flat substrate.

Although wires fabrication changes the slope under the same iron-oxide film thickness, this observation may not be related to electrochemical charge transfer coefficient. In section 4.3.7, the slope changed according to iron-oxide thickness, but under identical light absorption and carriers generation. However, in wires case, there are no fundamental changes in solid and liquid junction structure. Rather, light absorption is improved by reduced reflection. Also, photogenerated carriers can easily travel to the silicon surface in wires array. Therefore, it is estimated that the carrier density which participates in chemical reaction are higher than that of flat substrate. This should contribute to improved photocurrent.

4.4.2 Improvement by ohmic contact

To eliminate parasitic loss from Schottky contact, a shallow n$^+$ back doping was made on silicon substrate. After the treatment, the sheet resistance dropped to 12~14 Ω/sq., which is comparable with metallic surface. Using this substrate, photoanodes were fabricated both in flat and wires configuration.

Figure 4.30(a) shows the photoresponse of n^+ doped silicon without iron-oxide. Obviously, there is no photoresponse, which means the treatment does not make any modification on the junction characteristic between silicon and electrolyte.

Figure 4.30(b) depicts all the measured photocurrents from photoanodes with different iron-oxide thickness and pH. Comparisons with the same samples except ohmic contact are illustrated in figure 4.30(c)~(f). The biggest improvements were made on thin iron-oxide film photoanodes. As shown in figure 4.30(c) and (d) of 5 minutes(10 nm) film, high photocurrent of 12.2 mA/cm^2(pH=13.8) and 4.34 mA/cm^2(pH=12) were recorded at zero overpotential(1.23 V vs. RHE), which exceeds any previous reports on photoanode current density.

Interesting observation is the case of 10 minutes(20 nm) films. In this case, no shift was observed when compared to Schottky contact(untreated) substrate. This was common both in pH=13.8 and 12. It is rather unexpected result since the Schottky barrier is universal regardless of the iron-oxide film thickness. One possible explanation is the contribution of Schottky barrier to overall losses. The photoelectrodes have intrinsic loss occurred by the carrier transport through iron-oxide film, and this increases with the film thickness. If we re-think figure 4.12, the gain by decreasing the iron-oxide film thickness is rapidly decaying beyond 5 minutes(10 nm) point.(Assuming the atmospheric pressure CVD process requires stabilization time, very short deposition like 1 or 3 minutes is likely thinner than 2 or 6 nm.) In fact, 5 minutes deposition sample has almost reached the maximum achievable limit. Consequently, in 5 minutes deposition sample, the loss by iron-oxide film transport is relatively small. Since most of the loss is coming from Schottky junction, the ohmic contact greatly improves the photoresponses. In contrast, iron-oxide transport loss may be so dominant in thicker film as to render the loss by Schottky barrier.
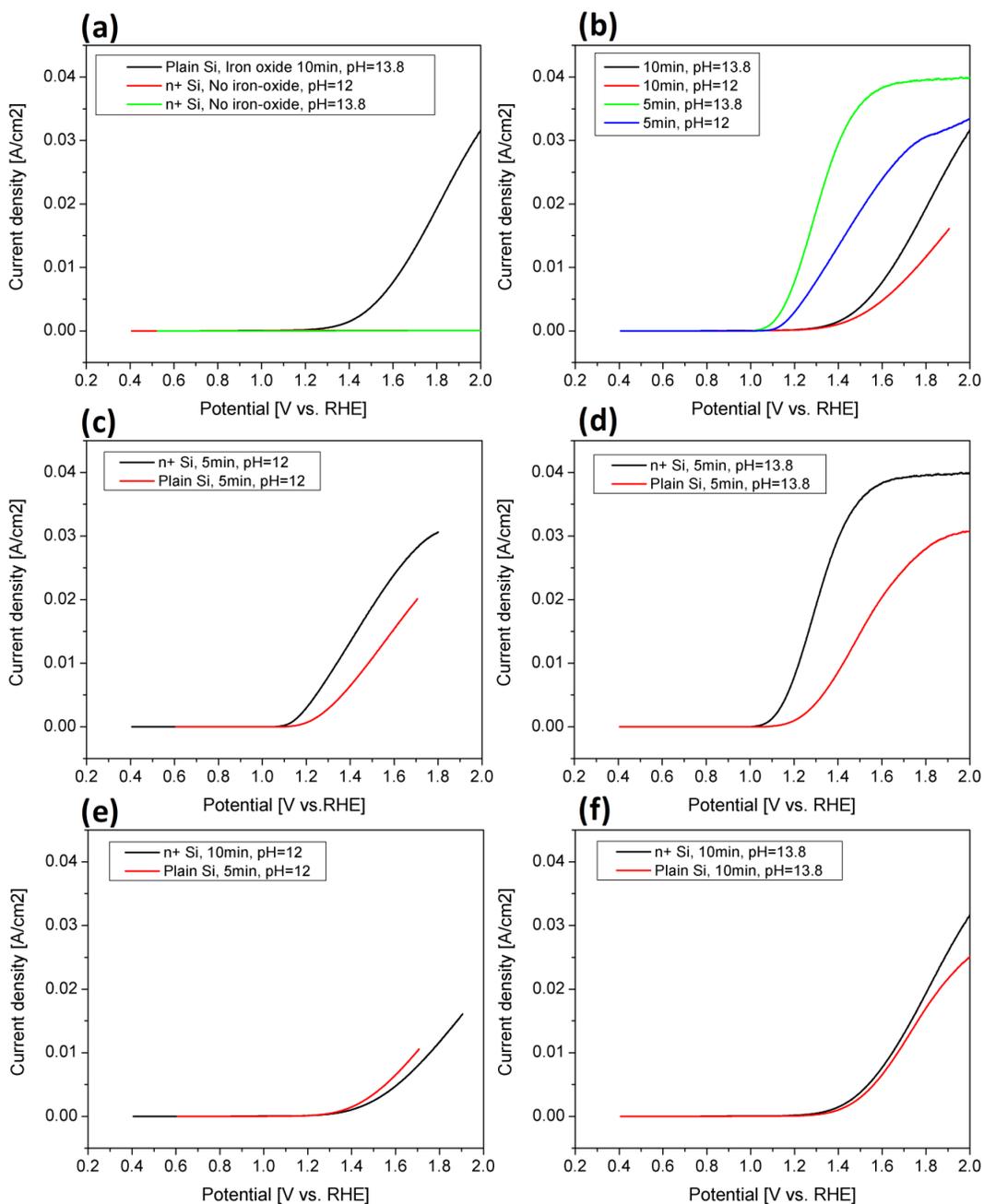
Figure 4.30 Photocurrents of flat substrate with ohmic contact. (a) comparison between n+ silicon substrate without iron-oxide film and plain silicon substrate with iron-oxide film, (b) photoresponses of n+ silicon based photoanodes at different pH and iron-oxide film thickness, (c)~(f) comparison of n+ silicon photoanodes with plain silicon photoanode, (c) and (d) 5 minutes iron-oxide deposition samples measured at pH=12 and 13.8, (e) and (f) 10 minutes iron-oxide deposition samples measured at pH=12 and 13.8.

Finally, the n$^+$ ohmic contact substrate was applied to silicon wires array fabrication, followed by iron-oxide film deposition. Figure 4.31 shows the results of 10 minutes film deposition at pH=12 and 13.8. At zero overpotential, photocurrents of 4.81 mA/cm^2 and 17.27 mA/cm^2 were achieved.
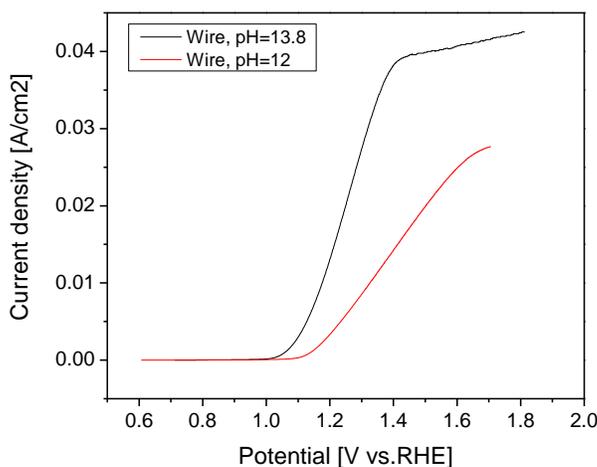
Figure 4.31 Photocurrents of silicon wire photoanodes with 10 nm thick iron-oxide films.

4.4.3 Quantitative evaluation of presented system

It was shown that iron-oxide catalyzed silicon photoanode possesses a high photocurrent generation potential. Since our device is based on half-cell reaction which is lacking full photocell bias for cathode reaction, it is rather difficult to quantitatively compare the overall performance with previous reports. The difference of photovoltaic cells, which result in different circuit voltages and cathode compensation requirements, hinders the standardization.

Therefore, the component performances, electrolysis efficiency and zero overpotential current density, will be first evaluated and compared with relevant researches. Then, the solar-to-chemical conversion efficiency will be calculated under idealized conditions. Finally, based on this conversion efficiency, the production cost will be estimated.

4.4.3.1 Electrolysis efficiency comparison with ruthenium-oxide

The total conversion efficiency is determined by photocell and electrolysis performance. Major improvement in our structure lies in the electrolysis process at the photoanode-electrolyte interface. Figure 4.32(a)[65, 149] describes the potential variation with galvanostatic current density at various

hydrogen and oxygen electrodes in 1M $HClO_4$. The electrodes include RuO_2, which is one of the best electrolysis catalyst, and platinum. In figure 4.32(b), our silicon photoanodes responses with n^+ doping and flat or wire configurations are illustrated. These two plots are drawn into the same scale, and merged as shown in figure 4.32(c).
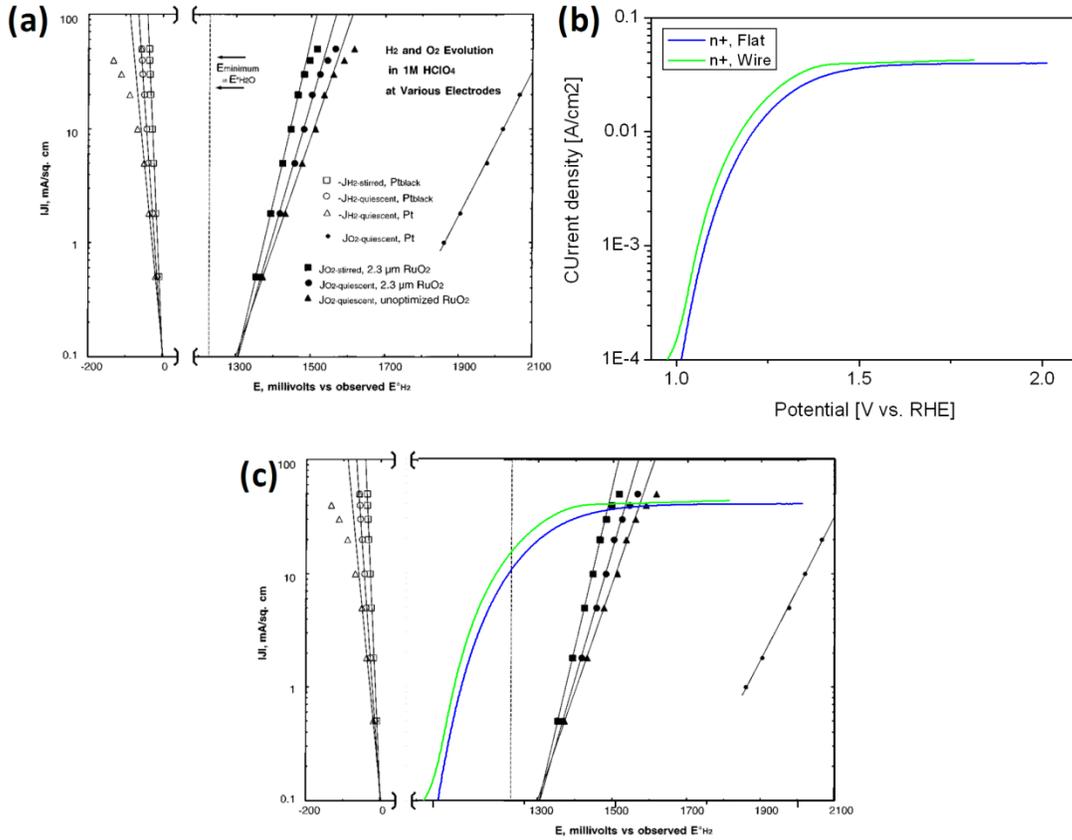
Figure 4.32 (a) Potential variation with galvanostatic current density at various hydrogen or oxygen electrodes in 1 M $HClO_4$, (b) iron-oxide catalyzed silicon photoanode photoresponses with n^+ doping and flat(5 minutes iron oxide deposition) or wire(10 minutes deposition) configuration at pH=13.8, (c) scaled and merged plot of (a) and (b).

Electrolysis efficiency can be expressed as following equation.

$$\eta_{electrolysis} = \frac{E_{H_2O}}{E_{O_2} - E_{H_2}}$$

Equation 4.6 Electrolysis efficiency

Since $E_{H_2O} = 1.23$ V, the denominator of equation 4.6 is the width of figure 4.32(c) plots. Assuming common cathode, the electrolysis efficiency of iron-oxide catalyzed silicon photoanode exceeds that of RuO$_2$ as much as 29 %(at 1 mA/cm^2) and 24%(at 10 mA/cm^2). Of course, our silicon photoanode eventually needs tandem cell to compensate cathode potential, which will lower the 'only-silicon' anode response to some extent. Therefore, above calculation is upper limit of performance improvement we can expect.

4.4.3.2   Zero overpotential current density comparison with iron-oxide photoanode

Iron-oxide photoanode is a good comparison example because the required cathode potential compensation is very similar to silicon as shown in figure 4.25(about 0.2 ~ 0.4 V). Given the same infrastructure requirement, it would be meaningful to compare zero overpotential current density between these two materials.

According to report by Grätzel and coworkers,[57] iridium-oxide decorated iron-oxide photoanode produces 3.01 mA/cm^2 current density at 1.23 V vs. RHE while our flat configuration iron-oxide/silicon photoanode produces 12.2 mA/cm^2. Nominally, our device shows 405 % of iron-oxide photocurrent. However, iron-oxide has about twice wider band gap than silicon, meaning roughly twice higher voltage output is expected. Therefore, in terms of output power, iron-oxide catalyzed silicon photoanode possess about 203 % of performance, or 103 % advantage over iron-oxide photoanode.

Iron-oxide photoanode has more flexibility in construction since wide range of wavelength spectrum(> 560 nm) is still available for narrower band gap semiconductors of tandem cell. Nevertheless, above calculation shows higher fill factor of silicon device compared to oxide semiconductor.

4.4.3.3   Zero overpotential current density comparison with silicon photoanode

The most analogous structure to our photoanode is electrocatalyst deposited silicon photoelectrode system. However, most of these structures have metallic interlayer between water and silicon, either as current collecting layer or metallic catalyst. As pointed in section 4.3.4, since the Fermi level of metal is pinned, favorable upward band bending like section 4.3.6 is hard to expect in general materials set. For example, two researches of silicon photoanode have been reported using cobalt phosphate(Co-Pi) catalyst on silicon solar cells.[66, 67] In spite of good catalytic functionality of Co-Pi, the zero overpotential current density is much smaller than our result.

In this respect, a recent report by McIntyre and coworkers[150] with iridium catalyzed silicon photoanode provides a very close comparison with our iron-oxide catalyzed silicon photoanode due to structural and electronic similarities. Since iridium is a conductive metal, silicon cannot communicate with water directly. However, the intrinsic electronic properties of iridium make fairly analogous situation. First, barrier height between n-type silicon and iridium(about 0.9 eV[151]) can be compared with 0.7~0.8 V built-in potential of silicon/iron-oxide photoanode. Also, Fermi level of iridium(-5.2 eV vs. vacuum) is similar to silicon valence band edge position(-5 eV vs. vacuum). Due to the electronic similarity, the performance likely relies on catalytic functionality.

At NaOH 1 M condition, about 9 mA/cm^2 was recorded. Considering our 12.2 mA/cm^2 result of flat substrate at the same condition, iron-oxide/silicon photoanode have about 36 % advantage. Note that McIntyre group reported high performance at acidic condition, which implies that iridium favors acidic environment(which is incompatible with iron-oxide, see figure 2.1) while iron-oxide favors basic environment as shown in figure 4.16. Again, iron-oxide has superior advantage in practical application over iridium which is the rarest element in earth crust.

4.4.3.4　Overall solar-to-chemical conversion efficiency

Since present device is based on half cell reaction and the cathode potential is supplemented by potentiostat, explicit solar-to-chemical conversion efficiency is hard to calculate. However, by abrupt simplifications and assumptions, reasonable metric will be calculated in this section.

First assumption is that cathode reaction needs no overpotential, that is, 0 V vs. RHE. It is known that many high efficiency cathode can be operated at less than 0.1 V of overpotential. Therefore, this assumption may not significantly violate the real situation.

Second assumption is that the Faraday efficiency, which means the conversion efficiency between charges and electrochemical species, is 100 % for both anode and cathode reactions.

The maximum photocurrent of crystalline silicon with 1.1 eV band gap is known about 43 mA/cm^2 under 1 sun irradiation condition.[150] From the theoretical calculation by Shockley and Queisser,[152] the ultimate solar-to-electric conversion efficiency is 29 % for 1.1 eV band gap semiconductor. Therefore, when 43 mA/cm^2 is harvested from photovoltaic device, the conversion efficiency corresponds to 29 %. In our photoelectrochemical process, the ideal current collection condition is when the electrode potential is in the theoretical limit, that is, 1.23 V vs. RHE. The ratio between current density at 1.23 V vs. RHE and 43 mA/cm^2 implies the portion of charges transferred to electrochemical reaction among all available

carriers generated by incident sun light. In summary, equation 4.7 deduces the solar-to-chemical conversion efficiency based on above logics.

$$\eta = \frac{\text{Current density at 1.23 V vs. RHE}}{43\,\text{mA/cm}^2} \times 29\,\%$$

Equation 4.7 Solar-to-chemical conversion efficiency in silicon photoanode for water oxidation reaction.

The maximum current density obtained from present devices is 17.27 mA/cm^2 at 1.23 V vs. RHE on photoanode with wires array and n$^+$ shallow doping. In this case, the calculated efficiency is 11.6 %.

4.4.3.5   Estimated hydrogen production cost

Compared to photovoltaic systems designed for electricity harvesting, photoelectrochemical(PEC) systems require further infrastructures enabling water circulation and gas collection. Therefore, the capital structure is typically more complex and expensive than simple photovoltaic systems. Based on a research[153] coordinated by U.S. Department of Energy, hydrogen production cost of 10.36 $/kg was estimated under following copper indium gallium selenide(CIGS) planar photovoltaic system:

10 years of transparent window/PEC cell life

CIGS/Ge cell

PEC cell cost about 153 $/m^2

10% solar-to-hydrogen efficiency

All relevant liquid/gas treatment subcomponents

Facility capacity of 1000 kg hydrogen per day

Note that this calculation is based on idealized and hypothetic system. Although CIGS photovoltaic system has been proved, its photoelectrochemical operation has not yet demonstrated. Therefore above calculation excludes electrochemical feasibility. On the contrary, our metric is based on experimental observations, which may provide more realistic prediction.

Using the calculated efficiency 11.6 % of presented iron-oxide/silicon photoelectrode, the hydrogen production cost is estimated about 8.93 $/kg. This assumes that the production cost of the two different cells, iron-oxide/silicon and CIGS/Ge, are identical.

If mass specific energy(hydrogen:gasoline = 2.8:1) and gasoline density(0.7 kg/L) are used to make a direct comparison of gasoline equivalent price, 1 kg hydrogen corresponds to 4 L or 1.06 gallon of gasoline. This is about 2~3 times higher than gasoline retail price in U.S.(about 4 $/gallon) as of mid 2011 and U.S. DOE's hydrogen price goal, 2~3 $/kg.[154] Future improvement of conversion efficiency as well as materials processing will potentially reduce this predicted hydrogen production cost.

4.5 Practical issues in operation

4.5.1 Oxygen evolution verification

We showed a high photocurrent evolution from our iron-oxide catalyzed silicon photoanode. Ideally, it is necessary to calculate the Faradaic efficiency by measuring the amount of evolved oxygen and hydrogen. However, due to the limited facilities, it was impossible to quantify. However, at least, it is desirable to verify that the reaction is producing oxygen and hydrogen. Therefore, we first provide indirect proofs that the current are not being evolved by other possible side reactions including etching or oxidation of electrode. Also, qualitative measurement of evolved gas by gas chromatography will be presented.

4.5.1.1   Silicon oxidation

Silicon may experience anodic oxidation under anodic bias. However, our operation potential is merely 1~2 V vs. cathode potential, which is much lower than practical anodic oxidation.[155] Also, silicon oxidation makes an insulating layer(silicon hydroxide) which passivates the surface. Although this oxide might be dissolved in chemical reaction,[156] corresponding current is very small. Therefore, our continuous high current operation disproves the anodic oxidation of silicon.

4.5.1.2   Silicon etching

Bare silicon had no photoreactivity(figure 4.33(a)). Also, (111) silicon and (100) silicon with iron oxide film showed no difference in performance(figure 4.33(b)). Considering (111) silicon has 2~3 order slower etching rate than (100) silicon, the same photocurrent cannot be sustained by silicon etching.

Finally, let's assume silicon is dissolved by the Si $\rightarrow$ Si^{4+} + 4e$^-$ reaction. The surface area of the silicon wires array with 1 µm diameter, 10 µm height and 2 µm pitch is 9 times the area of flat substrate.

Therefore, for unit cell(1cm by 1cm substrate), it is 9 cm^2. If this surface is etched as much as 500 nm deep, the wires must be completely gone. Corresponding silicon volume($4.5*10^{-4}$ cm^3) can be converted to charge(14.4 coulomb) using density(2.33 g/cm^3) and molecular weight(28 g/mol). If current density is 5 mA/cm^2, it takes 2885 seconds(48 minutes).
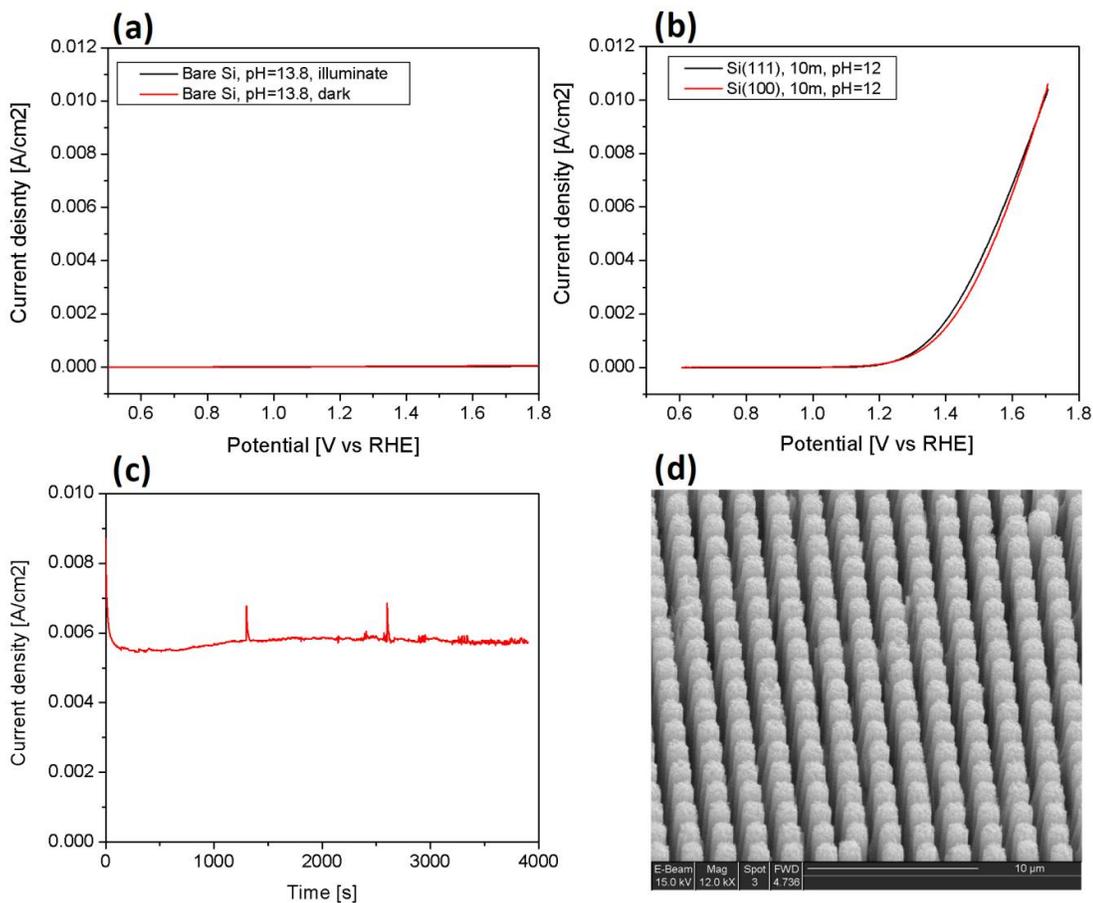
Figure 4.33 Silicon etching disproof. (a) bare silicon photoresponse, (b) photoresponse comparison between Si(111) and Si(100) samples, (c) current vs. time curve for silicon wires array photoanode, (d) SEM image of silicon wires array after the operation of (c).

Figure 4.33(c) and (d) show the results after 65 minutes operation at 5.5 mA/cm^2. The wires array showed no physical damage at all as illustrated in Figure 4.33(d). Note that in Figure 4.33(c), the peaks are artifacts when new measurement cycles starts at every 1300 seconds.

4.5.1.3 Iron-oxide etching

Iron-oxide etching is mediated by proton and chlorine ions, which is the reason of high-pH stability.[157] Therefore, it is assumed that our high pH and chlorine-free operation condition may not harm the iron-oxide film. This was experimentally proven in the similar manner to silicon etching calculation. We know iron oxide film thickness, therefore are able to calculate the atomic population and corresponding charge. Considering 20 nm Fe_2O_3 film experiences Fe $\rightarrow$ Fe^{3+} + 3e$^-$ dissolution, 10 mA/cm^2 current can be maintained only for 1.3 seconds as calculated in figure 4.34. Our operating time was orders of magnitude longer than 1.3 seconds.
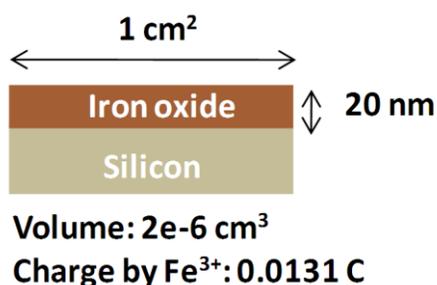
Figure 4.34 Iron-oxide etching disproof.

4.5.1.4 Gas chromatography

Figure 4.35 shows the picture of gas evolution measurement setup. The electrochemical cell is H-shape quartz tube with separation frit, which is made of porous glass coated with Nafion for selective permeation of proton. One side of the cell contains Ag/AgCl reference electrode and platinum mesh cathode, and the other side has our photoanode. The photoanode is prepared from plain(no n$^+$ back doping) flat silicon substrate with 10 minutes iron-oxide deposition. At each side of the cell, 100 ml of pH=11 electrolyte was filled. Electrode potential was controlled by potentiostat(AutoLab PGSTAT128N, Metrohm), and 300 W Xe Arc lamp(Model 66902, Thermo Oriel) was used for light source.

The experiment was conducted in this order. First, all electrodes and electrolyte were placed in each cell, and the cells were tightly encapsulated by rubber septum cap. Under dark condition without bias, both cells were purged by argon for two hours. After purging, the gas content of each cell was captured by glass syringe, and analyzed by gas chromatography tool(7890A, Agilent). Then, with the light on, 0.6 V vs. Ag/AgCl potential was applied for two hours. Measured current density was 1.2 mA/cm^2. Upon completion, the gas contents were analyzed again, and compared with the initial data.
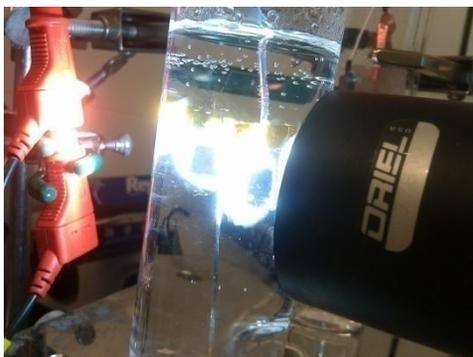
Figure 4.35 Gas chromatography setup.
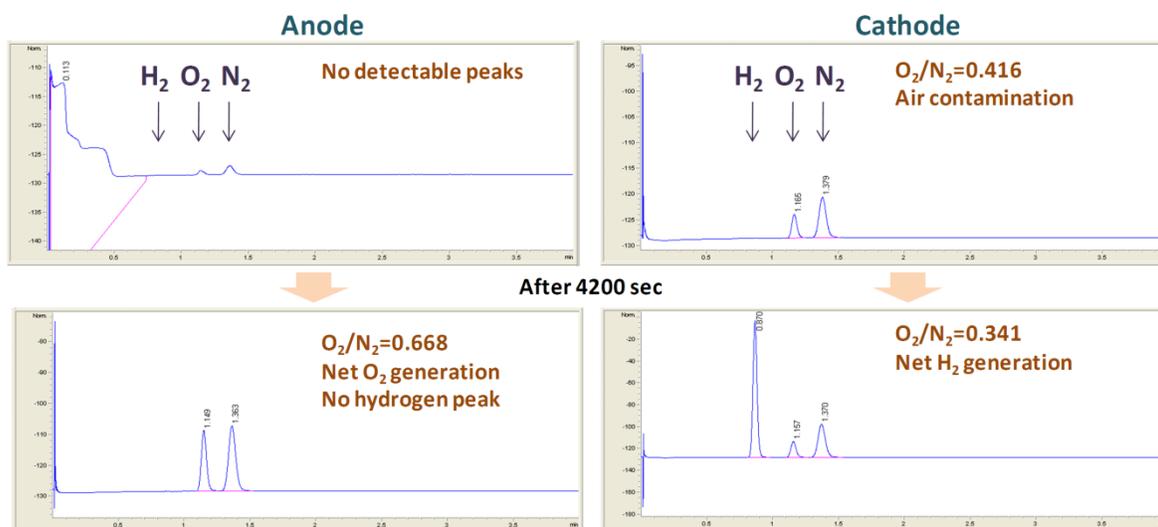
Figure 4.36 Gas evolution before and after the experiment.

Figure 4.36 shows the analyzed gas contents before and after the operation. Due to the contamination by small leakage or during transport, quantitative comparison was impossible.(See the N_2 contents, which is not supposed to be inside.) However, seeing the initial and final results of cathode, it is estimated that the $O_2/N_2 = 0.3\sim0.4$ is the ratio of ambient air. Considering this background contamination, the final result of anode shows net oxygen generation since the portion of oxygen becomes higher than ambient air. Hydrogen evolution in cathode is obvious from the plot.

4.5.2 Long term operation

For practical application of inorganic photoelectrode, long term stability must be verified. Since DC sweep only takes a few minutes, longer operation was tested with predetermined potential for hours.

114

Three flat photoanodes and one wires array photoanode(all 10 minutes iron-oxide deposition) were operated with different electrode potentials for 3900 seconds at pH=12, and the current vs. time curves are plotted in figure 4.37.
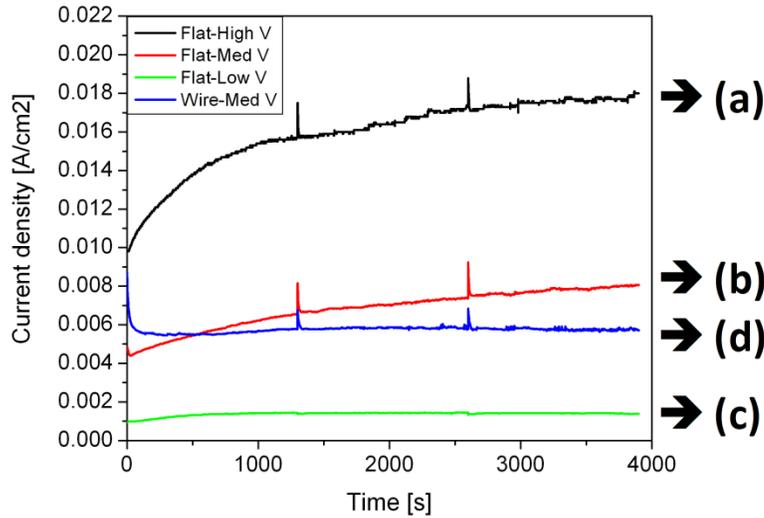
Figure 4.37 Stability comparison of 3900 seconds operations. (a)~(c) 10 minute iron-oxide on flat, plain(no n$^+$ contact) silicon devices with different potential, (d) 10 minute iron-oxide on wires array, plain silicon device.

Notable characteristic of the profiles is the gradual increase of photocurrent in flat silicon photoanodes. It is still unclear why the current increase happens. However, from this observation, low current density is less affected by this unknown instability. The highest potential sample(figure 4.37(a)) shows initial current of 10 mA/cm^2 and reaches ~15 mA/cm^2 after 3900 seconds, but is still in transient process. However, the lowest potential sample(figure 4.37(c)) soon reaches steady state current density of ~1.4 mA/cm^2. Initially, this current increase was thought as a process of stabilization. However, in such a case, samples with large current density should reach the steady state earlier than samples with small current density. In this respect, this current increase is likely a detrimental process.

One possible explanation is a kind of electromigration. From our investigation, iron-oxide is not chemically etched in our operational environment. However, when the current density is large, physical detachment of the film could happen. Electromigration is the analogical phenomenon in solid state electronics, in which high current repeatedly stimulates atoms by momentum and eventually induces physical migration. If similar process may happen in iron-oxide film, the surface atoms are gradually detached and the film gets thinner. Since thin film performs better, the current may increase to some extent.

If current density decreases, the migration will be suppressed. In other words, very large surface area, subsequently very low current density per unit film area should be beneficial. Wires array or other textured surface satisfies this condition. As seen in figure 4.37(d) again, photoanode fabricated on silicon wires array shows stable operation throughout the operation window even though its current density is high. For this sample, the actual current density per film area(0.6 mA/cm^2 film) is less than half of that of the lowest current flat film.(1.4 mA/cm^2 film) That is, surface texturing helps not only improved photoresponse but also operation stability.

The films on flat substrates cannot be thinned indefinitely. It is more reasonable to think that the film will be delaminated if the thickness reaches certain critical value. To test this assumption, flat silicon photoanodes with 5 minutes(10 nm) iron-oxide film were prepared and operated for a long time until obvious failure is observed. Figure 4.38 shows current vs. time plot of one of the samples.
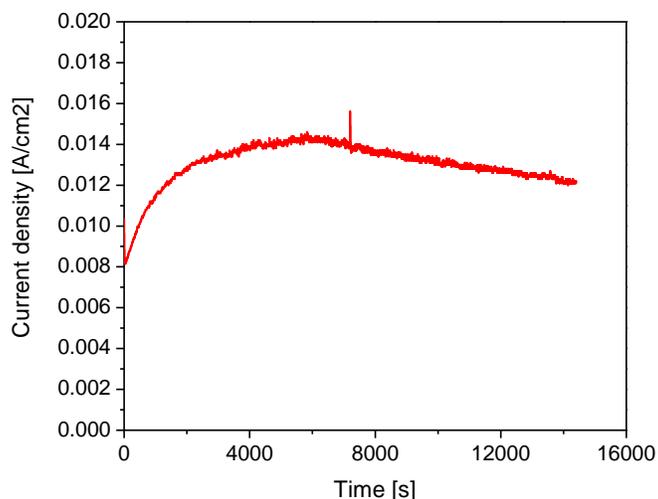
Figure 4.38 4 hours operation at pH=12.

The current reached maximum at about 6000 second point, then started to decay gradually. Test was continued for four hours, and the sample was investigated. However, no physical damages were found from this sample.
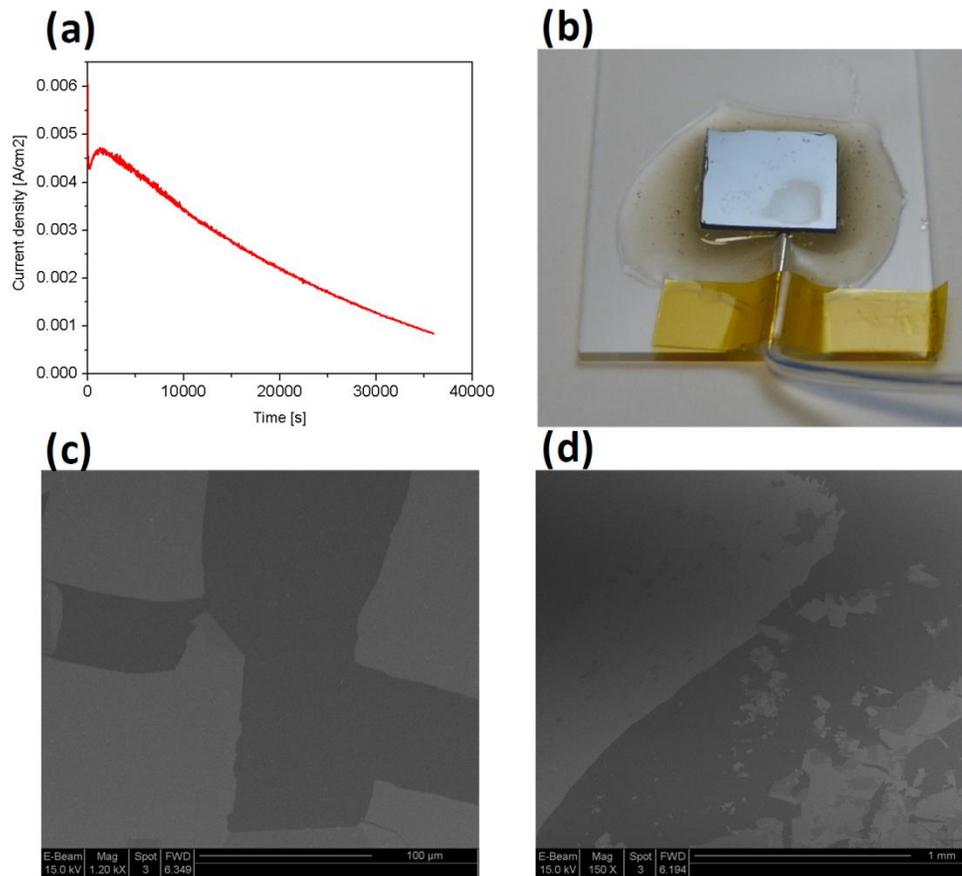
Figure 4.39 10 hours operation, failure mode. (a) current vs. time curve, (b) visual damage, (c) and (d) SEM images of (b).

Figure 4.39 is the result of another sample. The current maximum was reached at about 2000 seconds. However, to induce prominent damage, the operation condition was maintained for 36000 seconds(10 hours). At this point, the current dropped to about 20 % of the maximum value. This time, the damage of the film was visually observable. Electron microscope images of figure 4.39(c) and (d) clearly describes that film delamination occurred in this sample.

The two samples of figure 4.38 and figure 4.39 show different critical point. This randomness was still found in another trial, too. It is believed that the delamination point depends on the adhesion strength of the iron-oxide film and silicon substrate. There are many factors which affect the adhesion. For example, if silicon substrate has barrier oxide under the iron-oxide film, the adhesion is significantly compromised. Although HF etching was conducted before film deposition, there were time gaps between HF etching and film deposition from tens of minutes to hours, which varies among samples. Factors like this may affect the adhesion, resulting in inconsistency of critical points.

Chapter 5   Concluding remarks

5.1 Conclusion of iron-oxide catalyzed silicon photoanode

Currently, the search for alternative energy sources is being intensified. However, in contrast to electricity generation, there is no leading answer for renewable chemical energy. We suggested that hydrogen deserves to be a potential renewable chemical energy source not only for the value of pure form like burning gas or fuel cell, but also for core ingredient of artificial hydrocarbon synthesis. This can be justified only when mass production of hydrogen becomes affordable. Our search for high performance photoelectrode system started to meet this requirement and provide a viable option. Although inorganic photoelectrochemical system is known to be better option than biological production,[6] its performance still needs a lot of improvements. For this purpose, we explored novel materials set and structures, silicon photoanode catalyzed by iron-oxide thin film to efficiently split water molecules into oxygen and hydrogen.

Thin iron-oxide film was deposited on silicon substrate by low temperature atmospheric pressure CVD to catalyze oxygen evolution reaction. When iron-oxide film was sufficiently thin, around 10 nm or less, otherwise nonresponsive silicon photoanode showed a high photocurrent at a decent overpotential. Parametric studies revealed that the photoresponses become effective when (1) iron-oxide film is thin, (2) titanium content is high and (3) operation pH is high. From further analytical investigations, it was learned that photocarriers are solely generated by silicon while the role of iron-oxide is limited to catalyst. The catalytic functionality of standalone iron-oxide is fairly good, but not exceptionally outstanding. However, the performance is greatly boosted when combined with semiconducting silicon substrate. The reason is believed that iron-oxide can catalyze silicon surface without disturbing favorable upward band bending nature of silicon at the electrolyte junction.

Since silicon became the performance-determining factor of our photoelectrode, we adopted silicon microfabrication techniques including ohmic contact formation on the silicon backside and vertical wires array fabrication. By these measures, the onset potentials were decreased and the current-potential slope became steeper, resulting in high current density as high as 17 mA/cm^2 at zero overpotential. Extended time operation revealed oxygen evolution, but also film delamination issue. However, the film stability is believed to be an engineering problem in which practical solutions are being suggested.

Through this research, we made four notable contributions.

1. The possibility of silicon

Silicon has been the most popular solar cell material. Although silicon photocathode has been conceptually demonstrated, silicon photoanode has not been successful due to the energy band mismatch. In this research, it was shown that silicon can be used for photoanode with the help of appropriate catalyst and pH control. Along with the proven cost-to-performance metric of silicon, this allows the use of vast knowledge of silicon, which precipitates future related researches.

2. Inexpensive materials set

The list of all the materials used in this research includes silicon, iron and titanium which are the most abundant and affordable materials in earth crust(figure 5.1). This will be further benefitted by the intense researches on low cost silicon production.
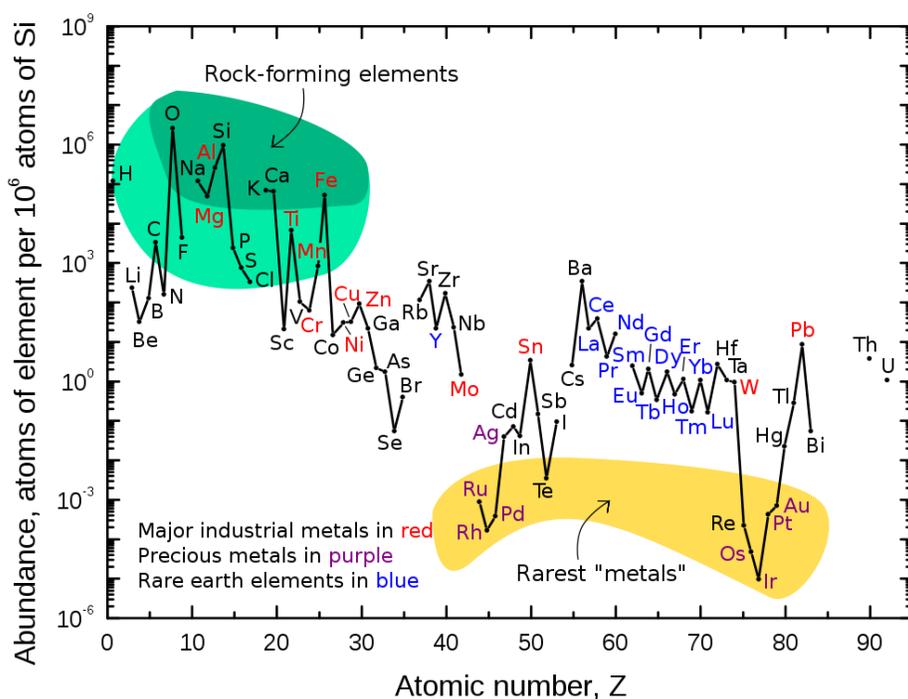
Figure 5.1 Abundance of elements in earth's crust.(from Wikipedia.org, http://en.wikipedia.org/wiki/Abundance_of_elements_in_Earth%27s_crust, last verified on June 16, 2011)

3. High performance

This research achieved high photocurrent at anode reaction at zero overpotential. Although the open circuit voltage would be low due to narrow band gap of silicon, the current density of 17 mA/cm^2 is at least 5 to 10 times larger than currently popular photoanodes using metal oxide semiconductors with 2~3

119

eV band gap. This should present higher fill factor than these low conversion efficiency semiconductors. Even when compared to similar photoanodes using silicon but different catalysts and constructions, present devices' performance surpassed most of the previous results.

4. Theoretical background for the search of further improved system

An energy band model was suggested based on theoretical and experimental analysis. Silicon has ideal band edge alignment in our operation conditions since oxygen evolution potential is aligned with valence band edge. Also, semiconducting catalyst(iron-oxide) plays an effective catalytic function. From this point, plenty of variations are possible: different catalysts, different substrates, other substrate treatments and so on. We established a platform from which further improved systems could be developed.

5.2 Suggested future works

Through this research, a few future works were identified. In this section, these points will be listed, and suggested directions will be presented, too.

5.2.1 Silicon microstructure optimization

In this research, simple vertical silicon wires array was tried. Recent studies revealed that the performance of silicon wires photovoltaic device can be further improved by more precise manipulations of the structure. For example, particle decoration and array configurations could be facilitated to enhance light harvesting capability.[82] Simple strategies including wires length adjustment and light incidence angle modification can be adopted for better silicon efficiency.

Alternative method to wires array is roughened surface. Wires array fabrication needs several steps of processes which raise the overall cost. As a simpler measure, roughened surface with random bumps are usually adopted to reduce light reflection in commercial flat silicon solar cell. This will be easily applied to photoelectrode fabrication, too.

5.2.2 Silicon protection

Although our silicon photoanode showed fairly acceptable stability in our operation window, silicon will be eventually etched in highly basic solution. Using etch-resistive crystal surface like Si(111) might

be a simple solution extending the life time effectively 2~3 orders than Si(100) substrate without sacrificing the performance as in section 4.2.4.

Another method is active protection layer of silicon surface. About this issue, a literature[158] reported that surface alkylation gives a good stability on silicon surface for a long time. Our thin polycrystalline film is thought to have small voids on silicon surface, and this exposed silicon would be attacked first. Therefore, surface treatment like methylation or hydrophobic coating of the bottom area could elongate the lifetime.

Finding out protective film of entire device would be challenging, but most effective method. Recently, very thin silicon oxide and titanium oxide films were proved to protect silicon photoanode with iridium catalyst for more than 24 hours.[150]

5.2.3 Iron-oxide film stabilization

In our observation, iron-oxide film experiences a gradual detachment from the host surface. Our suspicion comes to the atomic detachment induced by current momentum, similar phenomenon to electromigration in solid state materials. Easiest resolution is to decrease current density per film area as shown in our wires array experiment. The surface area can be more increased by corrugate film surface like dendrite structure.[51]

It is also necessary to add the film more mechanical strength in molecular scale. Sintering is one of the widely used methods for this purpose. Although our annealing failed to reproduce catalytic functionality, this is believed to be a result of insufficient optimization. Addition of other atomic contents which promote film stability is another measure worth considering.

Finally, the adhesion between iron-oxide film and silicon determines the delamination point. Again, complete removal of native oxide on silicon should be required to prevent weak adhesion. Another possibility is to introduce appropriate adhesion promoting interlayer between silicon and iron-oxide.

5.2.4 Cathode potential compensation

The photoanode fabricated in this research works on half cell reaction. Since the band gap of silicon is 1.12 eV, which is smaller than water redox potential difference,(1.23 V) we do need potential compensation for cathode reaction.

Already, there are models for this kind of architecture,[159, 160] as in figure 5.2. In summary, a photocell or photocathode is stacked with our photoanode and the energy bands of this entire cell straddle the water

redox potential. Therefore, the cathode electrode must have band alignment for hydrogen evolution. In contrast to anode, many cathodes have been developed with high performance, which exceeds the current density of our photoanode at zero overpotential.

This stacked photodevice can be located either upstream or downstream of our photoanode. Considering our device uses narrow band gap material(silicon), it is desirable to install the wide band gap cathode stack upstream of our device. The conceptual design is drawn in figure 5.2(c).
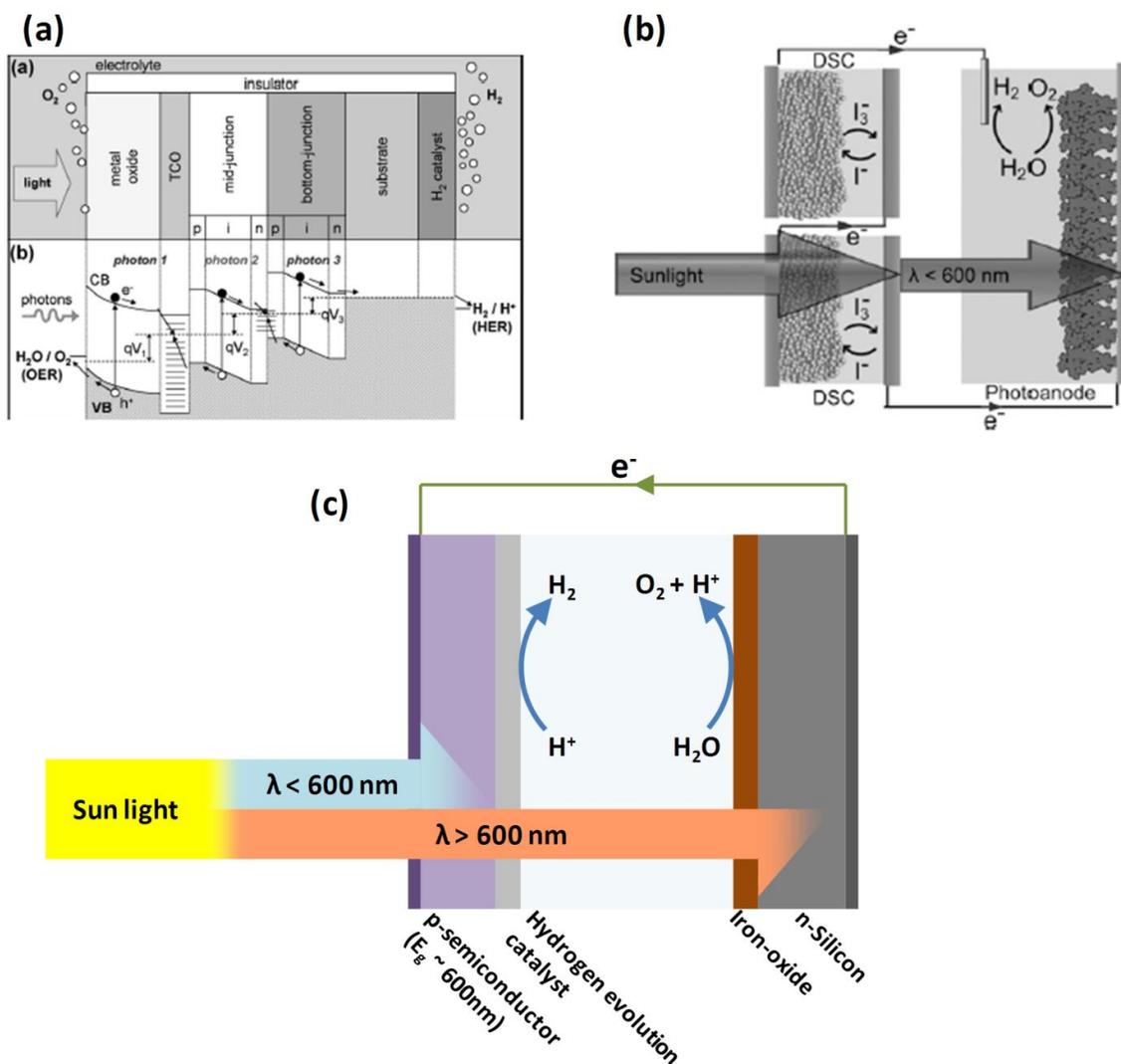
Figure 5.2 Cathode potential compensated full cell devices. (a) multijunction photoelectrode with semiconductor-liquid junction, (b) dye sensitized solar cell supported photoanode, (c) suggested model.

5.2.5 New photoanode materials search

In this research, single crystal silicon was used as the light absorption layer. Although crystalline silicon is the dominant material for solar cell, silicon accounts for the majority of cell cost and the development of low cost silicon wafer alternatives is a practical challenge. Analogously to solar cell, the crystalline silicon is likely the issue in photoanode. Therefore, it is desirable to search alternative photoanode materials with competitive cost.

Silicon photoanode produces high photocurrent due to the large built-in potential in semiconductor to liquid junction. This comes from the matching position of semiconductor valence band and oxygen evolution potential. Therefore, semiconductors with valence band near 1.23 V vs. RHE would be appropriate. In this standpoint, it is believed that amorphous silicon(a-Si) and cuprous oxide(Cu_2O)[60] might be good candidates.

5.2.6 New catalysts search

Although iron-oxide showed a good catalytic functionality in our experiment, it is not believed 'the best' catalyst available. From researches,[51, 57, 58, 73] when iron-oxide was decorated or compounded with certain components, the performance improved, occasionally, greatly. We have limitation that the catalyst must be semiconducting or nearly insulating with low doping density, but not too low to transfer the carriers. Since there are many transition metal oxides with semiconducting properties, it is very probable that catalyst with better activity could be found, especially, in the group of cobalt, nickel and iridium oxides.

Chapter 6   Appendix

6.1 Light absorption calculation

To calculate light absorption by formulas in equation 4.2, refractive index values must be obtained first.

Iron-oxide: reference[161]

Silicon: Filmetrics refractive index data base (http://www.filmetrics.com/refractive-index-database/Si/Silicon, last verified on June 16, 2011)

Water: reference[162]

For calculation, the data were appropriately fitted and plotted in figure 6.1.
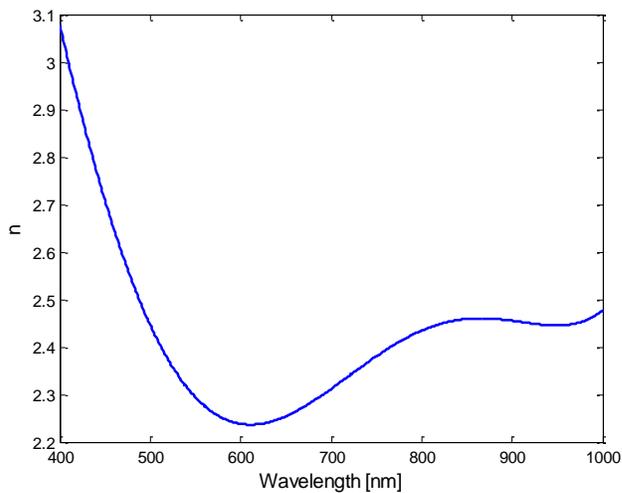
(a) iron-oxide n

$n = p1*x^5 + p2*x^4 + p3*x^3 + p4*x^2 + p5*x + p6$

p1 = 1.432*10^{-13}
p2 = 4.671*10^{-10}
p3 = 5.671*10^{-7}
p4 = -3.067*10^{-4}
p5 = 6.605*10^{-2}
p6 = -7.245*10^{-2}
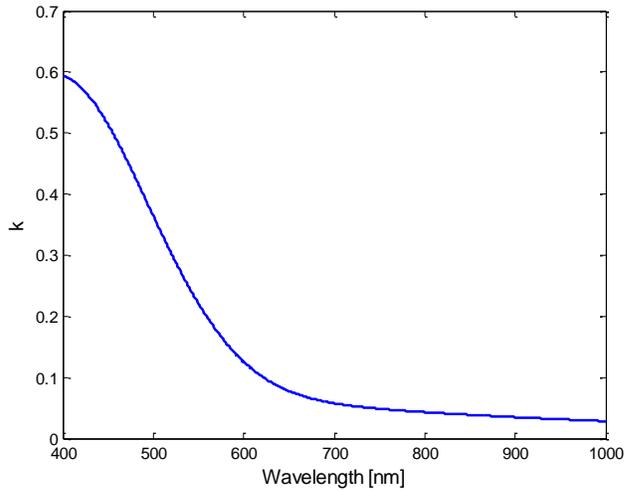
(b) iron-oxide k

k = p1*exp[-{(x-p2)/p3}^{2}] + p4*exp[-{(x-p5)/p6}^{2}]

p1 = 0.4974
p2 = 394
p3 = 142
p4 = $6.735*10^{11}$
p5 = $-2.841*10^4$
p6 = 5299
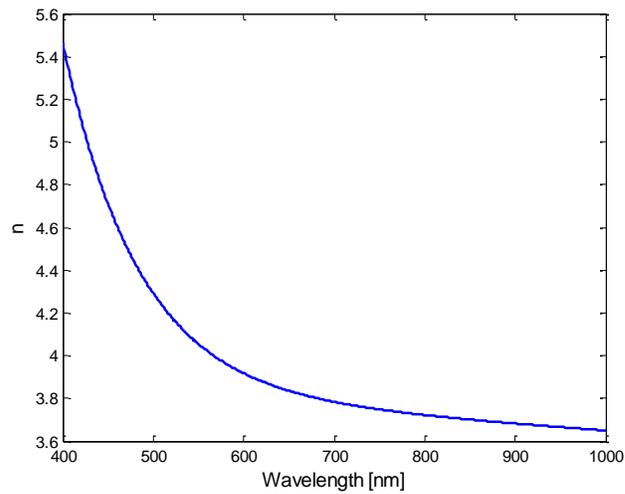
(c) silicon n

n = p1*exp(p2*x) + p3*exp (p4*x)

p1 = 198
p2 = -0.012
p3 = 3.96
p4 = $-8.192*10^{-5}$
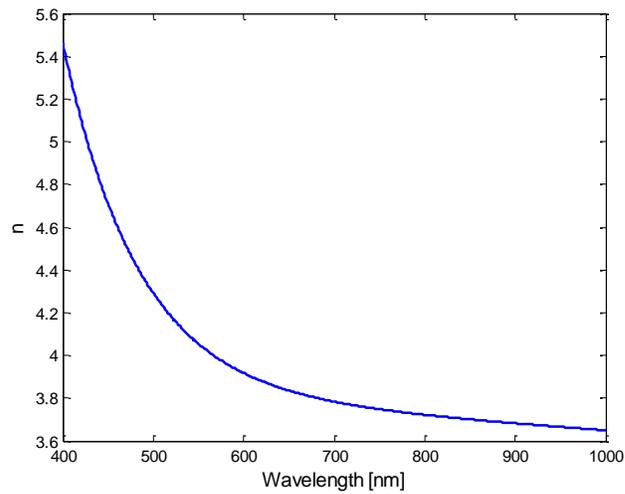
(d) water n

n = p1*x^6 + p2*x^5 + p3*x^4 + p4*x^3 + p5*x^2 + p6*x + p7

p1 = $1.951*10^{-18}$
p2 = $-9.029*10^{-15}$
p3 = $1.737*10^{-11}$
p4 = $-1.785*10^{-8}$
p5 = $1.04*10^{-5}$
p6 = $-3.297*10^{-3}$
p7 = 1.821

Figure 6.1 Fitted refractive index.

Using this information, the light absorptance was calculated by following MATLAB codes.

```
for u=1:300
x=399+u; %wavelength lambda

%Water
p1=1.951e-018;
p2=-9.029e-015;
p3=1.737e-011;
p4=-1.785e-008;
p5=1.04e-005;
p6=-0.003297;
p7=1.821;
ni=p1*x^6+p2*x^5+p3*x^4+p4*x^3+p5*x^2+p6*x+p7;

%Iron oxide
p11=1.432e-013;
p12=-4.671e-010;
p13=5.671e-007;
p14=-0.0003067;
p15=0.06605;
p16=-0.07245;
n=p11*x^5+p12*x^4+p13*x^3+p14*x^2+p15*x+p16;

p21=0.4974;
p22=394;
p23=142;
p24=6.735e+011;
p25=-2.841e+004;
p26=5299;
k=p21*exp(-((x-p22)/p23)^2) + p24*exp(-((x-p25)/p26)^2);

%Silicon
p31=198;
p32=-0.012;
p33=3.96;
p34=-8.192e-005;
ns=p31*exp(p32*x)+p33*exp(p34*x);

%definitions
d=20; %film thickness(nm)
q0=2*3.1416/x;
del=q0*d;
```

```
m=n+k*i;
ri=(ni-m)/(ni+m);
lambda(u)=x;
gamma=exp(i*m*del);

%iron oxide/silicon
rs=(ns-m)/(ns+m);
rbar=(ri-rs*(abs(gamma))^2)/(1-ri*rs*(abs(gamma))^2);
tbar=(1+ri)*(1-rs)*gamma*exp(-i*ns*del)/(1-ri*rs*(abs(gamma)^2));
A(u)=1-(abs(rbar))^2-ns/ni*(abs(tbar)^2);

end

plot(lambda, A)
```

6.2 Light reflection at the interface for IPCE calculation

For IPCE calculation, the same materials data and formulas to section 6.1 were used. Following are the MATLAB codes for the reflections(air/substrate, air/water and water/substrate) and light intensity at substrate.

```
for u=1:800
x=399+u; %wavelength lambda

%Water
p1=1.951e-018;
p2=-9.029e-015;
p3=1.737e-011;
p4=-1.785e-008;
p5=1.04e-005;
p6=-0.003297;
p7=1.821;
ni=p1*x^6+p2*x^5+p3*x^4+p4*x^3+p5*x^2+p6*x+p7;

%Iron oxide
p11=1.432e-013;
p12=-4.671e-010;
p13=5.671e-007;
p14=-0.0003067;
p15=0.06605;
p16=-0.07245;
n=p11*x^5+p12*x^4+p13*x^3+p14*x^2+p15*x+p16;
```

```
p21=0.4974;
p22=394;
p23=142;
p24=6.735e+011;
p25=-2.841e+004;
p26=5299;
k=p21*exp(-((x-p22)/p23)^2) + p24*exp(-((x-p25)/p26)^2);

%Silicon
p31=198;
p32=-0.012;
p33=3.96;
p34=-8.192e-005;
ns=p31*exp(p32*x)+p33*exp(p34*x);

%Air
nAir=1;

%definitions
d=20; %film thickness(nm)
q0=2*3.1416/x;
del=q0*d;
m=n+k*i;
ri=(ni-m)/(ni+m); %water incidence
rAir=(nAir-m)/(nAir+m); %air incidence
lambda(u)=x;
gamma=exp(i*m*del);

%air/water
Rairwater(u)=((ni-nAir)/(ni+nAir))^2;

%water/iron oxide/silicon
rs=(ns-m)/(ns+m);
rbar=(ri-rs*(abs(gamma))^2)/(1-ri*rs*(abs(gamma))^2);
tbar=(1+ri)*(1-rs)*gamma*exp(-i*ns*del)/(1-ri*rs*(abs(gamma)^2));
Awatersub(u)=1-(abs(rbar))^2-ns/ni*(abs(tbar)^2);
Rwatersub(u)=(abs(rbar))^2;

%air/iron oxide/silicon
rs=(ns-m)/(ns+m);
rbar=(rAir-rs*(abs(gamma))^2)/(1-rAir*rs*(abs(gamma))^2);
tbar=(1+rAir)*(1-rs)*gamma*exp(-i*ns*del)/(1-rAir*rs*(abs(gamma)^2));
Aairsub(u)=1-(abs(rbar))^2-ns/ni*(abs(tbar)^2);
Rairsub(u)=(abs(rbar))^2;

%final incident light intensity to substrate
Isub(u)=(1-Rairwater(u))*(1-Rwatersub(u));
```

```
end

plot(lambda, Rairsub)
ylabel('Reflectance, Air/Sub')
figure
plot(lambda, Rwatersub)
ylabel('Reflectance, Water/Sub')
figure
plot(lambda, Rairwater)
ylabel('Reflectance, Air/Water')
figure
plot(lambda, Isub)
ylabel('Intensity(max=1) at substrate')
```

Bibliography

1.   Annual Energy Outlook, U.S. Energy Information Administration. 2011.

2.   Winter, M.; Brodd, R. J., What Are Batteries, Fuel Cells, and Supercapacitors? *Chemical Reviews* **2004,** *104* (10), 4245-4270.

3.   Steinfeld, A.; Weimer, A. W., Thermochemical Production of Fuels with Concentrated Solar Energy. *Optics Express* **2010,** *18* (9), A100-A111.

4.   Yang, J. Y.; Bullock, R. M.; DuBois, M. R.; DuBois, D. L., Fast and efficient molecular electrocatalysts for H2 production: Using hydrogenase enzymes as guides. *MRS Bulletin* **2011,** *36* (01), 39-47.

5.   Yacoby, I.; Pochekailov, S.; Toporik, H.; Ghirardi, M. L.; King, P. W.; Zhang, S., Photosynthetic electron partitioning between [FeFe]-hydrogenase and ferredoxin:NADP+-oxidoreductase (FNR) enzymes in vitro. *Proceedings of the National Academy of Sciences* **2011**.

6.   Blankenship, R. E.; Tiede, D. M.; Barber, J.; Brudvig, G. W.; Fleming, G.; Ghirardi, M.; Gunner, M. R.; Junge, W.; Kramer, D. M.; Melis, A.; Moore, T. A.; Moser, C. C.; Nocera, D. G.; Nozik, A. J.; Ort, D. R.; Parson, W. W.; Prince, R. C.; Sayre, R. T., Comparing Photosynthetic and Photovoltaic Efficiencies and Recognizing the Potential for Improvement. *Science* **2011,** *332* (6031), 805-809.

7.   Steinfeld, A., Solar thermochemical production of hydrogen--a review. *Solar Energy* **2005,** *78* (5), 603-615.

8.   Tour, J. M.; Kittrell, C.; Colvin, V. L., Green carbon as a bridge to renewable energy. *Nature Materials* **2010,** *9* (11), 871-874.

9.   McDowall, W.; Eames, M., Towards a sustainable hydrogen economy: A multi-criteria sustainability appraisal of competing hydrogen futures. *International Journal of Hydrogen Energy* **2007,** *32* (18), 4611-4626.

10.   Roy, S. C.; Varghese, O. K.; Paulose, M.; Grimes, C. A., Toward Solar Fuels: Photocatalytic Conversion of Carbon Dioxide to Hydrocarbons. *Acs Nano* **2010,** *4* (3), 1259-1278.

11.   Jager, B.; Dry, M. E.; Shingles, T.; Steynberg, A. P., Experience with a new type of reactor for Fischer-Tropsch synthesis. *Catalysis Letters* **1990,** *7* (1), 293-301.

12.   van Dyk, J. C.; Keyser, M. J.; Coertzen, M., Syngas production from South African coal sources using Sasol-Lurgi gasifiers. *International Journal of Coal Geology* **2006,** *65* (3-4), 243-253.

13.   Steynberg, A. P.; Nel, H. G., Clean coal conversion options using Fischer-Tropsch technology. *Fuel* **2004,** *83* (6), 765-770.

14.   Olah, G. A.; Goeppert, A.; Prakash, G. K. S., Chemical Recycling off Carbon Dioxide to Methanol and Dimethyl Ether: From Greenhouse Gas to Renewable, Environmentally Carbon Neutral Fuels and Synthetic Hydrocarbons. *Journal of Organic Chemistry* **2009,** *74* (2), 487-498.

15.   Morrison, S. R., *Electrochemistry at semiconductor and oxidized metal electrodes*. Plenum press: New York, 1980.

16.   Finklea, H. O., *Semiconductor electrodes*. Elsevier: New York, 1988.

17.   Bard, A. J.; Faulkner, L. R., *Electrochemical methods : fundamentals and applications*. 2 ed.; John Wiley & Sons: New York, 2001.

18.   Sze, S. M., *Physics of semiconductor devices*. 2 ed.; John Wiley and Sons: New York, 1981.

19.   Gelderman, K.; Lee, L.; Donne, S. W., Flat-Band Potential of a Semiconductor: Using the Mott–Schottky Equation. *Journal of Chemical Education* **2007,** *84* (4), 685-null.

20.   Bard, A. J.; Parsons, R.; Jordan, J., *Standard potentials in aqueous solution*. Marcel Dekker: New York, 1985.

21.   van de Krol, R.; Liang, Y. Q.; Schoonman, J., Solar hydrogen production with nanostructured metal oxides. *Journal of Materials Chemistry* **2008,** *18* (20), 2311-2320.

22.   Roy, A.; Watson, S.; Infield, D., Comparison of electrical energy efficiency of atmospheric and high-pressure electrolysers. *International Journal of Hydrogen Energy* **2006,** *31* (14), 1964-1979.

23.   Brimblecombe, R.; Dismukes, G. C.; Swiegers, G. F.; Spiccia, L., Molecular water-oxidation catalysts for photoelectrochemical cells. *Dalton Transactions* **2009,** (43), 9374-9384.

24.   Kanan, M. W.; Nocera, D. G., In situ formation of an oxygen-evolving catalyst in neutral water containing phosphate and Co2+. *Science* **2008,** *321* (5892), 1072-1075.

25.   Steinmiller, E. M. P.; Choi, K. S., Photochemical deposition of cobalt-based oxygen evolving catalyst on a semiconductor photoanode for solar oxygen production. *Proceedings of the National Academy of Sciences of the United States of America* **2009,** *106* (49), 20633-20636.

26.   Dinca, M.; Surendranath, Y.; Nocera, D. G., Nickel-borate oxygen-evolving catalyst that functions under benign conditions. *Proceedings of the National Academy of Sciences of the United States of America* **2010,** *107* (23), 10337-10341.

27.   Talbot, D.; Talbot, J., *Corrosion science and technology*. CRC Press: 1998.

28.   Yerga, R. M. N.; Galvan, M. C. A.; del Valle, F.; de la Mano, J. A. V.; Fierro, J. L. G., Water Splitting on Semiconductor Catalysts under Visible-Light Irradiation. *Chemsuschem* **2009,** *2* (6), 471-485.

29.   Fujishima, A.; Honda, K., ELECTROCHEMICAL PHOTOLYSIS OF WATER AT A SEMICONDUCTOR ELECTRODE. *Nature* **1972,** *238* (5358), 37-+.

30.   Li, Y.; Zhang, J. Z., Hydrogen generation from photoelectrochemical water splitting based on nanomaterials. *Laser & Photonics Reviews* **2010,** *4* (4), 517-528.

31.   Gratzel, M., Photoelectrochemical cells. *Nature* **2001,** *414* (6861), 338-344.

32.   Lee, J. S., Photocatalytic water splitting under visible light with particulate semiconductor catalysts. *Catalysis Surveys from Asia* **2005,** *9* (4), 217-227.

33.   Sivula, K.; Le Formal, F.; Grätzel, M., Solar Water Splitting: Progress Using Hematite (α-Fe2O3) Photoelectrodes. *ChemSusChem* **2011,** *4* (4), 432-449.

34.   Borgarello, E.; Kiwi, J.; Gratzel, M.; Pelizzetti, E.; Visca, M., VISIBLE-LIGHT INDUCED WATER CLEAVAGE IN COLLOIDAL SOLUTIONS OF CHROMIUM-DOPED TITANIUM-DIOXIDE PARTICLES. *Journal of the American Chemical Society* **1982,** *104* (11), 2996-3002.

35.   Yamashita, H.; Harada, M.; Misaka, J.; Takeuchi, M.; Ikeue, K.; Anpo, M., Degradation of propanol diluted in water under visible light irradiation using metal ion-implanted titanium dioxide photocatalysts. *Journal of Photochemistry and Photobiology a-Chemistry* **2002,** *148* (1-3), 257-261.

36.   Kato, H.; Kudo, A., Visible-light-response and photocatalytic activities of TiO2 and SrTiO3 photocatalysts codoped with antimony and chromium. *Journal of Physical Chemistry B* **2002,** *106* (19), 5029-5034.

37.   Sakthivel, S.; Kisch, H., Daylight photocatalysis by carbon-modified titanium dioxide. *Angewandte Chemie-International Edition* **2003,** *42* (40), 4908-4911.

38.   Chen, X. B.; Lou, Y. B.; Samia, A. C. S.; Burda, C.; Gole, J. L., Formation of oxynitride as the photocatalytic enhancing site in nitrogen-doped titania nanocatalysts: Comparison to a commercial nanopowder. *Advanced Functional Materials* **2005,** *15* (1), 41-49.

39.   Goossens, A.; Maloney, E. L.; Schoonman, J., Gas-phase synthesis of nanostructured anatase TiO2. *Chemical Vapor Deposition* **1998,** *4* (3), 109-114.

40.   Park, J. H.; Kim, S.; Bard, A. J., Novel carbon-doped TiO2 nanotube arrays with high aspect ratios for efficient solar water splitting. *Nano Letters* **2006,** *6* (1), 24-28.

41.   Hwang, Y. J.; Boukai, A.; Yang, P. D., High Density n-Si/n-TiO2 Core/Shell Nanowire Arrays with Enhanced Photoactivity. *Nano Letters* **2009,** *9* (1), 410-415.

42.   Santato, C.; Ulmann, M.; Augustynski, J., Photoelectrochemical properties of nanostructured tungsten trioxide films. *Journal of Physical Chemistry B* **2001,** *105* (5), 936-940.

43.   Santato, C.; Ulmann, M.; Augustynski, J., Enhanced visible light conversion efficiency using nanocrystalline WO3 films. *Advanced Materials* **2001,** *13* (7), 511-+.

44.   Miller, E. L.; Paluselli, D.; Marsen, B.; Rocheleau, R. E., Development of reactively sputtered metal oxide films for hydrogen-producing hybrid multijunction photoelectrodes. *Solar Energy Materials and Solar Cells* **2005,** *88* (2), 131-144.

45.   Liao, P. L.; Toroker, M. C.; Carter, E. A., Electron Transport in Pure and Doped Hematite. *Nano Letters* **2011,** *11* (4), 1775-1781.

46.   Ingler, W. B.; Baltrus, J. P.; Khan, S. U. M., Photoresponse of p-type zinc-doped iron(III) oxide thin films. *Journal of the American Chemical Society* **2004,** *126* (33), 10238-10239.

47.   Glasscock, J. A.; Barnes, P. R. F.; Plumb, I. C.; Savvides, N., Enhancement of photoelectrochemical hydrogen production from hematite thin films by the introduction of Ti and Si. *Journal of Physical Chemistry C* **2007,** *111* (44), 16477-16488.

48.   Sartoretti, C. J.; Alexander, B. D.; Solarska, R.; Rutkowska, W. A.; Augustynski, J.; Cerny, R., Photoelectrochemical oxidation of water at transparent ferric oxide film electrodes. *Journal of Physical Chemistry B* **2005,** *109* (28), 13685-13692.

49.   Kleiman-Shwarsctein, A.; Huda, M. N.; Walsh, A.; Yan, Y. F.; Stucky, G. D.; Hu, Y. S.; Al-Jassim, M. M.; McFarland, E. W., Electrodeposited Aluminum-Doped alpha-Fe2O3 Photoelectrodes: Experiment and Theory. *Chemistry of Materials* **2010,** *22* (2), 510-517.

50.   Cesar, I.; Kay, A.; Martinez, J. A. G.; Gratzel, M., Translucent thin film Fe2O3 photoanodes for efficient water splitting by sunlight: Nanostructure-directing effect of Si-doping. *Journal of the American Chemical Society* **2006,** *128* (14), 4582-4583.

51.   Kay, A.; Cesar, I.; Gratzel, M., New benchmark for water photooxidation by nanostructured alpha-Fe2O3 films. *Journal of the American Chemical Society* **2006,** *128* (49), 15714-15721.

52.   Liang, Y. Q.; van de Krol, R., Influence of Si dopant and SnO2 interfacial layer on the structure of the spray-deposited Fe2O3 films. *Chemical Physics Letters* **2009,** *479* (1-3), 86-90.

53.   Lin, Y.; Zhou, S.; Sheehan, S. W.; Wang, D., Nanonet-Based Hematite Heteronanostructures for Efficient Solar Water Splitting. *Journal of the American Chemical Society* **2011,** *133* (8), 2398-2401.

54.   Vayssieres, L.; Sathe, C.; Butorin, S. M.; Shuh, D. K.; Nordgren, J.; Guo, J. H., One-dimensional quantum-confinement effect in alpha-Fe2O3 ultrafine nanorod arrays. *Advanced Materials* **2005,** *17* (19), 2320-+.

55.   Mao, A.; Han, G. Y.; Park, J. H., Synthesis and photoelectrochemical cell properties of vertically grown alpha-Fe2O3 nanorod arrays on a gold nanorod substrate. *Journal of Materials Chemistry* **2010,** *20* (11), 2247-2250.

56.   Hu, Y. S.; Kleiman-Shwarsctein, A.; Stucky, G. D.; McFarland, E. W., Improved photoelectrochemical performance of Ti-doped alpha-Fe2O3 thin films by surface modification with fluoride. *Chemical Communications* **2009,** (19), 2652-2654.

57.   Tilley, S. D.; Cornuz, M.; Sivula, K.; Gratzel, M., Light-Induced Water Splitting with Hematite: Improved Nanostructure and Iridium Oxide Catalysis. *Angewandte Chemie-International Edition* **2010,** *49* (36), 6405-6408.

58.   Zhong, D. K.; Sun, J. W.; Inumaru, H.; Gamelin, D. R., Solar Water Oxidation by Composite Catalyst/alpha-Fe2O3 Photoanodes. *Journal of the American Chemical Society* **2009,** *131* (17), 6086-+.

59.   Boettcher, S. W.; Warren, E. L.; Putnam, M. C.; Santori, E. A.; Turner-Evans, D.; Kelzenberg, M. D.; Walter, M. G.; McKone, J. R.; Brunschwig, B. S.; Atwater, H. A.; Lewis, N. S., Photoelectrochemical Hydrogen Evolution Using Si Microwire Arrays. *Journal of the American Chemical Society* **2011,** *133* (5), 1216-1219.

60.   Paracchino, A.; Laporte, V.; Sivula, K.; Grätzel, M.; Thimsen, E., Highly active oxide photocathode for photoelectrochemical water reduction. *Nat Mater* **2011,** *10* (6), 456-461.

61.   Miller, E. L.; Rocheleau, R. E.; Deng, X. M., Design considerations for a hybrid amorphous silicon/photoelectrochemical multijunction cell for hydrogen production. *International Journal of Hydrogen Energy* **2003,** *28* (6), 615-623.

62.   Rocheleau, R. E.; Miller, E. L.; Misra, A., High-efficiency photoelectrochemical hydrogen production using multijunction amorphous silicon photoelectrodes. *Energy & Fuels* **1998,** *12* (1), 3-10.

63.   Khaselev, O.; Turner, J. A., A monolithic photovoltaic-photoelectrochemical device for hydrogen production via water splitting. *Science* **1998,** *280* (5362), 425-427.

64.   Khaselev, O.; Bansal, A.; Turner, J. A., High-efficiency integrated multijunction photovoltaic/electrolysis systems for hydrogen production. *International Journal of Hydrogen Energy* **2001,** *26* (2), 127-132.

65.   Licht, S.; Wang, B.; Mukerji, S.; Soga, T.; Umeno, M.; Tributsch, H., Efficient Solar Water Splitting, Exemplified by RuO2-Catalyzed AlGaAs/Si Photoelectrolysis. *The Journal of Physical Chemistry B* **2000,** *104* (38), 8920-8924.

66.   Young, E. R.; Costi, R.; Paydavosi, S.; Nocera, D. G.; Bulovic, V., Photo-assisted water oxidation with cobalt-based catalyst formed from thin-film cobalt metal on silicon photoanodes. *Energy & Environmental Science* **2011,** *4* (6), 2058-2061.

67.   Pijpers, J. J. H.; Winkler, M. T.; Surendranath, Y.; Buonassisi, T.; Nocera, D. G., Light-induced water oxidation at silicon electrodes functionalized with a cobalt oxygen-evolving catalyst. *Proceedings of the National Academy of Sciences* **2011**.

68.   Sears, W. M., HOLE INJECTION INTO SINGLE-CRYSTALLINE AND POLYCRYSTALLINE SILICON ELECTRODES. *Journal of Applied Physics* **1985,** *57* (6), 2051-2056.

69.   Madou, M. J.; Loo, B. H.; Frese, K. W.; Morrison, S. R., BULK AND SURFACE CHARACTERIZATION OF THE SILICON ELECTRODE. *Surface Science* **1981,** *108* (1), 135-152.

70.   Zhang, X. G., *Electrochemistry of silicon and its oxide*. Kluwer Academic/Plenum Publishers: New York, 2001.

71.   Beermann, N.; Vayssieres, L.; Lindquist, S. E.; Hagfeldt, A., Photoelectrochemical studies of oriented nanorod thin films of hematite. *Journal of the Electrochemical Society* **2000,** *147* (7), 2456-2461.

72.   Allen, P.; Hampson, N. A.; Bignold, G. J., EFFECT OF ELECTRICAL POTENTIAL ON DISSOLUTION OF IRON-OXIDE CRYSTALS .1. REVIEW OF SELECTED RELEVANT LITERATURE. *Surface Technology* **1978,** *7* (4), 273-287.

73.   Merrill, M. D.; Dougherty, R. C., Metal Oxide Catalysts for the Evolution of O2 from H2O. *The Journal of Physical Chemistry C* **2008,** *112* (10), 3655-3666.

74.   Osaka, T.; Kitayama, H.; Hirota, N.; Eskildsen, S. S., STRUCTURAL-ANALYSIS OF IRON-OXIDE COATED N-SILICON HETEROJUNCTION PHOTOANODES. *Electrochimica Acta* **1984,** *29* (10), 1365-1370.

75.   Osaka, T.; Ejiri, K.; Hirota, N., Photoelectrochemical Behavior of Iron Oxide/n-Si Heterojunction Electrodes with an Outer Pd Layer. *Journal of The Electrochemical Society* **1984,** *131* (7), 1571-1574.

76.   Morisaki, H.; Ono, H.; Dohkoshi, H.; Yazawa, K., IRON-OXIDE COATED N-SI AS A HETEROSTRUCTURE PHOTOANODE FOR THE PHOTOELECTROLYSIS OF WATER. *Japanese Journal of Applied Physics* **1980,** *19* (3), L148-L150.

77.   Nogami, G.; Yamaguchi, H.; Maeda, G.; Beppu, K.; Ueda, Y.; Nakamura, T., XPS AND AES STUDIES ON IRON-OXIDE-COATED SI PHOTO-ANODES WITH A NEGATIVE FLAT-BAND POTENTIAL. *Journal of Applied Physics* **1983,** *54* (3), 1605-1609.

78.   Sastri, M. V. C.; Nagasubramanian, G., STUDIES ON FERRIC-OXIDE ELECTRODES FOR THE PHOTO-ASSISTED ELECTROLYSIS OF WATER. *International Journal of Hydrogen Energy* **1982,** *7* (11), 873-876.

79.   Archer, R. J.; Atalla, M. M., METALS CONTACTS ON CLEAVED SILICON SURFACES. *Annals of the New York Academy of Sciences* **1963,** *101* (3), 697-&.

80.   Popovic, R. S., METAL-N-TYPE SEMICONDUCTOR OHMIC CONTACT WITH A SHALLOW N+ SURFACE-LAYER. *Solid-State Electronics* **1978,** *21* (9), 1133-1138.

81.   Boettcher, S. W.; Spurgeon, J. M.; Putnam, M. C.; Warren, E. L.; Turner-Evans, D. B.; Kelzenberg, M. D.; Maiolo, J. R.; Atwater, H. A.; Lewis, N. S., Energy-Conversion Properties of Vapor-Liquid-Solid-Grown Silicon Wire-Array Photocathodes. *Science* **2010,** *327* (5962), 185-187.

82.   Kelzenberg, M. D.; Boettcher, S. W.; Petykiewicz, J. A.; Turner-Evans, D. B.; Putnam, M. C.; Warren, E. L.; Spurgeon, J. M.; Briggs, R. M.; Lewis, N. S.; Atwater, H. A., Enhanced absorption and carrier collection in Si wire arrays for photovoltaic applications. *Nature Materials* **2010,** *9* (3), 239-244.

83.   Kayes, B. M.; Atwater, H. A.; Lewis, N. S., Comparison of the device physics principles of planar and radial p-n junction nanorod solar cells. *Journal of Applied Physics* **2005,** *97* (11), 11.

84.   Maiolo, J. R.; Kayes, B. M.; Filler, M. A.; Putnam, M. C.; Kelzenberg, M. D.; Atwater, H. A.; Lewis, N. S., High aspect ratio silicon wire array photoelectrochemical cells. *Journal of the American Chemical Society* **2007,** *129* (41), 12346-+.

85.   Chai, C. C.; Peng, J.; Yan, B. P., PREPARATION AND GAS-SENSING PROPERTIES OF ALPHA-FE2O3 THIN-FILMS. *Journal of Electronic Materials* **1995,** *24* (7), 799-804.

86.   Li, X.; Bohn, P. W., Metal-assisted chemical etching in HF/H2O2 produces porous silicon. *Applied Physics Letters* **2000,** *77* (16), 2572-2574.

87.   Huang, Z. P.; Fang, H.; Zhu, J., Fabrication of silicon nanowire arrays with controlled diameter, length, and density. *Advanced Materials* **2007,** *19* (5), 744-+.

88.   Choi, W. K.; Liew, T. H.; Dawood, M. K., Synthesis of Silicon Nanowires and Nanofin Arrays Using Interference Lithography and Catalytic Etching. *Nano Letters* **2008,** *8* (11), 3799-3802.

89.   Chang, S. W.; Chuang, V. P.; Boles, S. T.; Ross, C. A.; Thompson, C. V., Densely Packed Arrays of Ultra-High-Aspect-Ratio Silicon Nanowires Fabricated using Block-Copolymer Lithography and Metal-Assisted Etching. *Advanced Functional Materials* **2009,** *19* (15), 2495-2500.

90.   Qu, Y. Q.; Liao, L.; Li, Y. J.; Zhang, H.; Huang, Y.; Duan, X. F., Electrically Conductive and Optically Active Porous Silicon Nanowires. *Nano Letters* **2009,** *9* (12), 4539-4543.

91.   Kayes, B. M.; Filler, M. A.; Putnam, M. C.; Kelzenberg, M. D.; Lewis, N. S.; Atwater, H. A., Growth of vertically aligned Si wire arrays over large areas (> 1 cm(2)) with Au and Cu catalysts. *Applied Physics Letters* **2007,** *91* (10), 3.

92.   Ganapati, V.; Fenning, D. P.; Bertoni, M. I.; Kendrick, C. E.; Fecych, A. E.; Redwing, J. M.; Buonassisi, T., Seeding of Silicon Wire Growth by Out-Diffused Metal Precipitates. *Small* **2011,** *7* (5), 563-567.

93.   Lieber, C. M.; Wang, Z. L., Functional nanowires. *Mrs Bulletin* **2007,** *32* (2), 99-108.

94.   Li, Y.; Qian, F.; Xiang, J.; Lieber, C. M., Nanowire electronic and optoelectronic devices. *Materials Today* **2006,** *9* (10), 18-27.

95.   Jun, K.; Joo, J.; Jacobson, J. M., Focused ion beam-assisted bending of silicon nanowires for complex three dimensional structures. *Journal of Vacuum Science & Technology B* **2009,** *27* (6), 3043-3047.

96.   Jun, K.; Jacobson, J. M., Programmable growth of branched silicon nanowires using a focused ion beam. *Nano Lett* **2010,** *10* (8), 2777-82.

97.   Kolasinski, K. W., Catalytic growth of nanowires: Vapor-liquid-solid, vapor-solid-solid, solution-liquid-solid and solid-liquid-solid growth. *Current Opinion in Solid State and Materials Science 10* (3-4), 182-191.

98.   Lu, W.; Lieber, C. M., Semiconductor nanowires. *Journal of Physics D-Applied Physics* **2006,** *39* (21), R387-R406.

99.   Bakkers, E.; Borgstrom, M. T.; Verheijen, M. A., Epitaxial growth of III-V nanowires on group IV substrates. *Mrs Bulletin* **2007,** *32* (2), 117-122.

100.   Martensson, T.; Svensson, C. P. T.; Wacaser, B. A.; Larsson, M. W.; Seifert, W.; Deppert, K.; Gustafsson, A.; Wallenberg, L. R.; Samuelson, L., Epitaxial III-V nanowires on silicon. *Nano Letters* **2004,** *4* (10), 1987-1990.

101.   Hochbaum, A. I.; Fan, R.; He, R. R.; Yang, P. D., Controlled growth of Si nanowire arrays for device integration. *Nano Letters* **2005,** *5* (3), 457-460.

102.   Wang, D. L.; Lieber, C. M., Inorganic materials - Nanocrystals branch out. *Nature Materials* **2003,** *2* (6), 355-356.

103.   Bifano, T. G.; Johnson, H. T.; Bierden, P.; Mali, R. K., Elimination of stress-induced curvature in thin-film structures. *Journal of Microelectromechanical Systems* **2002,** *11* (5), 592-597.

104.   Prewett, P. D.; Anthony, C. J.; Cheneler, D.; Ward, M. C. L., Stress-induced curvature of focused ion beam fabricated microcantilevers. *Micro & Nano Letters* **2008,** *3* (1), 25-28.

105.   Park, B. C.; Jung, K. Y.; Song, W. Y.; Beom-Hoan, O.; Ahn, S. J., Bending of a carbon nanotube in vacuum using a focused ion beam. *Advanced Materials* **2006,** *18* (1), 95-98.

106.   Tripathi, S. K.; Shukla, N.; Dhamodaran, S.; Kulkarni, V. N., Controlled manipulation of carbon nanopillars and cantilevers by focused ion beam. *Nanotechnology* **2008,** *19* (20).

107.   Wagner, R. S.; Doherty, C. J., MECHANISM OF BRANCHING AND KINKING DURING VLS CRYSTAL GROWTH. *Journal of the Electrochemical Society* **1968,** *115* (1), 93-&.

108.   Dick, K. A.; Deppert, K.; Larsson, M. W.; Martensson, T.; Seifert, W.; Wallenberg, L. R.; Samuelson, L., Synthesis of branched 'nanotrees' by controlled seeding of multiple branching events. *Nature Materials* **2004,** *3* (6), 380-384.

109.   Wang, D.; Qian, F.; Yang, C.; Zhong, Z. H.; Lieber, C. M., Rational growth of branched and hyperbranched nanowire structures. *Nano Letters* **2004,** *4* (5), 871-874.

110.   Doerk, G. S.; Ferralis, N.; Carraro, C.; Maboudian, R., Growth of branching Si nanowires seeded by Au-Si surface migration. *Journal of Materials Chemistry* **2008,** *18* (44), 5376-5381.

111.   Dick, K. A.; Deppert, K.; Karlsson, L. S.; Larsson, M. W.; Seifert, W.; Wallenberg, L. R.; Samuelson, L., Directed growth of branched nanowire structures. *Mrs Bulletin* **2007,** *32* (2), 127-133.

112.   Dick, K. A.; Deppert, K.; Karlsson, L. S.; Seifert, W.; Wallenberg, L. R.; Samuelson, L., Position-controlled interconnected InAs nanowire networks. *Nano Letters* **2006,** *6* (12), 2842-2847.

113.   Shedd, G. M.; Lezec, H.; Dubner, A. D.; Melngailis, J., FOCUSED ION-BEAM INDUCED DEPOSITION OF GOLD. *Applied Physics Letters* **1986,** *49* (23), 1584-1586.

114.   Guckel, H.; Burns, D. W.; Visser, C. C. G.; Tilmans, H. A. C.; Deroo, D., FINE-GRAINED POLYSILICON FILMS WITH BUILT-IN TENSILE STRAIN. *Ieee Transactions on Electron Devices* **1988,** *35* (6), 800-801.

115.   Prewett, P. D.; Heard, P. J., REPAIR OF OPAQUE DEFECTS IN PHOTOMASKS USING FOCUSED ION-BEAMS. *Journal of Physics D-Applied Physics* **1987,** *20* (9), 1207-1209.

116.   Buaud, P. P.; Dheurle, F. M.; Irene, E. A.; Patnaik, B. K.; Parikh, N. R., INSITU STRAIN-MEASUREMENTS DURING THE FORMATION OF PLATINUM SILICIDE FILMS. *Journal of Vacuum Science & Technology B* **1991,** *9* (5), 2536-2541.

117.   Magagnin, L.; Maboudian, R.; Carraro, C., Gold deposition by galvanic displacement on semiconductor surfaces: Effect of substrate on adhesion. *Journal of Physical Chemistry B* **2002,** *106* (2), 401-407.

118.   Gao, D.; He, R. R.; Carraro, C.; Howe, R. T.; Yang, P. D.; Maboudian, R., Selective growth of Si nanowire arrays via galvanic displacement processes in water-in-oil microemulsions. *Journal of the American Chemical Society* **2005,** *127* (13), 4574-4575.

119.   San Paulo, A.; Arellano, N.; Plaza, J. A.; He, R. R.; Carraro, C.; Maboudian, R.; Howe, R. T.; Bokor, J.; Yang, P. D., Suspended mechanical structures based on elastic silicon nanowire arrays. *Nano Letters* **2007,** *7* (4), 1100-1104.

120.   Porter, L. A.; Choi, H. C.; Schmeltzer, J. M.; Ribbe, A. E.; Elliott, L. C. C.; Buriak, J. M., Electroless nanoparticle film deposition compatible with photolithography, microcontact printing, and dip-pen nanolithography patterning technologies. *Nano Letters* **2002,** *2* (12), 1369-1372.

121.   Fan, R.; Wu, Y. Y.; Li, D. Y.; Yue, M.; Majumdar, A.; Yang, P. D., Fabrication of silica nanotube arrays from vertical silicon nanowire templates. *Journal of the American Chemical Society* **2003,** *125* (18), 5254-5255.

122. Shir, D.; Liu, B. Z.; Mohammad, A. M.; Lew, K. K.; Mohney, S. E., Oxidation of silicon nanowires. *Journal of Vacuum Science & Technology B* **2006**, *24* (3), 1333-1336.

123. Li, J.; Stein, D.; McMullan, C.; Branton, D.; Aziz, M. J.; Golovchenko, J. A., Ion-beam sculpting at nanometre length scales. *Nature* **2001**, *412* (6843), 166-169.

124. Kim, K. J.; Moon, D. W.; Lee, S. K.; Jung, K. H., Formation of a highly oriented FeO thin film by phase transition of Fe3O4 and Fe nanocrystallines. *Thin Solid Films* **2000**, *360* (1-2), 118-121.

125. Ye, X. S.; Lin, D. S.; Jiao, Z. K.; Zhang, L. D., The thermal stability of nanocrystalline maghemite Fe2O3. *Journal of Physics D-Applied Physics* **1998**, *31* (20), 2739-2744.

126. Akl, A. A., Optical properties of crystalline and non-crystalline iron oxide thin films deposited by spray pyrolysis. *Applied Surface Science* **2004**, *233* (1-4), 307-319.

127. Hou, Y. L.; Xu, Z. C.; Sun, S. H., Controlled synthesis and chemical conversions of FeO nanoparticles. *Angewandte Chemie-International Edition* **2007**, *46* (33), 6329-6332.

128. Cesar, I.; Sivula, K.; Kay, A.; Zboril, R.; Graetzel, M., Influence of Feature Size, Film Thickness, and Silicon Doping on the Performance of Nanostructured Hematite Photoanodes for Solar Water Splitting. *Journal of Physical Chemistry C* **2009**, *113* (2), 772-782.

129. Thimsen, E.; Le Formal, F.; Gratzel, M.; Warren, S. C., Influence of Plasmonic Au Nanoparticles on the Photoactivity of Fe2O3 Electrodes for Water Splitting. *Nano Letters* **2011**, *11* (1), 35-43.

130. Tepper, T.; Ross, C. A., Pulsed laser deposition of iron oxide films. *Journal of Applied Physics* **2002**, *91* (7), 4453-4456.

131. Sivula, K.; Zboril, R.; Le Formal, F.; Robert, R.; Weidenkaff, A.; Tucek, J.; Frydrych, J.; Gratzel, M., Photoelectrochemical Water Splitting with Mesoporous Hematite Prepared by a Solution-Based Colloidal Approach. *Journal of the American Chemical Society* **2010**, *132* (21), 7436-7444.

132. Tassis, D. H.; Dimitriadis, C. A.; Boultadakis, S.; Arvanitidis, J.; Ves, S.; Kokkou, S.; Logothetidis, S.; Valassiades, O.; Poulopoulos, P.; Flevaris, N. K., Influence of conventional furnace and rapid thermal annealing on the quality of polycrystalline beta-FeSi2 thin films grown from vapor-deposited Fe/Si multilayers. *Thin Solid Films* **1997**, *310* (1-2), 115-122.

133. Zarpellon, J.; Jurca, H. F.; Klein, J. J.; Schreiner, W. H.; Mattoso, N.; Mosca, D. H., Iron silicide formation from Fe thin-film electrodeposition on hydrogen-terminated Si(111). *Journal of the Electrochemical Society* **2005**, *152* (12), C808-C812.

134. Tsubomura, H.; Nakato, Y.; Hiramoto, M.; Yano, H., METAL-OXIDE COATED P-N-JUNCTION SILICON ELECTRODES FOR PHOTOELECTROCHEMICAL SOLAR-ENERGY CONVERSION. *Canadian Journal of Chemistry-Revue Canadienne De Chimie* **1985**, *63* (7), 1759-1762.

135. Pailhe, N.; Wattiaux, A.; Gaudon, M.; Demourgues, A., Impact of structural features on pigment properties of alpha-Fe2O3 haematite. *Journal of Solid State Chemistry* **2008**, *181* (10), 2697-2704.

136. Madou, M. J., *Fundamentals of Microfabrication: The Science of Miniaturization*. 2 ed.; CRC Press: Boca Raton, 2002.

137. Palik, E. D.; Bermudez, V. M.; Glembocki, O. J., ELLIPSOMETRIC STUDY OF THE ETCH-STOP MECHANISM IN HEAVILY DOPED SILICON. *Journal of the Electrochemical Society* **1985**, *132* (1), 135-141.

138. Hagglund, C.; Apell, S. P.; Kasemo, B., Maximized Optical Absorption in Ultrathin Films and Its Application to Plasmon-Based Two-Dimensional Photovoltaics. *Nano Letters* **2010**, *10* (8), 3135-3141.

139.   Le Formal, F.; Gratzel, M.; Sivula, K., Controlling Photoactivity in Ultrathin Hematite Films for Solar Water-Splitting. *Advanced Functional Materials* **2010,** *20* (7), 1099-1107.

140.   Khan, S. U. M.; Akikusa, J., Photoelectrochemical splitting of water at nanocrystalline n-Fe2O3 thin-film electrodes. *Journal of Physical Chemistry B* **1999,** *103* (34), 7184-7189.

141.   Miller, E. L.; Paluselli, D.; Marsen, B.; Rocheleau, R. E., Low-temperature reactively sputtered iron oxide for thin film devices. *Thin Solid Films* **2004,** *466* (1-2), 307-313.

142.   Glasscock, J. A.; Barnes, P. R. F.; Plumb, I. C.; Bendavid, A.; Martin, P. J., Structural, optical and electrical properties of undoped polycrystalline hematite thin films produced using filtered arc deposition. *Thin Solid Films* **2008,** *516* (8), 1716-1724.

143.   Shinde, S. S.; et al., Physical properties of hematite α-Fe 2 O 3 thin films: application to photoelectrochemical solar cells. *Journal of Semiconductors* **2011,** *32* (1), 013001.

144.   Kumari, S.; Tripathi, C.; Singh, A. P.; Chauhan, D.; Shrivastav, R.; Dass, S.; Satsangi, V. R., Characterization of Zn-doped hematite thin films for photoelectrochemical splitting of water. *Current Science* **2006,** *91* (8), 1062-1064.

145.   Brillet, J.; Gratzel, M.; Sivula, K., Decoupling Feature Size and Functionality in Solution-Processed, Porous Hematite Electrodes for Solar Water Splitting. *Nano Letters* **2010,** *10* (10), 4155-4160.

146.   Kumar, A.; Wilisch, W. C. A.; Lewis, N. S., THE ELECTRICAL-PROPERTIES OF SEMICONDUCTOR-METAL, SEMICONDUCTOR LIQUID, AND SEMICONDUCTOR CONDUCTING POLYMER CONTACTS. *Critical Reviews in Solid State and Materials Sciences* **1993,** *18* (4), 327-353.

147.   Dareedwards, M. P.; Goodenough, J. B.; Hamnett, A.; Trevellick, P. R., ELECTROCHEMISTRY AND PHOTOELECTROCHEMISTRY OF IRON(III) OXIDE. *Journal of the Chemical Society-Faraday Transactions I* **1983,** *79*, 2027-2041.

148.   Papaioannou, J. C.; Patermarakis, G. S.; Karayianni, H. S., Electron hopping mechanism in hematite (alpha-Fe2O3). *Journal of Physics and Chemistry of Solids* **2005,** *66* (5), 839-844.

149.   Lodi, G.; Sivieri, E.; Debattisti, A.; Trasatti, S., RUTHENIUM DIOXIDE-BASED FILM ELECTRODES .3. EFFECT OF CHEMICAL COMPOSITION AND SURFACE MORPHOLOGY ON OXYGEN EVOLUTION IN ACID-SOLUTIONS. *Journal of Applied Electrochemistry* **1978,** *8* (2), 135-143.

150.   Chen, Y. W.; Prange, J. D.; Dühnen, S.; Park, Y.; Gunji, M.; Chidsey, C. E. D.; McIntyre, P. C., Atomic layer-deposited tunnel oxide stabilizes silicon photoanodes for water oxidation. *Nat Mater* **2011,** *10* (7), 539-544.

151.   Sousapires, J. D.; Ali, P.; Crowder, B.; Dheurle, F.; Petersson, S.; Stolt, L.; Tove, P. A., MEASUREMENTS OF THE RECTIFYING BARRIER HEIGHTS OF THE VARIOUS IRIDIUM SILICIDES WITH N-SI. *Applied Physics Letters* **1979,** *35* (2), 202-204.

152.   Shockley, W.; Queisser, H. J., DETAILED BALANCE LIMIT OF EFFICIENCY OF P-N JUNCTION SOLAR CELLS. *Journal of Applied Physics* **1961,** *32* (3), 510-&.

153.   James, B. D.; Baum, G. N.; Perez, J.; Baum, K. N., Technoeconomic Analysis of Photoelectrochemical(PEC) Hydrogen Production, U.S. Department of Energy. 2009.

154.   Dai, H. B.; Ma, G. L.; Xia, H. J.; Wang, P., Combined Usage of Sodium Borohydride and Aluminum Powder for High-performance Hydrogen Generation. *Fuel Cells* **2011,** *11* (3), 424-430.

155.   Sharma, S. K.; Chakravarty, B. C.; Singh, S. N.; Das, B. K., GROWTH-KINETICS OF THIN ANODIC OXIDES OF SILICON AND ITS DEPENDENCE ON PHOSPHORUS CONCENTRATION IN SILICON. *Thin Solid Films* **1988,** *163*, 373-377.

156.   Philipsen, H. G. G.; Kelly, J. J., Anisotropy in the anodic oxidation of silicon in KOH solution. *Journal of Physical Chemistry B* **2005,** *109* (36), 17245-17253.

157.   Virtanen, S.; Schmuki, P.; Davenport, A. J.; Vitus, C. M., Dissolution of thin iron oxide films used as models for iron passive films studied by in situ x-ray absorption near-edge spectroscopy. *Journal of the Electrochemical Society* **1997,** *144* (1), 198-204.

158.   Takabayashi, S.; Nakamura, R.; Nakato, Y., A nano-modified Si/TiO2 composite electrode for efficient solar water splitting. *Journal of Photochemistry and Photobiology a-Chemistry* **2004,** *166* (1-3), 107-113.

159.   Miller, E. L.; Marsen, B.; Paluselli, D.; Rocheleau, R., Optimization of hybrid photoelectrodes for solar water-splitting. *Electrochemical and Solid State Letters* **2005,** *8* (5), A247-A249.

160.   Brillet, J.; Cornuz, M.; Le Formal, F.; Yum, J. H.; Gratzel, M.; Sivula, K., Examining architectures of photoanode-photovoltaic tandem cells for solar water splitting. *Journal of Materials Research* **2010,** *25* (1), 17-24.

161.   Ozer, N.; Tepehan, F., Optical and electrochemical characteristics of sol-gel deposited iron oxide films. *Solar Energy Materials and Solar Cells* **1999,** *56* (2), 141-152.

162.   Schiebener, P.; Straub, J.; Sengers, J.; Gallagher, J. S., REFRACTIVE-INDEX OF WATER AND STEAM AS FUNCTION OF WAVELENGTH, TEMPERATURE AND DENSITY. *Journal of Physical and Chemical Reference Data* **1990,** *19* (3), 677-717.